Ultrafast Charge Dynamics in Mesoporous Materials used in Dye-Sensitized Solar Cells

Priti Tiwana
Brasenose College

Condensed Matter Physics
Department of Physics
University of Oxford

Thesis submitted for the degree of
Doctor of Philosophy at the University of Oxford
Hilary 2013

Abstract

This thesis is concerned with measuring ultrafast electron dynamics taking place in dye-sensitized mesoporous semiconductor films employed as working electrodes in dye-sensitized solar cells (DSCs). An understanding of these ultrafast charge transfer mechanisms is essential for designing efficient photovoltaic (PV) devices with high photon-to-current conversion efficiency. Optical-pump terahertz-probe (OPTP) spectroscopy is a sub-picosecond resolution, non-contact, photoconductivity measurement technique which can be used to directly measure charge carrier dynamics within nanostructured materials without the need for invoking complex modelling schemes.

A combination of OPTP and photovoltaic measurements on mesoporous TiO_2 films show an early-time intra-particle electron mobility of $0.10\pm0.03\,\mathrm{cm}^2/(\mathrm{Vs})$. This value is an order of magnitude lower than that measured in bulk TiO_2 and can be partly explained by the restricted electron movement because of geometrical constraints and increased trap sites in the nanostructured material. In addition, the mesoporous film behaves like a nanostructured composite material, with the TiO_2 nanoparticles embedded in a low dielectric medium (air or vacuum), leading to lower apparent electron mobility. THz mobility measured in similar mesoporous ZnO and SnO_2 films sensitized with the same dye is calculated to be $0.17\pm0.04\,\mathrm{cm}^2/(\mathrm{Vs})$ for ZnO and $1.01\pm0.20\,\mathrm{cm}^2/(\mathrm{Vs})$ for SnO_2. Possible reasons for the deviation from mobilities reported in literature for the respective bulk materials have been discussed. The conclusion of this study is that while electron mobility values for nanoporous TiO_2 films are approaching theoretical maximum values, both intra- and inter-particle electron mobility in mesoporous ZnO and SnO_2 films offer considerable scope for improvement.

OPTP has also been used to measure electron injection rates in dye-sensitized TiO_2, ZnO and SnO_2 nanostructured films. They are seen to proceed in the order $TiO_2 > SnO_2 > ZnO$. While the process is complete within a few picoseconds in TiO_2/Z907, it is seen to extend beyond a nanosecond in case of ZnO. These measurements correlate well with injection efficiencies determined from DSCs fabricated from identical mesoporous films, suggesting that the slow injection components limit the overall solar cell photocurrent. The reasons for this observed difference in charge injection rates have been explored within.

It is now fairly common practice in the photovoltaic community to apply a coating of a wide band-gap material over the metal-oxide nanoparticles in DSCs to improve device performance. However, the underlying reasons for the improvement are not fully understood. With this motivation, OPTP spectroscopy has been used to study how the conformal coating affects early-time mechanisms, such as electron injection, trapping or diffusion length. The electron injection process is unaffected in case of $TiCl_4$-treated TiO_2 and MgO-treated ZnO, while it becomes much slower in case of MgO-treated SnO_2. Finally, a light-soaking effect observed in SnO_2-based solid-state DSCs has been examined in detail using THz spectroscopy and transient PV measurement techniques. It is concluded that continued exposure to light results in a rearrangement of charged species at the metal-oxide surface. This leads to an increase in the density of acceptor states or a lowering of the SnO_2 conduction band edge with respect to the dye excited state energy level, ultimately leading to faster electron transport and higher device photocurrents.

Dedicated to my parents.

Acknowledgements

I would like to sincerely thank

Prof. Laura Herz for giving me an opportunity to learn and work on state-of-the-art spectroscopic techniques in her beautiful lab, and for her constant support throughout my DPhil (both for technical or not-so-technical issues). Your guidance and friendship has taught me immensely over the past few years. Thank you.

Dr. Henry Snaith for introducing me to the world of photovoltaics research, and for all the great ideas and energy that he has shared with me over the past few years, and, of course, for helping fund my DPhil;

Prof. Franco Cacialli and **Prof. Robin Nicholas** for reviewing and examining my thesis very thoroughly and patiently;

Dr. Michael Johnston for technical guidance whenever I asked, and for giving me an opportunity to work as a tutor and lab-demonstrator under him. I enjoyed the experience immensely;

(Dr.) Patrick Parkinson for getting me started with terahertz spectroscopy and Matlab coding. And for cheerfully answering my endless questions about Brasenose, Oxford and England in general!

Pablo Docampo, Mike Lee, Mike Brown and Agnese Abrusci for not complaining too much about my questions when working in the device fabrication and characterization labs;

Stefan Guldin and Prof. Ulli Steiner for making my visit to their lab in Cambridge a very educational trip (& good fun, thanks to the EuroCup finals!);

Amy Stevens and Chaw-Keong for training me on the upconversion and TCSPC systems;

Labmates in the Herz and Johnston groups, both old and new: Amy, Chaw-Keong, Christian, Enrique, James, Patrick, Stephan, Suzie, Xinlong - for stimulating conversations, and, for letting me keep the office window open, come rain, hail or shine!

Labmates in the Snaith group (Agnese, Andy, Derek, Mike & Mike, Pablo) for all the laughs and beers together;

Technical and support staff in the Clarendon, for their enthusiastic and helpful solutions to my technical questions and all the chinwag sessions (esp. Rob Harris, Alan, George, Rob Storey, Dash, Janet, Paul Pattinson, Simon Moulder);

My parents and close friends, for their constant support, love and encouragement, and finally,

Nav and Josh, for waiting so patiently for the wife/mum to finish writing up. Thanks for taking care of dinners for so long, it's my turn now!

Contents

List of published papers:

- *Ultrafast terahertz conductivity dynamics in mesoporous TiO_2: Influence of dye sensitization and surface treatment in solid-state dye-sensitized solar cells*, **P Tiwana**, P Parkinson, MB Johnston, HJ Snaith, LM Herz, *J. Phys. Chem. C*, 114, 1365 (2010)
- *Control of solid-state dye-sensitized solar cell performance by block-copolymer-directed TiO_2 synthesis*, P Docampo, S Guldin, M Stefik, **P Tiwana**, MC Orilall, S Huttner, H Sai, U Wiesner, U Steiner, HJ Snaith, *Adv. Funct. Mater.*, 20, 1787 (2010)
- *Improved conductivity in dye-sensitised solar cells through block-copolymer confined TiO_2 crystallisation*, S Guldin, S Hüttner, **P Tiwana**, MC Orilall, B Ülgüt, M Stefik, P Docampo, M Kolle, G Divitini, C Ducati, SAT Redfern, HJ Snaith, U Wiesner, D Eder, U Steiner, *Energy Environ. Sci.*, 4, 225 (2011)
- *Electron Mobility and Injection Dynamics in Mesoporous ZnO, SnO_2, and TiO_2 Films Used in Dye-Sensitized Solar Cells*, **P Tiwana**, P Docampo, MB Johnston, HJ Snaith, LM Herz, *ACS Nano*, 5, 5158 (2011)
- *The origin of an efficiency improving "light soaking" effect in SnO_2 based solid-state dye-sensitized solar cells*, **P Tiwana**, P Docampo, MB Johnston, LM Herz, HJ Snaith, *Energy Environ. Sci.*, 5, 9566 (2012)
- *Unraveling the function of an MgO interlayer in both electrolyte and solid-state SnO_2 based dye-sensitized solar cells*, P Docampo, **P Tiwana**, N Sakai, H Miura, LM Herz, T Murakami, HJ Snaith, *J. Phys. Chem. C*, 116, 22840 (2012)

List of Abbreviations

Physical Constants

c	2.998×10^{8} m/s	speed of light
e	1.602×10^{-19} C	elementary charge
h	6.626×10^{-34} Js	Planck's constant
k_b	1.38×10^{-23} J/K	Boltzmann constant

Physical Variables

D_e	cm^2/s	Diffusion coefficient
E_0	V/m	Electric field amplitude
E_c	eV	Conduction band edge
E_F	eV	Fermi energy level
E_v	eV	Valence band edge
f	Hz	Frequency
F_{abs}	%	Absorbance
FF	%	Fill Factor
IPCE	%	Incident photon-to-current conversion efficiency
I_{SC}	mA	Short-circuit current
J	A/cm^2	Current density
J_{SC}	mA/cm^2	Short-circuit current density
k_{rec}	s^{-1}	Charge recombination rate
k_{signal}	s^{-1}	Exponential decay rate
k_{trans}	s^{-1}	Charge transport rate
L	μm	Sample thickness
l_e	nm	Electron diffusion length
M	M, mol/L, mol/m^3	Molar concentration
n		Refractive index
ñ		Complex refractive index
N_{incident}	$photons/cm^2/s$	Incident photon fluence
N_{abs}	$F_{\mathrm{abs}}N_{\mathrm{incident}}$, $photons/cm^2/s$	Incident photon fluence
$N(\tau)$	$photons/cm^2/s$	Number of (photoexcited) mobile charge carriers
OD		Optical density
R	Ω	Resistance
r_{41}	m/V	Electro-optic coefficient
T	K, °C	Temperature
$T(\tau)$, $\Delta T(\tau)$	V/m	Time-domain electric field amplitude measured by lock-ins
THz	10^{12} Hz	Terahertz

V_{OC}	mV	Open-circuit voltage
$\chi^{(2)}$		Second order susceptibility
$\Delta\sigma$	S/cm	Change in sample photoconductivity
η	%	Efficiency
η_{coll}	%	Charge collection efficiency
λ	nm	Wavelength
μ	$\mathrm{cm}^2/\mathrm{Vs}$	Carrier mobility
μ_{THz}	$\mathrm{cm}^2/\mathrm{Vs}$	Early-time carrier mobility calculated via THz pump probe spectroscopy
μ_{NE}	$\mathrm{cm}^2/\mathrm{Vs}$	Carrier mobility calculated in working DSC via Nernst-Einstein relation
μ_{bulk}	$\mathrm{cm}^2/\mathrm{Vs}$	Carrier mobility calculated in single crystals via Hall measurement
$\Omega/\square$	Ω	Sheet resistance
ω	$\omega = 2\pi f$, s^{-1}	Radial frequency
ϕ_{inj}		Charge injection efficiency (Quantum yield)
$\phi\mu$	$\mathrm{cm}^2/\mathrm{Vs}$	Effective mobility
$\sigma(\omega)$	S/cm	Conductivity spectrum
$\sigma(\tau)$	S/cm	Time-domain conductivity signal
τ	ps	Delay between pump and probe frequencies
τ'	ps	Delay between probe and gate frequencies
τ_e	ns	Electron lifetime

Abbreviations

Al_2O_3	Aluminium Oxide
AM1.5G	Air Mass 1.5 Global
APCE	Absorbed Photon-to-electron Conversion Efficiency
ASTM	American Society for Testing and Materials
BBO	β-Barium Borate (β-BaB_2O_4)
BET	Brunauer, Emmett and Teller method
BIPV	Building Integrated Photovoltaic
CB	Conduction Band
CdTe	Cadmium telluride photovoltaics
CIGS	Copper indium gallium selenide
CL	Compact Layer
CN	Cellulose Nitrate
CPA	Chirped Pulse Amplification
CV	Cyclic Voltammetry
DC	Direct Current
DI water	Deionised water
DoS, DOS	Density of States
DSC, DSSC	Dye-sensitized Solar Cell
EOS	Electro-Optic Sampling
EPFL	École Polytechnique Fédérale de Lausanne
FTDT	Finite-Difference Time-Domain method
FTO	Fluorine-doped tin-oxide
FWHM	Full Width Half Maximum

HOMO	Highest Occupied Molecular Orbital
HTM	Hole transporter molecule
IPA	Isopropyl Alcohol
IPCE	Incident Photon to Current Efficiency
JV	Current-voltage characteristics
LED	Light Emitting Diode
LHE	Light harvesting efficiency
LIN1, LIN2	Lock-ins 1,2
Li-TFSI	bis(trifluoromethyl-sulfonyl)amine lithium salt
LUMO	Lowest Unoccupied Molecular Orbital
MgO	Magnesium Oxide
MLCT	Metal-to-Ligand Charge Transfer
MPP	Maximum Power Point
NIR	Near InfraRed
NHE	Normal Hydrogen Electrode
NREL	National Renewable Energy Laboratory
OAP	Off-Axis Parabolic mirror
OPA	Optical Parametric Amplifier
OPD	Optical Penetration Depth
OPTP	Optical Pump Terahertz Probe Spectroscopy
PMT	PhotoMultiplier Tube
PV	Photovoltaic
QWP	Quarter Wave Plate
rpm	Revolutions Per Minute
SDSC	Solid-state Dye-Sensitized Solar Cell
Si	Silicon
SnO_2	Tin Dioxide
SNR	Signal-to-Noise Ratio
spiro-OMeTAD	2,2',7,7'-tetrakis(N,N-di-p-methoxypheny-amine)-9,9'-spirobifluorene
TAS	Transient Absorption Spectroscopy
*t*BP	4-tert-butylpyridine
TCO	Transparent Conductive Oxide
TDG	Timing Delay Generator
TDS	Time Domain Spectroscopy
TiO_2	Titanium Dioxide
TOF	Time Of Flight
TOPAS	Traveling-Wave Optical Parametric Amplifier of White-Light Continuum
TRMC	Time Resolved Microwave Conductivity
TRTS	Time Resolved Terahertz Spectroscopy
TW	Terawatt
UV	UltraViolet
VB	Valence Band
vs	versus
WTF	What the Fermi!
XRD	X-ray Diffraction
ZrO_2	Zirconium Dioxide
ZnO	Zinc Oxide
ZnTe	Zinc Telluride

Chapter 1

Introduction

At this point in human history, there is no doubt about the urgent need for replacing fossil fuel resources with alternative renewable energy resources in order to satisfy the ever-increasing worldwide energy demand. The latest BP statistical review reveals that most oil reserves, including those in the Middle East and Africa, are sufficient to meet only another 50 years of global production [1]. A recent increase in Venezuelan official reserve estimates increased Latin America's reserve limit to about 95 years. Global coal reserves will last for another 100 years, but world natural gas reserves are estimated to be sufficient for only $\sim$60 more years of global production. This highlights the need for a quick and reliable switch over to renewable energy resources. In addition, over the past few years, an irrefutable link has been shown between global warming and green-house gas emission such as CO_2, CH_4 and N_2O, due to burning of fossil fuels [2, 3]. While it is essential for humans to exercise control over our individual energy consumption "quota", there is no doubt that the overall energy requirement will keep growing exponentially. This further emphasises the urgent need for developing efficient and reliable methods for extracting usable energy from renewable energy sources.

The field of photovoltaics is of great interest among renewable energy resources because of the abundant availability of solar energy over most of the planet. To illustrate, in one hour more sunlight falls on the earth than what is used by the entire population in one year [4, 5]. Needless to say, some countries such as UK will have to rely on other renewable energy sources such as wind or tidal energy, in addition to solar energy, as suggested by

Prof. David MacKay [6]. As per the latest survey published by BP, solar power generating capacity grew by 73% in 2010, with a total installed capacity of 40 GW [1]. However, despite the rapid capacity growth, the share of solar power in total electricity generation remains low, at an estimated 0.1% [1]. Although attractive incentives have been offered by various governments for investing in renewable energy, the relatively easy availability of fossil fuels and the strong political and economic lobby for these resources makes it difficult for the alternatives to become anything more than 'alternatives'.

There is another important reason for solar cell technology not being as popular as it should be. To date, the field of photovoltaics is almost exclusively dominated by silicon solar cell technology, which offers efficient sunlight-to-electricity conversion, but suffers from steep production costs because of the need for high purity silicon. Hence there has been a lot of emphasis over the past couple of decades on developing high efficiency, long lasting, cheap solar cells. While respectable performances have been demonstrated in some of these technologies, they are still not competitive enough to displace the existing silicon solar cell market. Among these alternatives, a prime candidate is the concept of dye-sensitized solar cells (DSCs), introduced by O'Regan and Grätzel in 1991 [7]. These cells currently exhibit about 11% efficiency, are cheap to manufacture and can be semi-transparent, thus suitable for building-integrated photovoltaics (BIPV) [8–10].

1.1 Overview of this thesis

While device labs around the world have made tremendous improvements in enhancing DSC performance, many of the underlying electronic processes are still not fully understood, and a wide array of optical and electronic pump-probe techniques are being used to fill that gap. The work presented in this thesis is mainly focused on using sub-picosecond resolution optical-pump terahertz-probe (OPTP) spectroscopy for measuring electron dynamics in different mesoporous semiconductor films sensitized with dye molecules absorbing in the visible part of the spectrum. This gives an insight into the differences between various metal-oxides popularly used as photoanodes by the DSC community, and also an understanding of the effect of intrinsic and extrinsic material properties such as crystal-size, film porosity, nanoparticle alignment etc. on the overall device performance. This ultrafast electronic information is also critical for designing dye-molecules with HOMO-LUMO (highest-occupied and lowest-unoccupied molecular orbital) states that are better aligned with the semiconductor energy bands, in order to ensure near-100% photon-to-electron conversion efficiency.

Chapter 2 introduces the working principle behind DSCs and gives a brief review of the pros and cons of this technology compared to silicon-based photovoltaics. A brief literature review about the different charge transfer processes that take place in DSCs under working conditions has been presented. The main focus of the results presented in this thesis is on sub-picosecond charge dynamics measured using OPTP spectroscopy. The technique has been introduced in the latter half of the chapter, describing the basic concept and advantages of using terahertz spectroscopy.

The first half of Chapter 3 is devoted to a detailed description of how DSCs are fabricated and characterized using standard PV-related techniques. In the latter half, the experimental technique of terahertz pump-probe spectroscopy has been described in detail. Both the experimental set-up and the data-analysis methods have been discussed, using a case-study based on photoconductivity measured in a nanostructured TiO_2 film photoexcited at 400 nm using the 40 fs 1 KHz pulse train from a high power ultrafast laser system.

Compared to typical optical pump-probe spectroscopic techniques, optical-pump terahertz-probe spectroscopy (OPTP) measures change in conductivity within the photoexcited sample, which is a function of the charge carrier density and mobility. In chapter 4, the technique has been used to explore photoinduced conductivity dynamics in mesoporous anatase TiO_2 films commonly employed as the electron-transporting electrode in DSCs. This measured photoconductivity signal is then used to calculate the intrinsic electron mobility in the nanostructured semiconductor. In addition, the sub-nanosecond time-scale electron injection kinetics in TiO_2 films sensitized with a ruthenium dye, Z907 (Appendix B), have also been measured and discussed in detail.

Chapter 5 reports OPTP and photovoltaic device measurements conducted on three different metal-oxides used in DSCs: ZnO, TiO_2 and SnO_2. All films are sensitized with Z907 dye and photoexcited at 550 nm, and the charge injection dynamics and electron mobility have been compared. This is followed by a detailed discussion about the possible reasons and implications for the observed differences.

While conducting THz spectroscopic measurements on dye-sensitized SnO_2 films, a very interesting and repeatable light-soaking effect was observed, whereby there was a monotonic increase in the charge injection rate and peak photoconductivity over time, until steady state was achieved. This corroborated with photovoltaic measurements done on solid-state DSCs fabricated using the same SnO_2 paste. An in-depth study of this phenomenon was then conducted, and the findings have been reported in Chapter 6. It appears that light-soaking, with or without the presence of a UV component, causes a rearrangement of charged species at the dye-sensitized heterojunction, making forward electron transfer more favourable. The overall result is an improvement in both short-circuit current and device efficiency with exposure to light.

Finally, Chapter 7 gives a summary of the work described in this dissertation, along with an outlook and future experiments that could extend the experimental findings reported herein.

Chapter 2

Electronic Processes in Dye-Sensitized Solar Cells

This thesis focuses on time-resolved THz pump-probe measurements conducted on materials used in dye-sensitized solar cells (DSCs), in order to quantitatively understand the early-time electronic mechanisms that take place inside a liquid-electrolyte or solid-state DSC. This chapter introduces the concept of DSCs by detailing the working principle, device architecture and charge transfer processes associated with the device under working conditions. The motivation behind using optical pump terahertz probe (OPTP) spectroscopy has also been explained, by detailing the concept and advantages of using this technique and the complementary information it can provide, compared to other pump-probe pump-probe experimental techniques.

2.1 Harvesting solar energy

Solar cell performance is measured in terms of the percentage of incident light energy that is successfully converted into electricity. The current PV market is primarily dominated by silicon photovoltaics, with efficiencies up to 25% [11]. Despite high power conversion efficiencies, this technology is limited by very high manufacturing costs due to an unavoidable energy-intensive fabrication protocol. Additionally, the silicon panels are not easy to integrate into the built environment. This turns out to be a deterrent for architects and building planners when considering the possibility of harnessing solar energy in a residential area in an aesthetically pleasing manner.

Several second- and third-generation photovoltaic technologies are being researched intensively, to provide an alternative or companion solution to the silicon PV technology. These include thin film technologies such as amorphous Si, CdTe (cadmium telluride), CIGS (copper indium gallium selenide), organic solar cells, quantum dot cells, tandem/multi-junction cells, etc. Dye-sensitized solar cell (DSC) technology, pioneered by Prof Michael Grätzel at École Polytechnique Fédérale de Lausanne in 1991 [7], is another prominent thin-film technology with certified device efficiencies demonstrated at ∼11% [11]. Other advantages include cheap and easy fabrication and optical transparency.

The work shown in this thesis has been done to support DSC research. Photovoltaic measurement and optical pump-probe experiments have been used to probe different nanostructured semiconductor materials used for DSC fabrication, in combination with different dyes. The motivation is to understand the inherent charge dynamics in working DSC devices and, therefore, to enable improvement in overall device performance. With this aim, the DSC technology is described in detail in the following sections, including a brief literature review about the current status of understanding of the electronic processes that take place in DSCs during operation.

2.2 Dye-sensitized solar cells (DSCs)

2.2.1 Working principle and device structure

The DSC working principle is shown in Figure 2.1. At the heart of the device is a mesoporous metal-oxide film with a layer of sensitizer dye adsorbed on it [10, 12]. Incident sunlight is absorbed by the dye molecules, causing electrons to be excited from the dye ground state into its excited states. A favourable energy difference causes these electrons to be transferred into the conduction band (CB) of the semiconductor, thus converting solar energy into electricity. These electrons then diffuse through the interconnected matrix formed by the sintered semiconductor nanoparticles towards the conductive glass electrode where they are collected by the external circuit, as depicted in the figure. Meanwhile, the ground state of the dye is restored by transporting the positive charge from the oxidized dye molecules to the cathode via a redox electrolyte or an organic or inorganic hole transporter material (HTM). Both the dye-regeneration and hole-transport steps need to be fast enough to prevent the

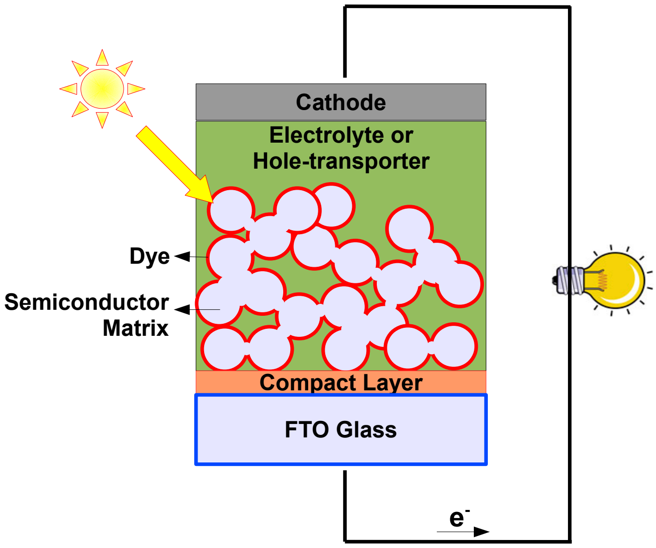

Figure 2.1: Schematic of a dye-sensitized solar cell (DSC). The greyish circles represent the mesoporous semiconductor matrix, covered with approximately a monolayer of dye molecules (depicted by the red outlines of the nanoparticles). Detailed device construction can be seen in Figure 3.2 (liquid-electrolyte DSCs) and Figure 3.3 (SDSCs).

electrons in the semiconductor from recombining with the holes in the dye or electrolyte/hole-transporter material (HTM). This cyclic electronic process can sustain millions of turnovers, ensuring long-lived devices [13].

Sensitization of wide band-gap semiconductors using dyes has a long history, dating back to the early days of photography in the 19th century. Systematic mechanistic studies were started much later with research on photoelectrochemical and photosynthetic cells in the late 1960s [13]. Most of these early studies were fundamental in nature, aimed at understanding electron transfer processes involving valence and conduction bands of a semiconductor immersed in a redox electrolyte. A significant landmark achievement in the design of DSCs was the replacement of the flat metal-oxide layer with a mesoporous film made with sintered nanoparticles [7, 14]. This resulted in as much as a 100-fold increase in surface area per micrometer thickness as compared to flat films. Higher surface area allows a higher density of dye molecules to be adsorbed on the metal oxide surface, resulting in much improved light harvesting by the photovoltaic device. Further drastic improvements were made by the development of stable metal-organic sensitizers bearing attachment groups which enable the dye molecule to be chemically bonded to the semiconductor surface, thus improving charge injection [12, 15, 16]. Over the past many years, numerous research groups have been working at optimizing different aspects of the DSC architecture in order to maximize the light to electricity conversion efficiency.

2.2.2 Advantage over traditional silicon-based solar cells

Silicon photovoltaic cells currently dominate the commercial photovoltaic market, with efficiencies ranging between 10% to 25% depending on the technology [11]. The high efficiency panels preferably employed for large scale applications are fabricated using monocrystalline silicon, which requires a notoriously expensive fabrication process, in terms of both energy and cost. Polycrystalline silicon solar panels are cheaper to manufacture, but the performance-cost trade-off is not in their favour and they have had limited success in displacing monocrystalline PVs from the market. In comparison, DSCs currently exhibit a certified performance at ~10% ($17\,\mathrm{cm}^2$ sub-module) [11] which makes them a viable competitor. In addition, DSC fabrication should be extremely cheap, since it does not require an ultrahigh purity semiconductor nor cleanroom conditions for fabrication. Si PV technology is quite mature, while extensive research is being carried out in the DSC area, and further leaps in performance are expected over the next few years.

Compared to Si PVs, DSCs exhibit a higher efficiency under non-direct sunlight and cloudy conditions (diffuse sunlight) [10, 12]. This is because electron-hole recombination in Si PVs is a strong function of the operating charge density condition. At very low charge densities, the probability of recombination is much higher. Hence they have a significant illumination cut-off level below which they are ineffective. On the other hand, in case of DSCs, since the charge generation part (sensitizer dye) is separate from the charge transport part (semiconductor, electrolyte), the recombination rate is much less dependent on charge density. DSCs, therefore, work well under low light conditions, and there is also a strong potential market for employing DSCs in indoor conditions.

All semiconductors suffer from decreasing open-circuit voltage as the operating temperature increases (negative temperature coefficient) [17, 18]. This results in poor device performance in summers or in hot countries, especially in the case of thick Si PV panels. DSCs, consisting of a very thin semiconductor film, can lose this heat via radiation and convection, keeping the operating temperatures much lower. This helps maintain higher performance levels in DSCs as compared to Si PVs [13].

Finally, another critical distinction between the two technologies results from the fact that DSCs can be optically transparent in the visible range and can be coloured in the desired wavelength range by selecting the appropriate dye sensitizer or combination of dyes. This makes them aesthetically pleasing, and they can be a good choice for Building Integrated PVs (BIPV).

Certified efficiencies of 10.9% and 9.9% have been demonstrated in small and large area liquid electrolyte DSCs respectively [11]. Very recently, Grätzel *et al.* reported an efficiency of 12.3% measured on DSCs fabricated from TiO_2 co-sensitized with Y123 and YD2 dyes and filled with a Co^{2+}/Co^{3+} electrolyte [19]. Also, certified efficiency of 6.08% was demonstrated recently in a solid-state DSC fabricated using TiO_2 sensitized with an organic dye molecule, labelled C220, with spiro-OMeTAD as the hole-transporter [20].

2.2.3 Issues with liquid-electrolyte DSCs

Despite the promising performance of redox-electrolyte based DSCs, the presence of the reactive and volatile electrolyte presents significant challenges for the mass-production and long-term stability of these devices, making them unsuitable for commercial application [10, 21–23]. The electrolyte tends to corrode even inert metal contacts such as gold and silver over time, causing the devices to fail in a relatively short time period. In addition, the electrolyte exhibits serious temperature stability issues. It can freeze at low temperatures and expand significantly at high temperatures, thus adversely affecting the device sealing and even causing physical damage to the panels. The use of redox electrolyte places very tight constraints on the design and selection of suitable encapsulants which are inert towards the corrosive iodide/triiodide redox couple-based electrolyte, and impermeable towards the electrolyte solvent. The complicated hermetic sealing step counteracts the commercial success of DSCs by lowering the performance/price ratio.

Various alternatives are being explored to circumvent the issues arising from the use of the redox electrolyte. These include replacing the redox iodide/triiodide system with a cobalt(II)/(III), copper(I)/(II) or ferrocene/ferrocenium redox couple [12, 16, 19, 24–26], using viscous ionic liquid electrolytes [27, 28], thixotropic electrolytes [29], or solid-state hole-transporters which may be either inorganic [30, 31] or organic [32, 33]. Since the device work reported in Chapters 4 and 6 is based on DSCs with an organic hole transporter material (HTM), this concept is described in more detail in the next section.

In addition, extensive efforts are also on-going for optimizing other components of the DSC in order to improve device efficiency, lifetime, processability and cost. These include developing alternate metal oxides such as SnO_2, ZnO, Nb_2O_5, WO_3 etc. [12, 13, 34–37]; different metal-oxide morphologies such as core-shell structures [38, 39], nanowires and nanotubes [24, 40, 41], copolymer-assisted self-assembled structures [42, 43]; alternate sensitizer dyes especially organic structures [44–46] etc. In all such material optimization studies, there is an increasing appreciation that changing any one material component of the device stack can affect the performance of other material components, and thus, any such material change experimentation needs to be accompanied by detailed functional studies to be able to draw unambiguous conclusions.

2.2.4 Solid-state DSCs (SDSCs)

As mentioned above, one way of circumventing the issues arising from the use of a corrosive electrolyte in DSCs is to replace it with a solid-state hole transporter. This idea was successfully demonstrated in 1998 by Bach *et al.*, who employed an organic HTM molecule spiro-OMeTAD (2,2',7,7'-tetrakis(N,N-di-p-methoxypheny-amine)-9,9'-spirobifluorene) (molecular structure shown in Figure 2.2), resulting in a hybrid (organic/inorganic) fully electronic solid-state DSC (SDSC) [32]. Typically, the hole transporter is dissolved in a suitable solvent and deposited on the dye-sensitized semiconductor film on a transparent conductive oxide

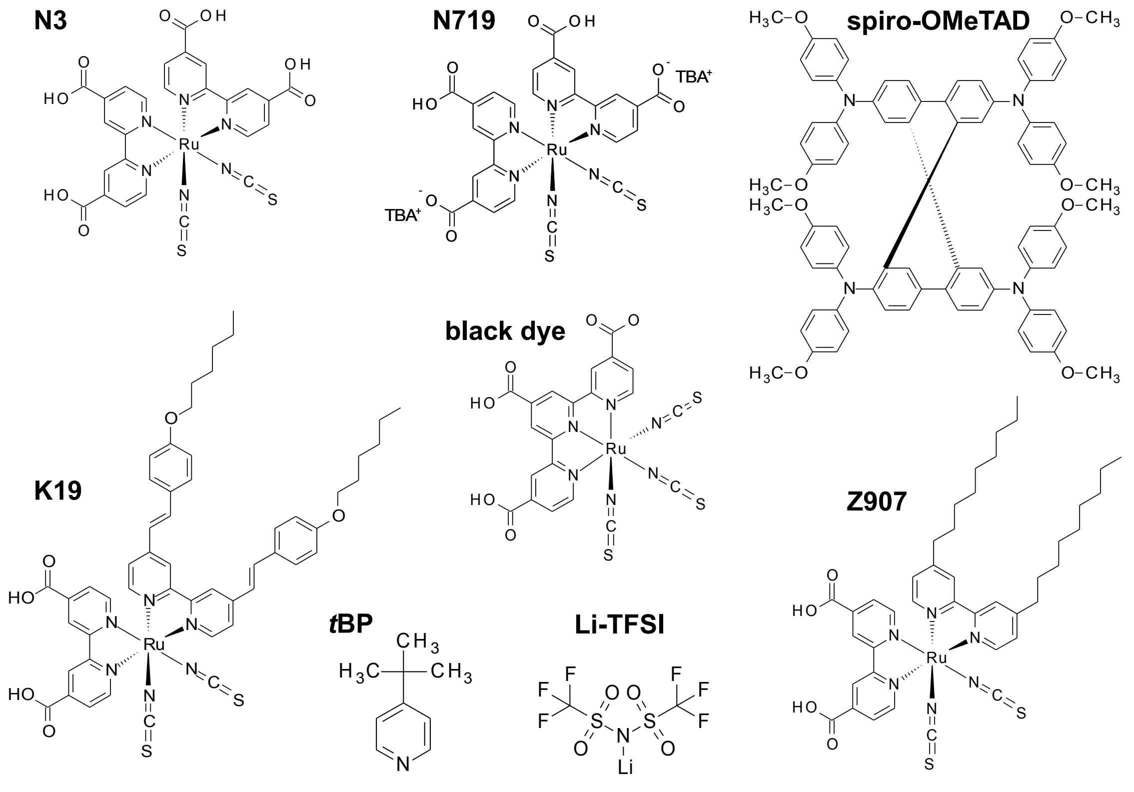

Figure 2.2: Molecular structures of the most successful ruthenium-based dye sensitizers: N3, N719, Z907, K19 and "black dye". Also shown are structures of spiro-OMeTAD hole-transporter (2,2',7,7'-tetrakis(N,N-di-p-methoxypheny-amine)-9,9'-spirobifluorene) and commonly used additives in DSCs: *tert*-butyl pyridine (*t*BP) and bis(trifluoromethyl-sulfonyl)amine lithium salt ($Li[CF_3SO_2]_2N$) (Li-TFSI).

(TCO) substrate via spin-coating. After the solvent has evaporated, a solid film infiltrated into the semiconductor matrix is left behind, posing no risk of leakage or corrosion. Over the years spiro-OMeTAD is still a favourite because of its respectable charge carrier mobility ($\sim 10^{-4}\,\mathrm{cm}^2/(\mathrm{Vs})$) [47, 48] and high solubility in a range of solvents [10]. The latter property enables good infiltration of the molecule into mesoporous semiconductor matrix of up to at least 5 microns thickness [49, 50]. There has been extensive debate about spiro-infiltration in recent literature, since this has been assumed to be the bottle-neck for SDSC performance for some years [10]. It has been shown in recent work that sufficient infiltration takes place successfully, thus ruling out this factor as the main limiting factor for the observed lower performance of SDSCs compared to liquid electrolyte DSCs [49, 50].

Electronically, once electrons are successfully injected from the dye LUMO states into the metal oxide, holes are created in the dye HOMO states, which are transferred to the hole-transporter. The holes are then transported via hopping between electronic states on the organic molecules to the anode (counter-electrode) (Figure 2.1). The details of the involved charge transport processes are described in Section 2.3.3, and the device construction is described in more detail in Section 3.1.6.

2.3 Electronic processes in DSCs

2.3.1 Overview

A schematic of the DSC has already been shown in Figure 2.1 showing a typical device structure. Figure 2.3 shows the basic electron transfer processes that take place inside a working DSC, for the illustrative case of a TiO_2-based liquid electrolyte device with N3 dye (Figure 2.2) and I^-/I_3^- redox couple [10, 12, 16, 51]. Absorption of photons by the dye molecule results in electrons getting excited from the dye ground states into the excited LUMO states. The desirable electron transfer pathway is indicated by processes 3,4,5,8 whereby electrons injected from the dye excited states into the semiconductor conduction band (CB) are successfully collected at the anode (working electrode) while the oxidized dye is regenerated by the redox electrolyte, thus completing the electrical circuit. These favourable electronic processes have to compete with loss mechanisms indicated in the figure. Process 2 is the direct recombination within the dye molecule, measured by the dye excited state lifetime. Processes 6 and 7 represent the recombination of the mobile electrons in the semiconductor CB with the oxidized dye or acceptors in the electrolyte, respectively. The high degree of intimate contact between the porous metal-oxide film, dye and electrolyte greatly increases the probability of these recombination mechanisms, and can only be avoided by ensuring that the separated charges (electrons and holes) are collected at the respective electrodes as soon as possible.

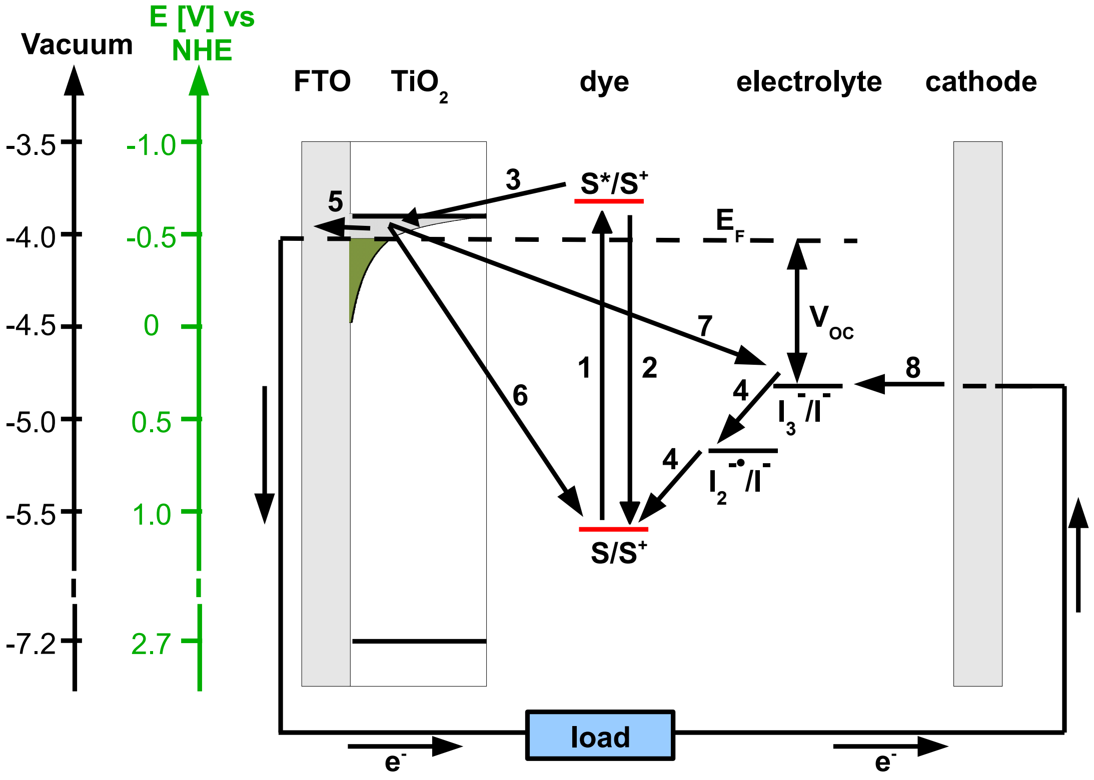

Figure 2.3: Schematic energy diagram for the electronic processes and main loss mechanisms in a typical DSC based on TiO_2, N3 dye and I_3^-/I^- redox electrolyte. The energy scale is indicated in electron volts using both NHE (normal hydrogen electrode) and vacuum level as a reference. Process 1: incident light causes electrons to be excited into the dye excited states; Process 2: dye excited state decay; Process 3: electron injection into semiconductor conduction band; Process 4: dye regeneration by electrolyte; Process 5: electron transport through semiconductor towards electrode; Process 6: recombination of injected electrons with oxidized dye; Process 7: recombination of electrons with acceptors in electrolyte; Process 8: transport of holes towards cathode. More details are given in Section 2.3.3 and the respective time-scales for each process are shown in Figure 2.5.

The device open-circuit photovoltage V_{OC} corresponds to the free energy difference between the working and counter-electrodes. In the dark at equilibrium, the Fermi energy level of the TiO_2 electrode equilibrates with the midpoint potential of the redox couple, resulting in zero voltage [51, 52]. The TiO_2 Fermi level lies deep within the semiconductor bandgap at this point. Photoexcitation results in electron injection into the TiO_2 conduction band and accompanying hole injection into (or, oxidation of) the redox electrolyte. On illumination, there is no significant change in the chemical potential of the electrolyte from its 'dark' value because of a high concentration of both oxidized and reduced species of the redox couple at any given time. On the other hand, electron injection into the TiO_2 CB significantly increases the electron density from $1\times10^{13}\,\mathrm{cm}^{-3}$ to $1\times10^{18}\,\mathrm{cm}^{-3}$ [51]. The TiO_2 Fermi level is, therefore, raised towards the conduction band edge. This leads to an increase in the stored overall free energy of electrons in the system, thus inducing a photovoltage in the external circuit. In other words, the device V_{OC} is governed by the difference between the quasi-fermi level of electrons in TiO_2 under illumination and the Fermi level of the electrolyte, as indicated in Figure 2.3 [52].

The following detailed description of electronic processes taking place inside DSCs has been roughly divided into two parts; the first part focuses on the energetics of different components of a DSC, and the latter part reviews the kinetics and time-scales of the charge transfer processes indicated in Figure 2.3. This section is intended to serve as an introduction rather than an extensive review on the subject, and borrows from some excellent reviews published over the past few years [10, 12, 16, 51–53]. The main focus of the experimental work reported in the following chapters is on the sub-nanosecond time-scale charge carrier dynamics in DSCs. Accordingly, the early-time electron injection and electron transport mechanisms in dye-sensitized semiconductor films have been reviewed in greater detail than other electronic processes.

2.3.2 Energetics of operation

Energy levels in semiconductor

The charge transport environment provided by a randomly interconnected mesoporous semiconductor film is significantly different from that in a conventional silicon solar cell fabricated from high purity silicon crystals with carefully controlled doping levels. An essential difference is that instead of travelling through the conduction band, electrons have to travel via hopping or tunneling from one crystallite to another [12, 16]. The inherent conductivity and carrier mobility of these porous films composed of nanoparticles is much lower than that for a continuous film because of grain boundaries, surface traps and bulk traps. In addition, the porous semiconductor matrix has an enormous irregular surface area which is inhomogenously exposed to different species such as the dye molecules, redox molecules and additives. All these factors drastically increase the complexity of modeling charge tranport characteristics of mesoporous electrodes employed in DSCs.

The best performing electrode in DSCs so far is nanostructured TiO_2. While TiO_2 exists in several different crystal forms naturally: rutile, anatase, and brookite, the preferred structure in DSCs is anatase because of its larger band-gap (3.2 eV vs 3.0 eV for rutile) and a higher conduction band edge, E_c [12, 54]. This enables DSC devices with a higher V_{OC}. Despite rutile being the more stable crystal structure, anatase is more suitable for DSC application morphologically because of larger interconnects between nanoparticles thus enabling faster electron transport [52]. The current understanding about nanostructured TiO_2 is that E_c is not very well-defined [55, 56]. With a band-gap of 3.2 eV, the ground state UV-Vis spectrum of anatase TiO_2 shows a fundamental absorption edge at 385 nm with an absorption tail extending to longer wavelengths [13, 55, 57]. Based on various electrochemical, photochemical and spectroscopic studies, it has been concluded that mesoporous nanocrystalline TiO_2 thin films possess a tailing of acceptor density of states (DoS) rather than an abrupt onset from an ideal E_c [10, 16, 56, 58]. The trap-density forms an exponential tail below the conduction band containing $\sim$30 traps per nanoparticle, where the typical nanoparticle diameter is about 20 nm [59]. The inset of Figure 2.4 a) shows this distribution graphically, as measured by Bisquert *et al* [56]. While the traps are primarily due to defects in the bulk of the semiconductor crystal structure, various experiments have also confirmed the presence of a significant population of deep, surface trap states in TiO_2 nanostructured electrodes, at an energy located within the bandgap [12, 16, 56, 60]. The small peak observed below the conduction band edge in the inset of Figure 2.4 a) has been attributed to surface states in mesoporous TiO_2 [56], believed to be unsaturated Ti^{IV} surface states formed due to oxygen vacancies [16]. Both types of trap-states have been shown schematically in Figure 2.4 b). The figure also shows schematically the relationship between the energy states in N3 dye and TiO_2 nanoparticles, based on experimental results [16, 56, 58]. The electron quasi-Fermi energy level, E_F, is not fixed; rather it depends on factors such as the illumination intensity and applied bias, and is discussed in more detail in Section 2.3.3.

This model of energetics in nanostructured TiO_2 has been used successfully to explain non-exponential electron injection dynamics observed in Ru dye/TiO_2 systems, and to argue that electron transport takes place through a multiple-trapping, continuous-time random walk mechanism [59, 61–63].

The band-energetics described above are not an inherent property of the material and can be tuned by altering the ionic content of the medium surrounding the nanoparticles. Many studies have reported that the adsorption of molecules or ions with varying Lewis acidic or basic character compared to Ti^{IV} can cause a shift in E_c and E_F [16, 51, 60]. For instance, Hagfeldt *et al.* [58] have shown experimentally an increase in the number of trap sites within the bandgap on inserting Li^+ ions within nanostructured TiO_2. The data has been reproduced in Figure 2.4 a). Increasing the concentration of ions or protons adsorbed on the TiO_2 surface alters the surface charge of the metal-oxide, resulting in interfacial dipoles [51]. This changes the energetics of the metal-oxide acceptor states relative to the dye excited state energy level, thus affecting the electron injection process. Additives commonly used to influence energetics include Li^+ and *t*BP (tert-butylpyridine) salts, shown in Figure 2.2. For example, while the CB edge of TiO_2, E_c, in 0.1 M $LiClO_4$ acetonitrile electrolyte has been

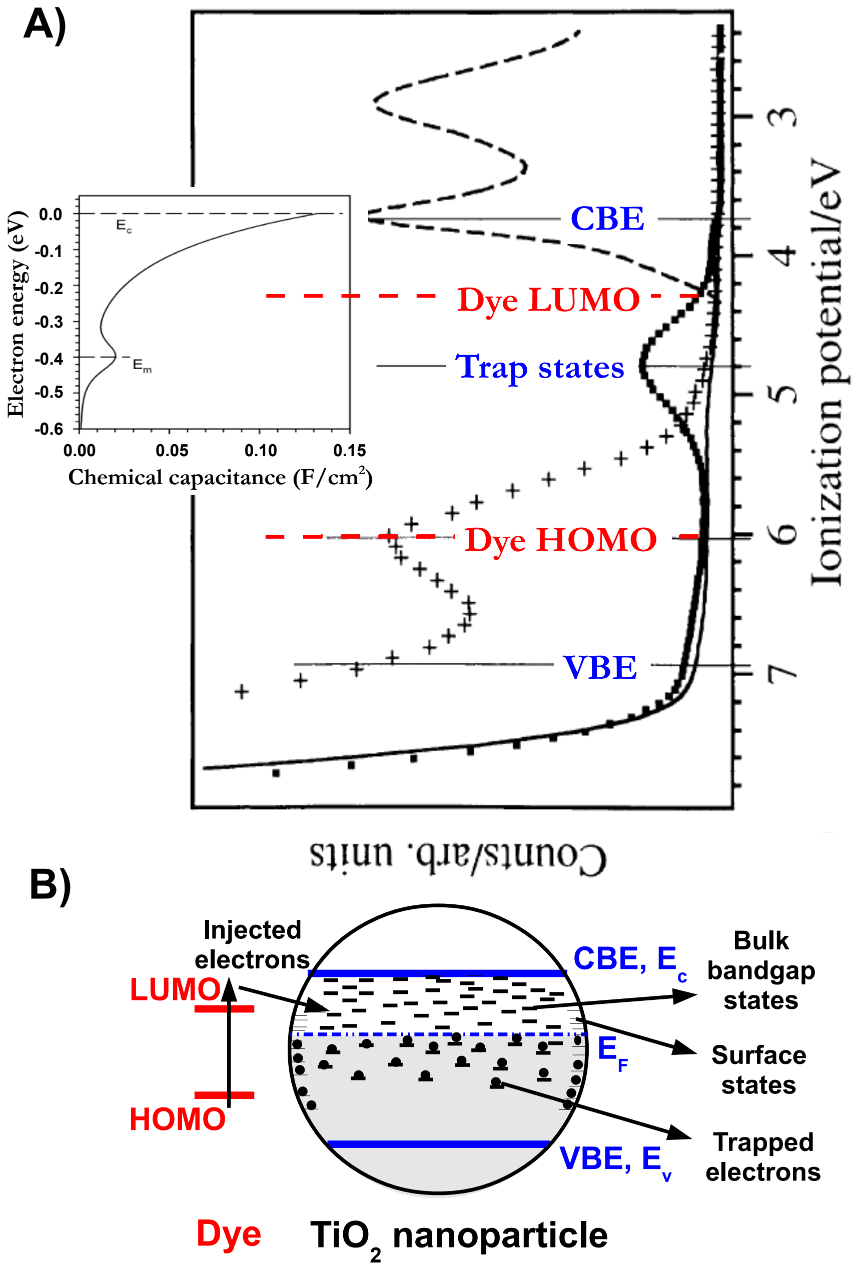

Figure 2.4: A) The electronic density of states (DoS) of nanostructured TiO$_2$ (solid line), TiO$_2$ sensitized with N3 dye (crosses), and TiO$_2$ inserted with Li$^+$ ions (boxes), measured with photoelectron spectroscopy [58]. See Figure 2.2 for the chemical structure of N3 dye. Overlaid is the absorption spectrum of N3 dye (broken line), with the absorption maximum of the dye at 535 nm corresponding to 2.32 eV above the maximum of the HOMO peak. INSET: Exponential distribution of DoS below the TiO$_2$ CB edge, measured by electrochemical methods [56]. The figures have been scaled so as to align the energies of the (surface) deep trap states, exponential DoS near the conduction band, and the conduction band edge; however, the energy differences among these states are dissimilar. Adapted from Figure 9 of Ref 16. The spatial location of these energy states within a TiO$_2$ nanoparticle are shown schematically in B), as a function of their energy with respect to the conduction band edge E$_c$, according to my understanding. Typical TiO$_2$ nanoparticle diameter is ~20 nm.

reported to be -0.76 V vs NHE (normal hydrogen electrode), it changes to -1.76 V when Li^+ is replaced by TBA^+, the tetrabutylammonium counterions in N719, the deprotonated form of N3 dye [16] (Figure 2.2). Similarly, Hagfeldt *et al.* measured an increase of 0.16 eV in V_{OC} due to the addition of *t*BP [12].

Based on the above discusion, it can be concluded that any mesoporous metal-oxide electrode, TiO_2 or otherwise, needs to fulfill certain requirements to enable high performance DSCs:

1. Wide band-gap so that there is minimal spectral overlap between semiconductor and dye

2. CB edge suitably situated with respect to the dye excited state energy level to ensure rapid electron injection

3. High electron mobility

4. Large surface area to ensure sufficient dye coverage for efficient light harvesting

Energy Levels of Redox Systems in Solution

The midpoint potential of the redox couple is given by the Nernst equation, and is therefore a function of the relative concentrations of both iodide and iodine, in case of I_3^-/I^- redox electrolyte [12, 64]. The respective concentrations are chosen so as to optimize the rates of dye regeneration at the working electrode and iodide regeneration at the counter electrode. Details of the reaction are given in Section 2.3.3. Typical concentrations are in the range of 0.1–0.7 M iodide and 10–200 mM iodine [64]. The resulting midpoint potential of the electrolyte is at ∼0.3 V vs NHE. Excess iodide in the solution leads to the formation of I_3^- which is why the electrolyte is referred to as an iodide/triiodide redox couple.

Energy levels in excited dye molecules

The most successful DSC systems consist of a ruthenium polypyridyl complex adsorbed on a metal-oxide mesoporous matrix. Some popularly used dyes are shown in Figure 2.2. These dyes can typically be described as a donor-bridge-acceptor unit with a chromophore (electron donor) anchored on the surface of semiconductor nanoparticle (electron acceptor) through a molecular spacer and anchoring group (bridge) [53]. Optical excitation of the chromophore promotes electrons from the Ru metal centre and the sulfur atom to the carboxylated bipyridyl ligand which is directly bound to the semiconductor surface. In TiO_2/Ru dye DSCs, electron injection therefore takes place from the π^* orbitals of the organic ligand to the conduction band acceptor states of the metal-oxide, which in case of TiO_2 are its unfilled d orbitals [16]. This injection process competes with the dye recombination process, whereby electrons that are too slow or less energetic for transfer into the semiconductor recombine with the dye cations.

The energetics in both inorganic and organic dyes have been reviewed in great detail in a recent review by Meyer *et al* [16]. For efficient photovoltaic performance, the ideal dye sensitizer molecule needs to fulfill the following conditions [12, 16]:

- The absorption spectrum of the dye should cover a large part of the visible and near-IR spectrum in order to harness a significant amount of the incident light.
- The dye LUMO energy state should be higher than the semiconductor CB edge to ensure a sufficiently high electron injection yield.
- The oxidized energy state of the dye should be more negative (with respect to vacuum, see Figure 2.3) than the redox potential of the electrolyte to enable rapid dye regeneration.

The molecular structure of the dye can be optimized to maximise electron injection and minimise recombination. For instance, the presence of an anchoring group such as -COOH, -H_2PO_3, -SO_3H etc. promotes strong binding with the semiconductor surface, thus facilitating fast electron transfer. This also improves long-term stability by reducing dye desorption. Desorbed dye molecules also lead to an undesirable filter effect and a decrease in the counter-electrode performance [12]. Ideally, the dye should form a closely packed monolayer adsorbed on the semiconductor nanoparticle, blocking direct contact between the semiconductor and redox electrolyte. Dye aggregation should be negligible to maximise quantum yield of electron injection. This is sometimes achieved by adding bulky side-chains on the molecule which constraints the orientation of the dye molecule with respect to the semiconductor surface. This has been successfully demonstrated in Z907 dye shown in Figure 2.2 [65]. The dye should also have a favourable interaction with the hole-transporting medium, in order to ensure rapid regeneration of the dye. This can be enhanced by the presence of suitable functional groups on the dye molecule [12].

The dye excited state decay time should be sufficiently long to allow for most of the excited electrons to be injected into the semiconductor conduction band instead of decaying back to the dye ground state. Usually this is about a few tens of nanoseconds in case of well-performing dyes, as described in Section 2.3.3. In addition, the lifetime of the dye oxidized state should be at least in the range of $\sim 100\,\mathrm{s}$ [66]. Given that the dye regeneration time in a typical TiO_2/Ru-dye/iodide electrolyte is in the microsecond time-scale, as discussed in Section 2.3.3 (Figure 2.5), this would allow the dye to sustain more than 10^8 cycles of photoexcitation, electron injection and regeneration, equivalent to 20 years of sustained perfomance under outdoor illumination conditions [13, 66]. Finally, the dye molecule should be stable at elevated operating temperatures.

2.3.3 Kinetics of operation

This section briefly summarizes the current understanding about the kinetics of the various electronic processes that take place within a working DSC. Most of the results reviewed here have been measured using femtosecond and nanosecond resolution transient absorption spectroscopy (TAS) techniques [67]. Each of the reactant and product species involved in different interfacial charge transfer dynamics has a characteristic spectral signature, which can be monitored to follow the photoinduced dynamics in dye-sensitized systems [53, 68–70]. After excitation at a suitable wavelength, the photoexcited system can be probed over a wide wavelength spectrum spanning across visible, infra-red (IR), and even up to terahertz and microwave wavelengths. Probing with visible/near-IR wavelength detects electronic transitions within the system, and has been successfully implemented over the years for measuring ultrafast electronic mechanisms taking place inside DSCs. For instance, the electron injection phase can be studied by monitoring the rise of the photoinduced absorption signal for the dye cation or the injected electrons. However, the primary drawback of probing in this wavelength range is the spectral overlap between the broad absorption bands of different species, such as the ground, singlet, triplet, and oxidized states of the dye [68, 71, 72]. To identify each charge species unambiguously, it is often necessary to probe over a wide spectral range to separate the dynamics of different absorbing species [68, 73], significantly increasing the complexity of the experimental set-up.

In comparison, transient mid-IR spectroscopy can simultaneously measure the dynamics of both the injected electrons and adsorbates by monitoring the mid-IR absorption of free or trapped electrons and holes, and also the vibrational transitions of the adsorbate in its ground, excited and oxidized states [35, 74, 75]. Probing at even longer wavelengths such as in the terahertz and microwave region requires a much different experimental set-up compared to optical pump-probe techniques, but it directly yields information regarding the dynamics of electrons or holes within the probed system, without the need for complicated post-experimental data-analysis. Time-resolved microwave conductivity (TRMC) spectroscopy has a nanosecond time resolution while THz spectroscopy can achieve a resolution of up to a few tens of femtoseconds. In addition to directly and unambiguously mapping the ultrafast charge carrier dynamics, THz spectroscopic measurements can also indicate the nature of charge carriers within the system, whether they are free or bound charge-carriers. The main shortcoming of optical spectroscopy techniques that probe in the long wavelength region (mid-IR to microwave) is the difficulty in probing systems that inherently absorb strongly in this part of the spectrum, such as in an aqueous or ionic medium.

The main focus of the work shown in this thesis is on using THz pump-probe spectroscopy for measuring sub-nanosecond duration charge transfer mechanisms taking place within DSC systems. The experimental technique and its advantages have, therefore, been described in great detail in the latter half of this chapter (Section 2.4) and in Chapter 3. While experimental studies published by other research groups have been discussed in the following chapters where relevant, an overall brief review is presented here detailing the current understanding about the various charge transfer kinetics taking place within DSCs. The approximate time-scales for these processes have also been summarized in Figure 2.5 for quick reference.

Process 1–3: Electron injection and excited state decay

It is now generally agreed within the DSC community that, for the case of a dye-semiconductor system exhibiting respectable photovoltaic performance, electron injection from the dye excited state into the metal-oxide conduction band is usually ultrafast, with half-times ranging between ∼100 femtosecond to a few hundred picoseconds, as shown in Figure 2.5 [71, 76, 77]. While this is beneficial, an ultrafast injection rate is not a critical factor for an efficient DSC [12, 51]. Rather, it is essential to achieve a high quantum efficiency for injection (quantum yield), which is possible only if the injection time is at least a couple of orders of magnitude faster than the decay time of the excited state of the dye to its ground state [12], indicated by process 2 in Figure 2.3. This excited state lifetime, including both the radiative and non-radiative decay rates, is typically in the 1–100 ns range for ruthenium-complexes [78, 79]. If the injection rate is much higher, this leads to “kinetic redundancy” in the system, as proposed by Durrant *et al* [51, 80, 81]. According to this philosophy, the charge separation kinetics should be just fast enough to compete successfully with the dye excited state decay, thus enabling a high injection yield while minimizing the probability of interfacial charge recombination.

Numerous research groups have reported multi-exponential electron injection dynamics in the case of TiO_2, ZnO or SnO_2 mesoporous films sensitized with various dyes [35, 36,

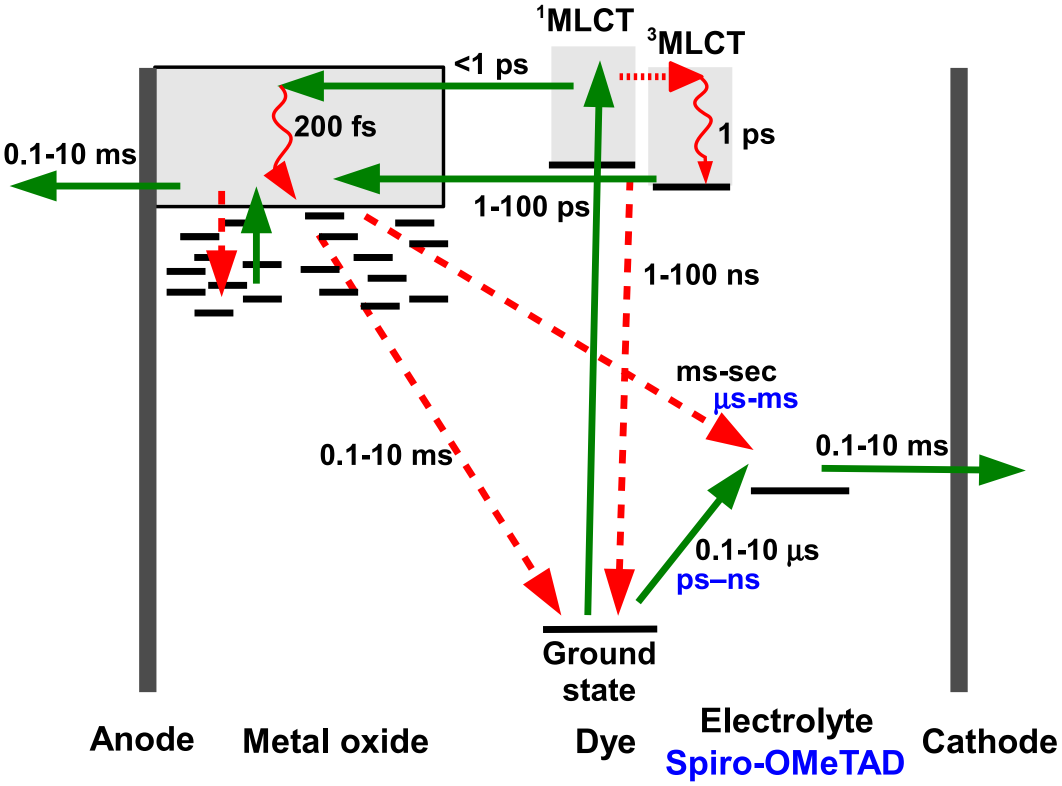

Figure 2.5: Schematic energy diagram of a typical DSC device (TiO_2, N3 dye, I_3^-/I^- electrolyte), showing the approximate time-scales for the different charge transfer mechanisms. Recombination processes are indicated by red broken arrows. Red wavy arrows depict thermalization of electrons. Corresponding time-scales in solid-state DSCs with spiro-OMeTAD hole transporter are indicated with blue labels. Details of energetics are shown in Figure 2.3.

72, 74, 75, 82–85]. Electron injection has been observed to be biphasic, with a fast sub-picosecond component, followed by a slower component which is sensitive to factors such as the electronic coupling between donor and acceptor orbitals, acceptor density of states (DoS), thermodynamic driving force, etc [35, 53, 77]. Furthermore, dye molecules adsorbed on a mesoporous semiconductor nanoparticle network offer an inhomogenous distribution of adsorbate/semiconductor interactions, furthur contributing to the multiexponential injection dynamics [35, 74]. Some of these factors are reviewed in more detail here.

Two-state injection model: The observed non-exponential electron injection dynamics have been attributed partly to the fact that electron injection can take place from various states in the thermal relaxation pathway in the dye molecular energetics [16, 53, 77]. As described earlier in Section 2.3.2, optical excitation of the dye results in metal-to-ligand charge-transfer (MLCT) excitation where an electron is promoted from a mixed Ru-NCS state to an excited π^* state of the dcbpy (4,4'-dicarboxy-2,2'-bipyridine) ligand, and then injected into the semiconductor conduction band [12, 16]. Electron injection can take place from the singlet ^{1}MLCT excited state within the first few hundred femtoseconds after photoexcitation, either before or after electron thermalization, as depicted in Figure 2.5. Remaining electrons, if any, undergo intramolecular relaxation via intersystem crossing to the triplet state(s) (^{3}MLCT) followed by vibrational relaxation, as shown by the red arrows in the figure. As mentioned above, the lifetime of the dye excited state is typically in the 1–100 ns time range and does not directly compete with the charge injection process in a well-optimized system. At 400 nm excitation, the energy difference between the initially excited singlet state and the relaxed triplet state in Ru bipyridyl molecules ranges between 1.0 to 1.6 eV [53]. Some research groups have argued that the extra charge transfer steps and the lower energy difference between the dye donor states and semiconductor acceptor states result in electron injection from the thermalized, triplet ^{3}MLCT excited state being much slower as compared to the faster injection from the ^{1}MLCT excited state, as shown in Figure 2.5 [70, 71].

Effect of driving force, ΔE_{inj}: The electron injection process depends on the energy difference between the dye LUMO energy level and the TiO_2 conduction band energy level. This explains why metal-oxides such as TiO_2, ZnO and SnO_2 are successful as electrodes in DSCs while no electron injection is observed in case of dye-sensitized Al_2O_3 or ZrO_2 [70, 86, 87]. TiO_2, ZnO and SnO_2 have band-gap values between 3.2–3.8 eV, as shown schematically in Figure 5.1 [88]. In comparison, both Al_2O_3 and ZrO_2 are considered as wide band-gap insulators, with the band gap varying between 7–9 eV for Al_2O_3 [89, 90] and 5–7 eV for ZrO_2 [91]. The CB edge of both these materials is, therefore, much higher than the dye excited state, making electron injection thermodynamically unfavourable.

A proton-induced shift in the semiconductor conduction band (CB) edge can result in faster or slower electron injection [12, 51, 55]. For instance, Durrant *et al.* have shown that the electron injection rate in N719-sensitized TiO_2 is almost 30-fold slower than in TiO_2/N3 [79]. N719 is a salt analogue of N3 dye with two of the four protons on the carboxylic groups replaced with TBA^+ (tetrabutylammonium) counterions, as seen in Figure 2.2. They have proposed that the presence of excess labile protons from the carboxylic acid binding groups of N3 dye causes the TiO_2 CB to be lowered, thus making electron injection energetically more favourable as compared to that in N719 dye. This was also confirmed by Lian *et al.* by probing injection dynamics in TiO_2/N3 in different pH aqueous buffer solutions - both the injection rate and yield decreased systematically as the pH was increased [12, 53]. This can be explained based on reports from the Meyer group that Ru sensitizers are bound to acid pre-treated TiO_2 films in the acid form, -COOH, and in the carboxylate form, -COO-, in case of base pre-treated TiO_2 films [16].

Another very popularly employed technique for influencing the semiconductor band edge is the addition of ions or salts in the medium surrouding the mesoporous film. This follows from the earlier discussion in Section 2.3.2. Addition of *t*BP to the electrolyte has been shown to cause a significant negative potential shift in TiO_2 (vs NHE), resulting in an increase in V_{OC} [12, 92]. This is attributed to the amine group charging the TiO_2 surface negatively by deprotonating it [52]. In contrast, adding cations such as Li^+ lowers the TiO_2 CB edge with respect to the dye LUMO energy level [16, 52, 93, 94]. This is because the small Li^+ ions get intercalated or strongly adsorbed to the TiO_2 surface. Tachibana *et al.* have reported a 7-fold increase in injection dynamics after adding 0.1 M Li^+ ions to the electrolyte [95].

The relative energetics of the dye excited state versus the semiconductor CB edge is a key determinant of electron injection dynamics in DSCs. It has been shown that a 100 meV shift in band edge can result in an approximately 2-fold change of injection dynamics [96]. However, it is important to note that a shift in E_c and E_F not only affects charge collection, but also the device V_{OC} (Figure 2.3). Addition of Li^+ is shown to cause a significant drop in device V_{OC} [51, 93, 94]. For optimal device performance, therefore, the band energetics need to be subtly controlled in order to achieve the maximum possible J_{SC} without sacrificing V_{OC}. For this very reason, TiO_2 devices with N719 dye mentioned above exhibit higher efficiency than with N3 dye [12, 80]; any loss in J_{SC} due to slower charge injection is more than compensated by higher V_{OC} in TiO_2/N719 DSC devices.

Effect of quasi-Fermi level in the semiconductor: The quasi-Fermi level is a function of electron concentration and is controlled by the filling of the density of states (DoS) in the semiconductor. The probability and, therefore, the yield of electron injection rate increases with an increase in the available acceptor DoS with energies just below the dye LUMO levels, as shown in Figures 2.3 and 2.4. The quasi-Fermi level can be manipulated by an applied potential or by exposing the device to sufficiently high light intensities [52]. Tachibana *et al.* showed that the application of an external electrical bias of -700 mV to TiO_2/N3 films in the presence of a redox-inactive electrolyte results in a 25-fold retardation of injection kinetics [95]. This was attributed to an increase in electron concentration within the TiO_2 reducing the density of unoccupied states available for electron injection.

A similar effect is observed when DSCs are exposed to high light intensities, whereby increased photoinjected electron concentration in TiO_2 leads to an upward shift in the electron quasi-Fermi energy level and therefore, significantly higher device V_{OC} [97]. While this has been shown to improve electron transport within TiO_2 [12] and leads to a higher recombination rate [10, 98, 99], there is not much literature regarding the direct relationship between injection dynamics and light intensity.

Effect of electronic coupling: While a favourable energy difference and a large acceptor DoS increases the probability of charge injection, the electronic coupling between the donor excited-state molecular orbitals and the acceptor orbitals is a critical factor that influences charge injection dynamics. For instance, it has been shown in various studies that electron injection is faster in N3-sensitized TiO_2 than in SnO_2 or ZnO sensitized with a similar ruthenium dye [74, 82, 83, 85, 100]. This has been attributed to the fact that the TiO_2 CB is mainly comprised of unfilled d orbitals while those of SnO_2 and ZnO possess a predominantly s-character, with less efficient orbital mixing with the carboxylate π system (shown schematically in Figure 8 of Ref 16). This is further discussed in Chapter 5 Section 5.3.1 where the reasons for significantly different charge injection rates in TiO_2, ZnO and SnO_2 are explored in detail.

Effect of dye aggregates: Wenger *et al.* reported monoexponential electron injection dynamics when the Ru dye sensitizer is adsorbed as a monolayer on the TiO_2 nanoparticles [77]. They observed that the absence of dye aggregates or any loosely attached dye molecules on the semiconductor surface results in charge injection being completed within the first 20 fs. However in a similar detailed study conducted on ZnO nanostructured films sensitized with a Ru-dye, Asbury *et al.* [74] concluded that dye aggregation does not affect electron injection rate. However, the overall injection yield is adversely affected by the presence of aggregates. This suggests that the aggregation or multilayer assembly of dye molecules inhibits successful electron transfer from all the dye molecules directly adsorbed on the semiconductor surface.

Effect of excitation wavelength: A high-performance DSC needs to achieve high photon-to-electron conversion efficiency over a wide wavelength range in the visible-to-near IR spectrum. It is, therefore, important to understand the effect of different excitation wavelengths on the electron injection mechanism. Absorption of photons with energies greater than the optical bandgap (e.g. blue photons) initially generates "thermally hot" excited states. Both the Lian and Sundström groups have reported faster electron injection with blue-shifted optical excitation, in case of TiO_2 sensitized with a ruthenium dye [53, 70, 101]. This fits with the two-state injection model described in Figure 2.5, whereby the fast component of electron injection takes place from the thermally unrelaxed ^{1}MLCT singlet excited state and the slow component from the vibrationally relaxed ^{3}MLCT triplet energy states. It is postulated that excitation in the near-IR wavelength range could populate the ^{3}MLCT states directly [101]. As the excitation wavelength increases, therefore, the contribution of the fast injection component decreases while the slower injection component remains unaffected. This is in agreement with the reported results, suggesting that the rate of electron injection is dependent on the initially populated electronic state; the higher the state, the faster the electron injection. It is also possible that excitation to higher energy states may change the electronic coupling between the dye donor states and TiO_2 acceptor states, responsible for faster electron transfer [70].

An interesting experiment was conducted by measuring injection dynamics in both TiO_2 and SnO_2 sensitized with the same ruthenium dye [102]. In case of TiO_2, APCE (absorbed photon to current conversion efficiency, Section 3.2.2) was wavelength-dependent with lower values in the longer wavelength regime. This was rationalized as injection from this lower energy band being thermodynamically less favourable. However, in contrast, in SnO_2, whose CB edge is lower than TiO_2 by $\sim$500 mV [13, 35, 36], no wavelength dependence of APCE was observed since electrons can successfully be injected from any state in the excited dye energy levels.

In contradiction to these measurements, the Tachiya and Durrant groups [86, 103] have reported that the electron transfer kinetics in Ru dye-sensitized TiO_2 are independent of the excitation wavelength. There could be several explanations for this. The much faster "hot" electron injection is probably only observed when the dye excited state is energetically much higher than the TiO_2 CB edge, for instance, in the presence of a high concentration of lithium ions or protons. This might not be true for highly optimized DSC systems. Also, following electron injection, injected electrons undergo rapid thermalisation down to the TiO_2 electron Fermi level in about 200 fs [104, 105], so this advantage might be lost. Another explanation could be that the intersystem crossing time from the singlet to triplet state is very fast (<100 fs) [71] and the ^{3}MLCT state is populated before charge injection from the singlet state is completed. Additionally, it is also possible that electron injection takes place equally efficiently even after relaxation to the ^{3}MLCT state and that there are no other direct relaxation channels from the higher excited ^{1}MLCT state to the ground state.

Effect of distance: The distance between the dye donor, typically the chromophore in Ru dyes, and the semiconductor has been shown to influence electron injection dynamics. Asbury *et al.* have reported a study where n (=0,1,3) CH_2 spacer groups were inserted between the bipyridine and the carboxylate anchoring groups in a ruthenium dye [35, 53]. The increased distance between the chromophore and semiconductor results in poorer electronic coupling with the acceptor states and, as expected, the injection rate is observed to decrease with increasing number of CH_2 spacer groups. This has been confirmed by other studies using different dyes and spacer units [12]. However, this effect is much less prominent when the linker groups are not rigid or have a conjugated orbital structure [12, 16].

In a follow-up study, Benkö *et al.* also showed that in some dye/semiconductor systems, photoexcitation leads to excited electrons being localized on a ligand of the sensitizer which is not directly attached to the semiconductor [76]. Before being injected into the semiconductor CB, they have to be transferred from the non-surface-attached ligand to the attached one; this interligand electron transfer time is in the picosecond time-scale. Intersystem crossing and intramolecular relaxation within the excited state manifold has been shown to be in the 0.1–1 ps time-range, and these processes, therefore, actively compete with the singlet injection process [16, 71, 76].

Effect of environment: Most of the electron injection dynamics reviewed so far have been measured in dye-sensitized semiconductor films in the absence of an electrolyte. While this gives a very useful first-level understanding about the efficacy of the dye-sensitized metal-oxide system, it is equally essential to study electron transfer dynamics in the presence of an electrolyte and other additives, in order to simulate the working conditions inside a complete DSC [51]. Initial studies have led to the conclusion that the presence of the redox electrolyte causes a significant retardation of the electron injection rate, as compared to an inert, aprotic solvent [87, 106]. Durrant *et al.* have reported injection half-times ($t_{50\%}$) as low as 120 ps in

TiO_2/N719 and 3000 ps in TiO_2/Z907 [87].

Haque *et al.* concluded that the change in the electron injection dynamics is because of the additives in the electrolyte which cause a conduction band shift in the semiconductor, as discussed in detail already [80]. Later this was also confirmed in another study conducted by the Durrant group [96], where they conclude that the injection dynamics are independent of the presence of the iodide/triiodide redox couple, but are strongly dependent on the concentration of ions such as *t*BP and Li^+. Bonn *et al.* recently employed terahertz spectroscopy on dye-sensitized nanostructured TiO_2 and SnO_2 films immersed in different media (air, acetonitrile, iodine/iodide redox couple, disulfide/thiolate redox couple, *t*BP and Li^+ additives) [107], and came to a similar conclusion that electron injection time is dependent on the ion concentration in the DSC.

The exact mechanism for this influence is still not very well understood. Abrusci *et al.* recently reported ten-fold improvement in short-circuit current in TiO_2/D102/P3HT SDSC devices with the addition of Li-TFSI salt [108]. D102 is an organic dye with molecular structure shown in Figure 3.1 while P3HT (poly(3-hexylthiophene)) is a well-studied polymer commonly employed as hole-transporter in organic photovoltaics and hybrid DSC devices [109]. They concluded that the presence of Li^+ ions increases the charge transfer nature of the dye excited state. This effect appears to be more significant than the previously discussed shift in the surface potential of TiO_2 due to the presence of ions.

Process 4: Regeneration of oxidized dye

Following electron injection into the semiconductor, the oxidized dye is reduced to its original ground state by an electron donor. This dye regeneration increases the lifetime of the separated charges, and also enables diffusion of the oxidized species to the counter-electrode, completing the device circuit. The most popular and effective reductant used in DSCs is iodide. The reduction of the oxidized dye (S^+) by iodide (I^-) most probably follows the following reaction mechanism [12, 110–112]:

$$\mathrm{S^{+} + I^{-} \longrightarrow (S \bullet\bullet\bullet I)}$$

$$\mathrm{(S \bullet\bullet\bullet I) + I^{-} \longrightarrow (S \bullet\bullet\bullet I_2^{-\,\bullet})}$$

$$\mathrm{(S \bullet\bullet\bullet I_2^{-\,\bullet}) \longrightarrow S + I_2^{-\bullet}}$$

$$\mathrm{2\,I_2^{-\bullet} \longrightarrow I_3^{-} + I^{-}}$$

The first step is a straight-forward one electron transfer between $\mathrm{S^{+}}$ and $\mathrm{I^{-}}$. The oxidation of iodide to free iodine radical ($\mathrm{I^{\bullet}}$) is energetically unfavourable because the redox potential of $\mathrm{I^{\bullet}/I^{-}}$ vs NHE is more positive than the oxidation potential of most dyes, $\mathrm{S^{+}/S}$ [12] (Figure 2.3). The redox potential of the iodine radical bound to the dye ($\mathrm{S \bullet\bullet\bullet I}$) will be less positive and therefore energetically more favourable [51]. Addition of a second iodide helps the complex to dissociate into ground-state dye S and $\mathrm{I_2^{-\bullet}}$. Finally, $\mathrm{I_2^{-\bullet}}$ dissociates forming triiodide and iodide.

Evidence for the intermediate complexes has been found via nanosecond resolution TAS experiments by monitoring the decay of the dye cation absorption, and/or the recovery of dye ground state absorption [68, 111]. For efficient DSC performance, it is essential that the rate of rereduction of dye cations by the redox couple exceeds that of recombination of photoinjected electrons with the oxidized dye [12, 51]. For the most common Ru sensitizer, N3, the half-time for regeneration in the presence of about 0.5 M iodide in the $\mathrm{I^{-}/I^{3-}}$ electrolyte is in the range of 100 ns to 10 μs [94, 113, 114], as shown in Figure 2.5.

The lifetime of the oxidized Ru dye is about 100 sec, as measured by cyclic voltammetry [66]. The interception by the electrolyte is therefore $\sim 10^8$ times faster, and thus the dye can sustain almost 100 million turnovers in continuous solar cell operation without loss of performance. Rapid regeneration of the dye is crucial for delaying the dye from permanent degradation. This depends on various factors, most importantly the electrolyte composition. Lower iodide concentration, and higher electrolyte viscosity result in a retardation of regeneration [51]. Pelet *et al.* found that the nature of cation of the iodide salt strongly influences the regeneration rate [115]; faster regeneration occurs in the presence of ions that adsorb onto the $\mathrm{TiO_2}$ surface such as $\mathrm{Li^{+}}$ and $\mathrm{Mg^{2+}}$, but slower regeneration is observed otherwise, with ions such as TBA$^+$. This was explained by the resulting higher local iodide concentration near the TiO_2 surface when positive charge is adsorbed. The regeneration rate can also be tuned by small modifications in the sensitizer molecule. For example, the addition of bulky alkyl chains to the dye has been found to reduce regeneration rate, due to steric and nonpolar shielding offered to the metal oxidized center [116]. Finally, the relative energetics of the dye oxidized state and the reductant need to be carefully optimized in order to improve regeneration rate [12].

In solid-state DSCs employing spiro-OMeTAD as the HTM, dye regeneration is much faster, in the picosecond–nanosecond time-domain [116–118]. This is indicated with a blue label in Figure 2.5. Hole transport through the HTM occurs via polaron hopping between sites (Appendix A.1) [10, 119], with mobility estimated to be $\sim 10^{-4}\,\mathrm{cm^2V^{-1}s^{-1}}$ in the pristine material [33, 47]. The faster dye regeneration in SDSCs (nano- versus microseconds) suggests that the dye should have a much longer lifetime if it is contacted by an organic HTM [10].

Despite all the advantages of using a redox electrolyte for dye-regeneration and hole-transport in DSCs, it is commonly agreed that the dye regeneration step is the largest source of loss in potential of the device [24, 112]. A certain "overpotential" is necessary to drive this electron transfer step with near-unity efficiency. To illustrate, in the device depicted in Figure 2.3, there is an overpotential of about 0.2–0.3 eV required to oxidize the electrolyte [112]. There is a further drop of $\sim$0.3 eV when $I_2^{-\bullet}$ converts to I^{3-}. If regeneration could occur through a one-step mechanism, this overpotential would be significantly reduced, thus yielding higher V_{OC} and, therefore, higher device efficiency [19].

Process 5: Electron transport through semiconductor

The mesoporous semiconductor electrode is typically composed of nanoparticles sintered together in a randomly interconnected matrix, through which electrons can percolate by hopping from one crystallite to the next. These nanoparticles are electronically undoped, unless slight doping takes place unintentionally during device fabrication. This could happen, for instance, when the semiconductor nanoparticles are sintered in the absence of air, leading to excess oxygen vacancies getting created. For the undoped case, under operating condition at 1 Sun intensity, the electron density in mesoporous TiO_2 in a DSC device is approximately $10^{18}\,cm^{-3}$ [12]. This is much lower than the concentration of cations in the electrolyte, $\sim 3\times 10^{20}\,cm^{-3}$. The nanoparticles thus do not have an inherent internal electric field. Also, electrons injected from the dye molecules are charge-compensated by the ions in the electrolyte. The main driving force for electron transport is, therefore, the gradient in electron concentration. Consequently, electron transport in DSCs occurs by diffusion rather than drift [120, 121].

Since the electrolyte is percolated throughout the nanoparticle matrix, the probability of the mobile electrons in the mesoporous semiconductor film getting captured by the electrolyte remains high until the electrons get successfully transported to the electrode. Efficient charge collection by the external circuit, therefore, requires the time constant for electron transport to the collection electrode to be faster than charge recombination of injected electrons with the redox couple. As discussed in Figure 2.4, it is now a proven fact that there exist subbandgap states in TiO_2 that influence electron transport, even though the exact distribution and location of these trap states is still under debate [10]. This knowledge is critical for a complete understanding of the charge transport mechanism in this nanostructured material. It is thought that the traps involved in electron transport can arise from defects located either in the bulk, at grain boundaries, or at the surface of the nanoparticles. They can also be partly attributed to Coulombic trapping due to local field effects through interaction of electrons with the polar TiO_2 crystal lattice or with cations in the electroyte [10, 12].

There is much experimental and theoretical evidence that supports the hypothesis that electron transfer takes place via a trapping-detrapping mechanism, between trap-states deep in the tail of the DoS and the CB (Figure 2.4), consistent with the multi-trapping model for charge transport [59, 61–63]. Electron transport dynamics are, therefore, strongly dependent on the position of the TiO_2 electron Fermi level; raising the Fermi level toward the conduction-band edge results in increased trap filling and thus, faster electron transport [51].

This is corroborated by the fact that higher incident light intensity results in faster electron transport [12]. Similarly, Boschloo *et al.* reported that electron transport increases at fixed high light intensities as the cell is biased towards short-circuit from open-circuit [122]. While this is true for liquid electrolyte DSCs, Snaith *et al.* observed that, at open-circuit conditions, the effective electron diffusion coefficient in solid-state DSCs levels off or even starts decreasing with increasing light intensity [33]. This is most probably due to the transport increasingly becoming "hole-limited". This emphasizes the need for a complete model for charge tranport, accounting for electronic mechanisms in different types of DSCs, under all working conditions.

Electron transport in the mesoporous semiconductor film is also a strong function of the network geometry. As the film porosity increases, the average coordination number decreases and the number of dead ends (nanoparticles with only one neighbor) increases from less than 1% in a 50% porous film to 31% in a 75% porous film [123]. Consequently, the electron travel path becomes increasingly tortuous, leading to slower electron transport rates [10, 12]. The percolation threshold was found at the critical porosity of 76%. In addition, replacing the randomly connected network of a nanoparticle-based film with a network fabricated from oriented nanotube or nanowire structures offers the advantage of directed electron transfer with higher electron mobilities [124–126]. However, surprisingly, no significant improvement in electron mobility has been observed [127, 128]. In the case of ZnO nanotubes, this has been explained on the basis of scattering from grain boundaries and due to disorder induced localizations [127]. In polycrystalline TiO_2 nanotubes, however, THz pump-probe measurements show that the poor electron mobility is due to the existence of exciton-like trap states, most probably due to the presence of Ti^{3+} states created during the nanotube synthesis [129] (Appendix A.2). In the following chapters, THz spectroscopy has been employed in conjuction with photovoltaic-related measurement techniques to understand the reason for the significantly different electron transport characteristics exhibited by DSCs fabricated using TiO_2, ZnO and SnO_2 nanostructured films.

Process 6,7: Recombination loss mechanisms

While moving through the sintered nanoparticle matrix towards the anode, electrons are always within a few nanometers distance of the semiconductor-dye-electrolyte interface, with a high probability of recombining with either the oxidized dye molecules or acceptors in the electrolyte. Recombination with the dye cations competes with the dye regeneration process, which takes place over the microsecond time-scale, as shown in Figure 2.5. This recombination rate has been studied extensively using nanosecond laser spectroscopy, and is observed to follow a multiexponential rate law, proceeding over a microsecond to millisecond time-scale [12, 94, 130].

This recombination rate is strongly influenced by the electron density in the semiconductor, and thus the incident light intensity, accelerating by almost an order of magnitude between short-circuit and open-circuit conditions [51]. Additionally, it decreases exponentially as the spatial separation of the dye cation from the nanoparticle surface increases [51]. The dependence of the recombination kinetics on the thermodynamic driving force, shown in Figure 2.3 to be about 1.5 eV for this reaction, is still not very clear and the various relevant experimental findings have been nicely summarized in a recent review from the Hagfeldt group [12].

Recombination of electrons in the semiconductor with acceptors in the electrolyte is typically studied by measuring transient response under short-circuit and open-circuit conditions. One of these methods, small perturbation transient photovoltage decay, has been described in detail in Section 3.3. In such experiments, it is assumed that the measured recombination rate is due to recombination of electrons with acceptors in the electrolyte, because dye regeneration is assumed to be very rapid in completely working DSCs. The recombination lifetime is usually referred to as the electron lifetime in literature. Recombination can occur both at the nanoparticle-electrolyte interface and at any part of the conducting substrate (typically fluorine-doped tin-oxide, FTO) in contact with the electrolyte. The latter route can be supressed by depositing a compact hole-blocking layer of the metal-oxide over the FTO, done using spray-pyrolysis in all experiments reported in this thesis.

DSCs with iodide/triiodide electrolyte exhibit very long electron lifetimes, in the milliseconds to second time-range, depicted in Figure 2.5 [10, 12, 51, 131]. This is an extremely desirable characteristic for a DSC. It is difficult to generalize the reaction order for the recombination reaction because of several reasons. In case of DSC devices exemplified by Figure 2.3, a wide distribution of reaction rates can be attributed to the randomly distributed trap states in TiO_2 and the two-step dye regeneration mechanism due to the iodide/triiodide redox couple [12]. Recombination kinetics may be dominated by the electron trapping-detrapping mechanism in the TiO_2. The choice of sensitizer is also a critical factor because the adsorption of dye can cause a shift in the TiO_2 CB edge. O'Regan *et al.* have also shown that some organic dyes assist in faster reduction of I_3^- at the TiO_2 surface by providing a binding site for iodine near the nanoparticle surface [132]. As before, recombination rate increases with electron concentration in the semiconductor, due to trap-filling.

In case of solid-state DSCs with spiro-OMeTAD, the recombination rate is estimated to be much faster, in the microsecond to millisecond time-range, as indicated with a blue label in Figure 2.5 [33, 119]. Most probably this is because it is a one-electron process [10].

Process 8: Transport of redox mediator to counter-electrode

Counter-electrodes for DSCs with I^-/I^{3-} electrolytes are typically prepared by depositing a thin catalytic film of platinum on a conducting glass substrate. Fabrication recipes such as the one detailed in Section 3.1.5 yields electrodes with nanoscale platinum clusters with film resistance as low as $1\,\Omega\mathrm{cm}^2$, thus enabling high performance DSCs with respectable long-term stability [133]. Transport of the redox mediator is mainly driven by diffusion [12]. This transport gives rise to a diffusion impedance which acts as a series resistance in the solar cell. It depends on the diffusion coefficient, concentration of redox mediator, and distance between the electrodes, and can be about 0.7–$2\,\Omega\mathrm{cm}^2$ in a well-optimized system [12].

When high mediator concentrations are used, charge transport can also occur in an alternate way, through formation and cleavage of chemical bonds:

$$I_3^- + I^- \longrightarrow I^- \bullet\bullet\bullet I_2 \bullet\bullet\bullet I^- \longrightarrow I^- + I_3^-$$

This is especially significant in case of viscous electrolytes such as ionic liquids with low diffusion coefficients. At the counter-electrode in standard DSCs, triiodide is reduced to iodide in the presence of Pt in a rapid one-electron reduction reaction [12]:

$$I_3^- + 2\,e^- \longrightarrow 3\,I^-$$

In solid-state DSCs with spiro-OMeTAD hole-transporter, charge transport occurs through hole-hopping (details in Appendix A.1). A very high resistance of the order of $\sim 100\,\Omega\text{cm}^2$ has been reported in SDSCs recently [119], which could possibly be a reason for the observed poor performance of SDSCs.

2.4 Optical Pump Terahertz Probe Spectroscopy

The terahertz (THz) region is the part of the electromagnetic spectrum with frequencies between the microwave and far-infrared regions. It covers the region from about 0.1 to 20 THz, equivalent to 15 to 3000 μm in wavelength. 1 THz is equivalent to 300 μm wavelength, 33.33 cm^{-1} wavenumber, or 4 meV photon energy. With photon energies in the meV range, THz pulses interact strongly with systems with characteristic lifetimes in the picosecond range and energetic transitions in the meV range. This is true for physical phenomena such as low-energy excitations and carrier dynamics in electronic materials, and vibrational, rotational and torsional modes in condensed matter. Some examples of such systems include bound electrical charges, free charge plasmas, excitons, exciplexes, phonons, polarons and plasmons in crystalline solids, weakly bonded molecular crystals, relaxational dynamics in aqueous liquids, hydrated biological matter etc [134–141] (Appendix A).

In addition, there are a number of practical applications of terahertz spectroscopy in the consumer market. Most of these applications exploit the long wavelength range in the terahertz region, giving it a ‘see-through’ property through commonly used materials such as textiles, packaging materials, construction materials etc. Many items of interest, such as moisture, narcotics, explosives, pharmaceutical materials, etc. have a distinct 'signature' in the terahertz spectral region, making them easy to detect. The technique is, therefore, implemented in applications such as body scanners at airport security checks, quality control in food industry, pharmaceutical industry (monitoring tablet coating thickness, for instance), art conservation etc [136, 137, 142, 143].

In this thesis, the main focus is on understanding early-time charge dynamics in dye-sensitized mesoporous semiconductor films used in DSCs. Time-resolved terahertz spectroscopy is a useful technique to this end because charge carrier scattering events in semiconductors, either doped or photoexcited, tend to be on time scales of tens to hundreds of femtoseconds. This results in distinct variations in the real and imaginary components of the complex conductivity in the THz region of the spectrum. In the following sections, the concept behind time-resolved terahertz spectroscopy is introduced, along with the main advantages of using this technique as compared to other pump-probe spectroscopic techniques. Details of the experimental set-up and data-analysis procedure are described in Chapter 3.

2.4.1 Time-resolved optical pump-probe spectroscopy

Over the past few years, optical pump-probe spectroscopy techniques have become a critical tool for understanding early-time charge dynamics in a wide variety of materials. A typical set-up is sketched in Figure 2.6. An ultrafast laser beam is split into two parts, for use as pump and probe beams. Since all the energy is concentrated in a very short time-period, ultrafast pulses tend to have extremely high peak intensities. Photoexciting the sample with an ultrafast pulse can, therefore, induce a linear or non-linear change in the optical properties of the material. This could include interband transitions, ionization, induced polarizations, lattice vibrations etc. The temporal resolution of such techniques is a function of the optical pulse duration. In addition, it also depends on the accuracy of the optical delay line and on the nature of the optical change induced in the sample.

The relative time delay between the pump and probe pulses is systematically varied so

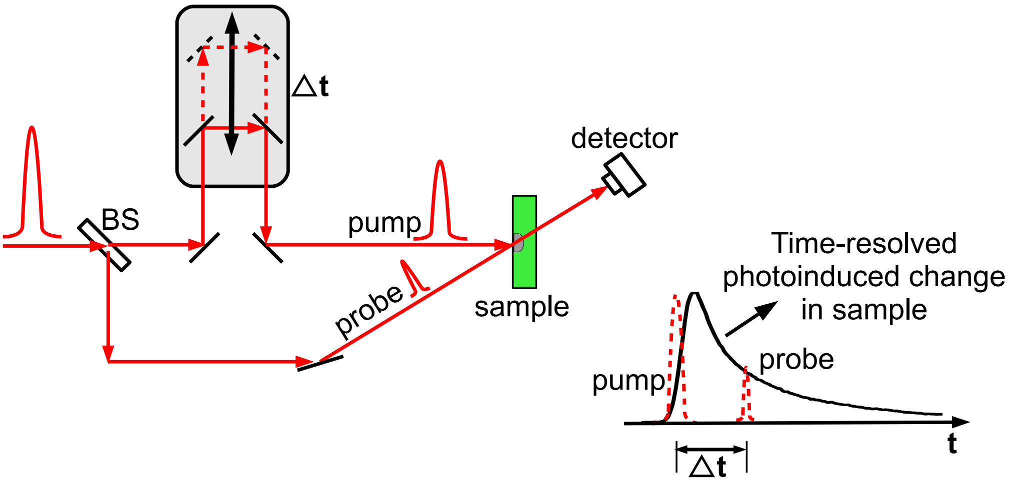

Figure 2.6: Typical set-up of a time-resolved optical pump-probe set-up. BS: beam-splitter, short black lines at 45°: mirrors, Δt: relative delay between pump and probe pulses.

that the photoinduced change can be mapped out as a function of time, as depicted in Figure 2.6. This time delay is adjusted by making the probe pulse path length longer with respect to the pump pulse by using a translation stage. The photoinduced changes in the sample are then analysed by measuring the probe transmission, reflection or scattering.

2.4.2 THz time-domain spectroscopy

THz time-domain spectroscopy (THz-TDS) is used for measuring optical properties in a material under steady-state conditions. Typically the experimental setup is based on an unamplified femtosecond laser. A simplified sketch is shown in Figure 2.7. The femtosecond beam is split into two parts; the larger fraction is used as a pump pulse to generate a THz pulse using a terahertz source such as a photoconductive antenna [143] or by employing optical rectification (Section 3.5.3). The sample is probed with a single cycle of terahertz radiation. The smaller part of the femtosecond beam is used to detect the transmitted THz electric field by using a THz detector such as a photoconductive antenna [143] or electro-optic sampling (Section 3.5.4) to measure the transmitted THz pulse.

It is important to note that these measurements are not *time-resolved*, rather steady-state

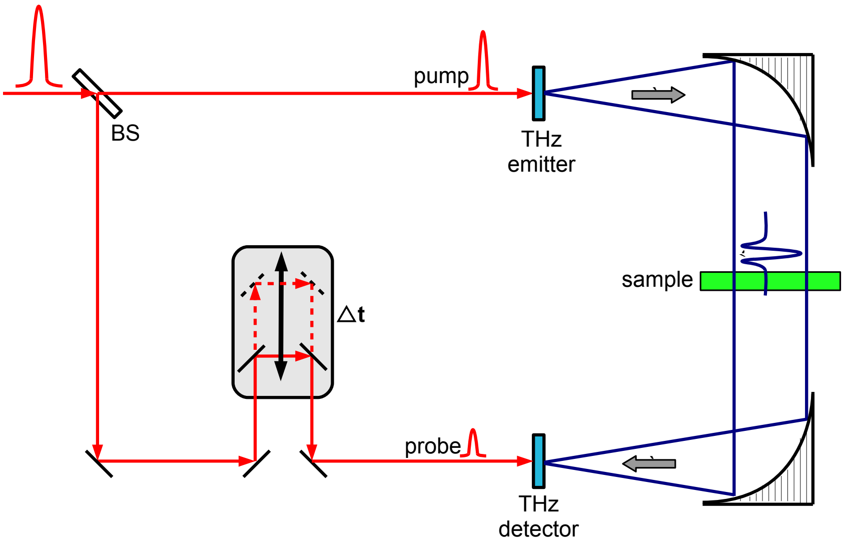

Figure 2.7: Schematic of a typical set-up for THz TDS, showing the generation and detection of THz pulses using femtosecond optical pulses.

measurements. The sample is not photoexcited with an optical pulse in this experiment. The technique is called time-domain spectroscopy (TDS) because the data is measured in time-domain and then fourier-transformed to obtain spectral information. Since this technique measures both the amplitude and phase of the transmitted THz pulse, and not just the intensity, the Fourier analysis of the transmitted or reflected THz pulse can yield not only the absorption but also the dispersion in the material. More detailed discussion is given in Sections 3.6.1 and 3.6.2.

2.4.3 Time-resolved optic-pump THz-probe (OPTP) spectroscopy

All THz measurements reported in this thesis have been measured using time-resolved OPTP spectroscopy. The experiment is based on an amplified femtosecond laser setup, described in detail in Section 3.5.1. The set-up is quite similar to that shown in Figure 2.7, except that there is an additional femtosecond laser beam for photoexciting the sample under study. As shown in the schematic in Figure 2.8, the sample is first photoexcited with a femtosecond pulse at a chosen wavelength to induce the desired optoelectronic change in the material.

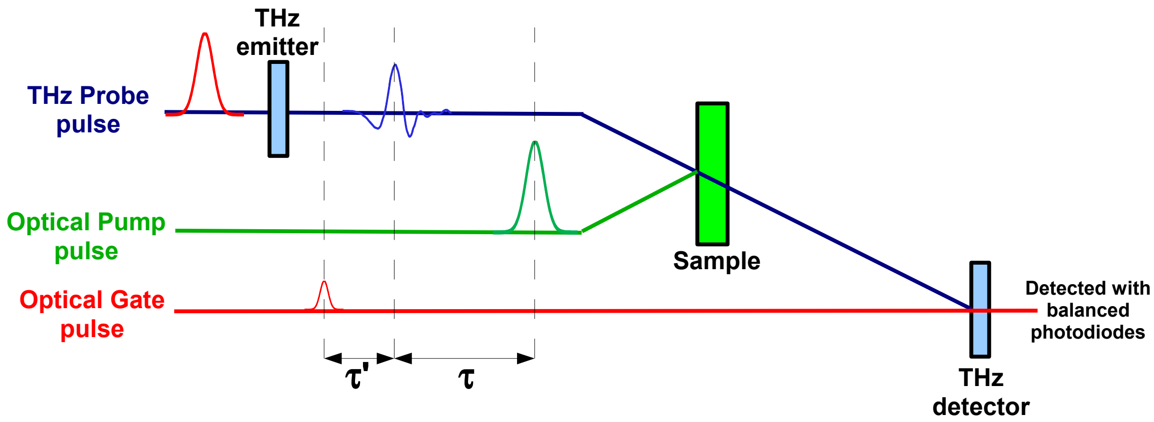

Figure 2.8: A schematic showing the delay scheme in a typical OPTP experimental set-up. The optical gate pulse is kept fixed and the terahertz probe and optical pump pulses are delayed from this by a time-interval τ' and $\tau' + \tau$ respectively. By fixing τ'=0 and varying τ, a 1-D pump scan is conducted. Alternatively, fixing τ and varying τ' yields the 1-D probe scan, described in detail in Section 3.5.5. A detailed sketch of the OPTP experimental set-up is given in Figure 3.17.

The photoexcited sample is then probed with a single cycle THz pulse after time τ. The transmitted terahertz waveform is then mapped via electro-optic sampling by probing with a femtosecond gate pulse at a time-lag τ' after the THz pulse.

2.4.4 Advantages of THz spectroscopy

THz-TDS (time-domain spectroscopy) is quite different from most other pump-probe techniques in that the transient electric field itself is measured, not simply its intensity. Fourier transforming the transient electric field enables direct determination of both the amplitude and the phase of each of the spectral components that make up the pulse, and, thus, the frequency-dependent complex-valued conductivity of the sample. This is directly related to the index of refraction and absorption coefficient of the sample. Therefore, the complex-valued permittivity of the sample can be directly measured using OPTP without having to carry out a mathematical Kramers-Kronig analysis [144]. THz-TDS adds critical information to what can be obtained from DC conductivity measurements such as Hall effect. DC measurements are dominated by the slowest conduction step as charges are moved over relatively large distances. Conversely, high-frequency THz radiation can be used to probe intrinsic material properties that are less affected by macroscopic disorder or sparse defects. Knowledge of a materials frequency dependent conductivity is important for its use in electronic devices.

Time-resolved OPTP spectroscopy is a non-contact electrical probe capable of measuring photoconductivity with a temporal resolution of less than 200 fs, and up to a nanosecond time-scale. Being an all-optical technique, OPTP can probe charge dynamics in nanostructured materials (mesoporous films, nanowires, carbon nanotubes etc.) while avoiding any issues arising from the possible existence of non-Ohmic contacts. A fundamental strength of OPTP is that the energy range of the terahertz probe is significantly below the band-gap of typical semiconductors, allowing it to act as a true probe of the photoexcited system. Many quasi-particles do, however, absorb in the terahertz frequency range, and the spectral variation in THz absorption is characteristic of the system being probed. OPTP measurements can therefore provide a unique THz 'spectral signature' characteristic of free charge carriers, trapped charges, excitons, exciplexes, surface plasmons, polarons, etc [134–141] (details in Appendix A).

Charge transfer mechanisms in DSC systems have been studied and reported by various research groups in great detail using ultrafast pump-probe techniques with probe frequencies in different regions of the spectrum ranging from far-IR to visible, such as transient absorption spectroscopy (TAS). While the information so obtained is extremely useful, the data-analysis requires an in-depth knowledge of the various ultrafast chemical processes taking place in the system which lead to changes in specific regions of the transmitted visible-IR spectrum [72]. OPTP spectroscopy has a significant advantage that it allows the direct observation of time-dependent charge injection in the dye/semiconductor system, without the need for complex analysis of multiple overlapping signals from TAS. Time resolved microwave conductivity (TRMC) measurements offer a similar capability, but can only achieve nanosecond temporal resolution [145].

2.5 Summary

The concept of dye-sensitized solar cells has been introduced in this chapter. The advantages and short-comings of this technology have been described, along with a detailed review of the various charge transfer mechanisms that take place in DSCs under working conditions. The latter part of the chapter gives a brief introduction to the OPTP spectroscopy technique, which has been employed to study electron mobility and electron injection dynamics in nanostructured semiconductor films sensitized with dyes, as reported in the following chapters.

Chapter 3

Experimental Techniques

In the work reported in this thesis, early-time electron injection and transport dynamics in dye-sensitized nanostructured metal-oxide films have been measured using a combination of photovoltaic characterisation techniques and time-resolved terahertz spectroscopy. The first half of this chapter describes the fabrication protocol for both liquid electrolyte and solid-state DSCs along with a brief description of some typical photovoltaic-related measurement techniques and their experimental set-ups. While THz spectroscopy is slowly becoming well-established among spectroscopists, both the experimental details and the data-analysis can be challenging. With this motivation, the latter half of the chapter is devoted to an in-depth explanation of the technique, experimental set-up and the relevant data-analysis.

3.1 DSC device fabrication

3.1.1 Materials

Colloidal TiO_2 paste

For the work shown in Chapter 4, TiO_2 colloidal paste was prepared by Pascal Comte in the Grätzel lab at EPFL using a method similar to that presented by Barbe *et al.* [146, 147]. Briefly, titanium iso-propoxide and acetic acid were hydrolyzed with water and peptized with nitric acid. The colloidal particles were then grown hydrothermally. The as-grown particles were redispersed by sonication and concentrated with a rotary evaporator. Ethyl cellulose and terpineol were then added to the centrifuged and washed material to obtain a homogeneous paste. This process resulted in $\sim$20 nm anatase TiO_2 nanoparticles.

The TiO_2 related work shown in Chapter 5 was performed on TiO_2 paste purchased from a commercial source, Dyesol (18NR-T), and thinned with ethanol in a volume to mass ratio of 3:1 ml g^{-1} ethanol:TiO_2. The paste was then gently sonicated with an ultrasonic horn. The particle diameter in this case was also about ~20 nm. Both pastes are composed of 100% anatase TiO_2, confirmed by XRD measurements [1].

Colloidal SnO_2 paste

Measurements discussed in Chapters 5 and 6 were measured on two separate batches of SnO_2 paste prepared using the same recipe [148]. One batch was prepared by Pascal Comte in Michael Grätzel's group at EPFL while the second batch was prepared by Pablo Docampo in Dr. Snaith's lab at Oxford. In both cases, SnO_2 particles were synthesized via hydrolysis of $SnCl_4$ in water. HNO_3 was used to control the pH of the dispersion. After autoclaving at 230°C and ultrasonification, the particles were concentrated in a rotary evaporator. All water in the mixture was then replaced by anhydrous ethanol using a combination of centrifugation and sonification. Finally, the synthesized SnO_2 nanoparticles were mixed with ethyl cellulose and terpineol to create the paste [147]. The final SnO_2 nanoparticles were about 10 nm wide and 20 nm long [148].

Colloidal ZnO paste

ZnO paste was prepared by Pablo Docampo in Dr. Snaith's lab using ZnO nanopowder purchased from Sigma Aldrich (544906, <100 nm size). The powder was ground with ethanol, dissolved in terpineol and ethyl-cellulose and sonicated to achieve a well-dispersed paste [147]. The nanoparticle concentration was adjusted depending on the method of film-preparation – spin-coating, doctorblading or screen-printing.

3.1.2 Dye-sensitization

Ruthenium polypyridyl dyes have been the best-performing dyes since the early days of DSC research and have been already introduced in Section 2.3 [12, 15, 16]. Most of the work shown

---

[1] information provided by Dr. Henry Snaith

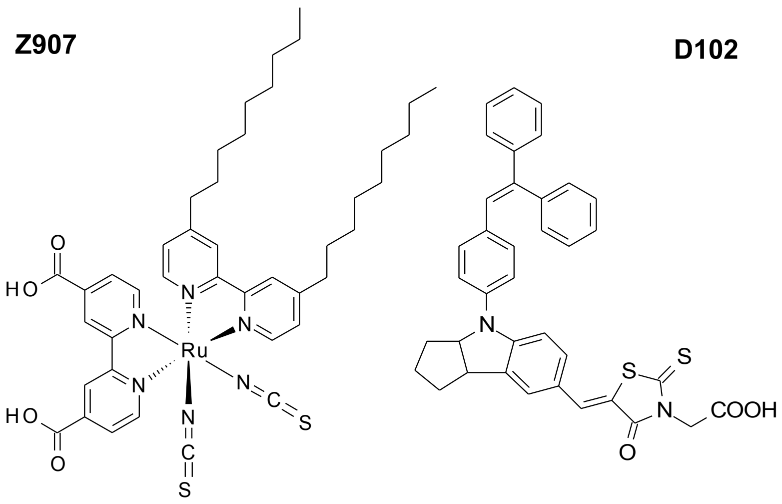

Figure 3.1: Molecular structures of Z907 and D102 dyes used in this thesis.

in this thesis has been done with Z907 dye, a well-known amphiphilic polypyridyl ruthenium complex, NaRu(4-carboxylic acid-4'-carboxylate)(4,4'-dinonyl-2,2'-bipyridine)$(NCS)_2$, with two of the carboxylate groups in the N3 dye replaced by nonyl chains [27]. The molecular structure is shown in Figure 3.1. This dye contains two carboxylate groups to anchor to the TiO_2 surface while the hydrophobic alkyl chains act as a spacer providing an insulating barrier between the hole conductor and electron-transporting semiconductor. They also help form a more compact monolayer of the dye on the TiO_2 surface. As described in Section 2.3.2, this arrangement facilitates faster charge injection and slower charge carrier recombination [65, 149]. Z907 has been successfully employed in polymer gel-electrolyte cells and shows a remarkably long-term thermal stability [130, 150].

Some DSC results described in this thesis have also been measured on solid-state DSCs with an organic indoline-based dye, D102 (structure shown in Figure 3.1). Being a metal-free organic dye, it is more environmentally friendly and can be more easily synthesized from widely available materials [12, 44, 45, 151]. Also, organic dyes have a much higher absorption coefficient compared to ruthenium dyes such as N3, N719 or Z907 [44, 148]. For instance, the absorption coefficient of D102 is 55,800 $\mathrm{L mol^{-1} cm^{1}}$ at 491 nm, which is about 4 times stronger than the most popular ruthenium dye, N3 (13,900 $\mathrm{L mol^{-1} cm^{-1}}$) [44]. Therefore, as much as 90% incident light can be absorbed within 2–3 micron thick D102-sensitized TiO_2 films. This is immensely beneficial because thinner semiconductor films imply lower series resistance in the device. Organic dyes, therefore, have a huge potential for application in flexible and/or solid-state DSCs which typically have very thin metal-oxide films.

3.1.3 Redox electrolyte

All liquid electrolyte devices discussed in this thesis were prepared using 'robust' electrolyte in a nonvolatile solvent, composed of 0.8 M PMII, 0.15 M iodine, 0.1 M GuNCS, and 0.5 M NMBI in 3-methoxy propionitrile (MPN) [28].

3.1.4 Organic hole transporter

All SDSCs in this thesis were fabricated using spiro-OMeTAD (2,2',7,7'-tetrakis(N,N-di-methoxypheny-amine)-9,9'-spirobifluorene) as hole-transporter [32, 152] (Figure 2.2). The material properties are reviewed in detail in Section 2.2.4. Tert-butylpyridine (*t*BP) and bis(trifluoromethyl-sulfonyl)amine lithium salt ($Li[CF_3SO_2]_2N$) (Li-TFSI) (dissolved separately in acetonitrile) were used as additives in the hole-transporter for improved device performance. The presence of mobile ions in the HTM improves the hole mobility and also enables higher current densities in the device as hole-transport is no longer operating under the space-charge-limited regime [149, 153]. Also, the presence of Li^+ ions in SDSCs induces a charge screening effect which leads to a retardation in electron recombination rate [48, 118, 153].

3.1.5 Liquid electrolyte DSC assembly

Fluorine-doped tin-oxide (FTO) glass sheets (15 $\Omega/\square$, Pilkington) were thoroughly washed with soap (2% Hellmanex® in water), de-ionized (DI) water, acetone, isopropanol (IPA) and finally treated under an oxygen plasma for 10 minutes to remove the last traces of organic residues. The FTO sheets were subsequently coated with a compact layer of the appropriate hole-blocking metal-oxide layer using aerosol spray pyrolysis deposition, using air as the carrier gas, while keeping the FTO substrates at 450°C. For SnO_2 devices, butyltin trichloride (95%, Sigma Aldrich) at 250 mM concentration in anhydrous ethanol was used; for TiO_2, titanium diisopropoxide bis(acetylacetonate) (Sigma Aldrich, 75% by weight in isopropanol) at 250 mM concentration in anhydrous ethanol was used; and for ZnO, zinc acetate dihydrate (99.999%, Sigma Aldrich) at 100 mM concentration in anhydrous methanol was used. The films were maintained at 450°C for 30 minutes, resulting in ∼100 nm thick compact films.

The ZnO, TiO_2 and SnO_2 nanoparticle pastes were subsequently applied on the substrates, either by doctor-blading or screen printing. In case of screen-printing, after applying the paste, the substrate was solvent annealed with ethanol for 1 to 5 minutes to ensure that the films were smooth across the substrate. With each application technique, thick films were prepared by applying multiple coats of the metal oxide paste. Between consecutive coats, the films were heated at 140°C for 5 minutes to evaporate the solvent, in order to prevent the previous coat from getting washed away by the solvent in the next coat.

The films were then slowly sintered in air with a slow ramp up to 500°C over 3 hours, resulting in porous mesoporous films. Porosity of TiO_2 films typically prepared via this route was measured with a BET (Brunauer, Emmett and Teller) setup to be ∼60% [2] [10]. After cooling down, the FTO sheets were cut into smaller $1.4\times1.4\,\text{cm}^2$ pieces.

Before dye-sensitization, the substrates were reheated up to 130°C to remove any moisture from the films, cooled down to 70°C, and then immersed into the dye solution for sensitization. The dye solution comprised of either 0.3 mM Z907 or 0.2 mM D102, both in acetonitrile/tert-butanol (1:1 vol%) solvent. D102 sensitization required only 1 hour in the dark at room temperature while sufficient Z907 adsorption in the mesoporous metal oxide films took about 14 hours. After dyeing, the films were briefly rinsed in acetonitrile to

---

[2] Measurement done by Michael Grätzel's group at EPFL

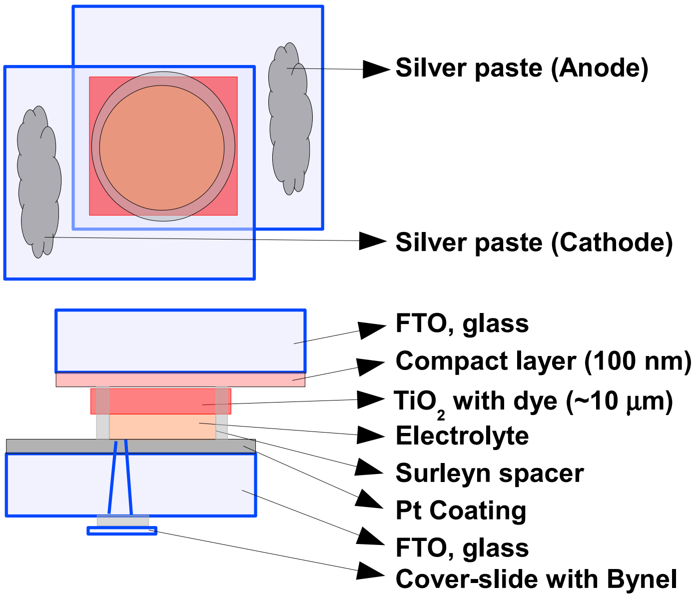

Figure 3.2: Top-view and side-view of the sandwich-type assembly used for making liquid-electrolyte DSCs. The FTO glass pieces are $\sim 1.4\times 1.4\times 0.3\,\mathrm{cm}^3$ in dimension.

remove any dye molecules not physically adsorbed on the semiconductor surface and then dried in air for a few seconds. Complete devices were assembled on these dyed electrodes immediately to prevent the dye from getting oxidized.

The counter-electrode was prepared by drilling a small hole in a separate $1.4\times 1.4\,\mathrm{cm}^2$ FTO piece with a sand drill. After thoroughly cleaning the FTO with the standard procedure (soap, DI water, acetone, IPA), it was platinized by coating the FTO side with a drop of 0.05 M hexachloroplatinic acid (H_2PtCl_6) in anhydrous isopropanol and heating at 400°C for 15 minutes. This FTO glass was then assembled in a sandwich type configuration with the dye-sensitized metal oxide coated FTO glass, using a hotmelt 25 μm thick polymer spacer (Surleyn, Dupont) at 200°C to seal the working and counter electrodes together. A drop of robust electrolyte [28] was injected into the interelectrode space from the predrilled hole in the counter-electrode via vacuum back-filling. Finally, the hole was sealed with a Bynel sheet (Dupont) and a thin glass cover slide by locally heating the hole to 450°C with a soldering iron. A cartoon of a typical device structure is drawn in Figure 3.2.

3.1.6 Solid-state DSC assembly

FTO glass sheets (15 Ω/□, Pilkington) were first etched with ZnO powder and HCl (2 M) to obtain the desired electrode pattern. The sheets were then thoroughly cleaned with soap, DI water, acetone and IPA, followed by oxygen plasma treatment. As in the case of liquid electrolyte DSCs, a compact layer was spray-coated on the FTO at 450°C. The compact layer prevents direct contact between the hole conductor and the metal oxide layer, which would short-circuit the cell. During the deposition of the compact layer, the electrodes were masked so that the metal oxide only covered the FTO and not the etched glass. The metal oxide nanoparticle paste was then coated via doctor-blading and slowly sintered in air at 500°C as described earlier. After cooling down, the FTO sheets were cut down to smaller pieces ($1.4\times1.4\,\mathrm{cm}^2$).

It has been shown by several research groups that treating the TiO_2 mesoporous film with $TiCl_4$ results in significantly improved device performance [63, 78, 146, 154, 155]. The underlying reason for this change is not well-understood and has been explored in the work discussed in Chapter 4. For preparing the samples studied in Section 4.3.3, some of the TiO_2 films were treated with $TiCl_4$ by soaking them in a 20 mM aqueous solution of $TiCl_4$ for 4 hours at room temperature in the dark [78, 154]. After rinsing with DI water and drying in air, the films were then resintered to 500°C for 45 min. Similarly, some of the SnO_2 and ZnO films were treated with MgO for coating the nanoparticles with a conformal layer of the high band-gap material. This was achieved by immersing them in 20 mM magnesium acetate in a boiling ethanol bath maintained at 100°C for 1 minute. The films were then resintered to 500°C in air for 45 min.

Dye-sensitization with Z907 or D102 was carried out as described in the previous section. Immediately after dye-sensitization, the hole transporter infiltration step was carried out. The hole-transporter solution was composed of 180 mg/ml spiro-OMeTAD in chlorobenzene. Once fully dissolved, *t*BP was added with a volume to mass ratio of 1:26 $\mu\mathrm{l\,mg^{-1}}$ *t*BP:spiro-OMeTAD. Li-TFSI was pre-dissolved in acetonitrile at 170 $\mathrm{mg\,ml^{-1}}$ and added to the hole-transporter solution at 1:12 $\mu\mathrm{l\,mg^{-1}}$ of Li-TFSI solution:spiro-OMeTAD [50]. About 25 μL

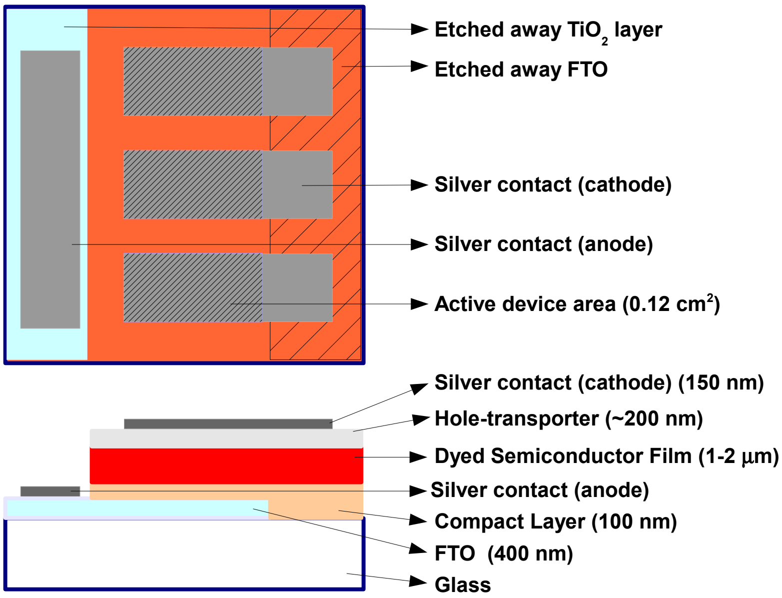

Figure 3.3: Top-view and side-view of a solid-state DSC fabricated on the FTO side of the substrate. Each ∼$1.4\times1.4\times0.3\,\mathrm{cm}^3$ FTO glass substrate had 3 active pixels on it, with areas about $0.12\mathrm{cm}^2$ each.

of the solution was deposited on the substrate and left to wet the film for 40 seconds before spin-coating at 2000 rpm for 25 seconds in air. The film was left overnight to dry in an air atmosphere before evaporating 150 nm thick silver electrodes on top under high vacuum (10^{-6} mbar) to complete the devices. Before evaporating the metal, the HTM and metal oxide layers were manually etched away from one side of the substrate (while keeping the underlying FTO intact) using a wooden toothpick. This is shown in Figure 3.3, and was done to ensure a good bottom contact.

3.2 Steady-state photovoltaic characterisation

3.2.1 Current-voltage characteristics

Electrically, the ideal solar cell is equivalent to a current generator in parallel with an asymmetric non-linear resistive element, i.e., a diode [156]. This is illustrated in Figure 3.4. On

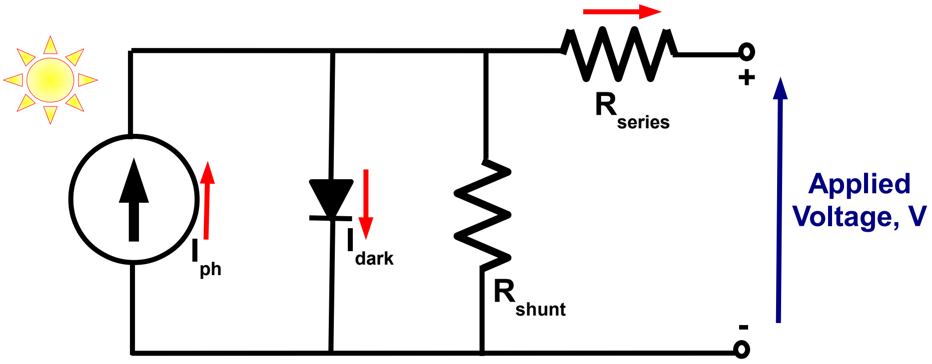

Figure 3.4: Equivalent circuit of a solar cell.

illumination, the ideal cell generates current proportional to the incident light intensity. This photocurrent is divided between the bias-dependent diode resistance and the applied load, in a ratio depending on the total photogenerated current and the load resistance. Since the voltage across the diode is equal to that measured across the load, the diode provides the device photovoltage. In a real photovoltaic device, power is dissipated through different resistances inherent in the device architecture and through leakage currents in the device. These effects are electrically equivalent to two parasitic resistances, R_{series} in series and R_{shunt} in parallel with the cell, as shown schematically in the figure.

The series resistance arises due to resistance of the cell materials and contacts to current flow, and includes contact resistance at interfaces, bulk resistance, FTO sheet resistance, etc. The shunt resistance arises from leakage of current through the cell, around the edges of the device and between contacts of different polarity. Microscopically, this occurs because of charge recombination within the device. In an ideal efficient cell, $R_{shunt} \rightarrow \infty$ and $R_{series} \rightarrow 0$.

Current-voltage (JV) measurements are carried out on a photovoltaic device by exposing it to illumination and applying a bias voltage V in the direction shown in Figure 3.4 (blue arrow). Figure 3.5 illustrates typical JV characteristics measured with and without illumination. Under illumination, the current flows through the load in the opposite direction (red arrows in circuit diagram) than the injected current (blue arrow). At zero-bias voltage, the

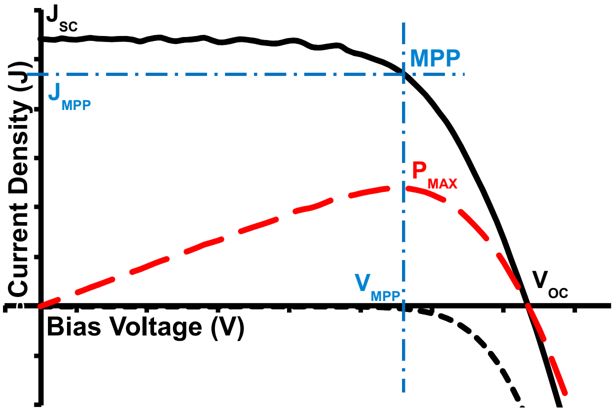

Figure 3.5: JV curve of a typical DSC under illumination (black solid curve) and in the dark (black dotted curve). The power density curve (J×V) is shown with a red dashed curve. Also indicated are the short-circuit current density (J_{SC}), open-circuit voltage (V_{OC}), maximum power point (MPP), current and voltage at MPP (J_{MPP}, V_{MPP}).

maximum generated photocurrent flows under short-circuit conditions (J_{SC}). At open-circuit voltage (V_{OC}) condition, the photogenerated current is balanced to zero. Between V=0 and $V=V_{OC}$, the device generates power and it is, therefore, the desired operating regime of the device. In the absence of illumination, no current flow is observed as the voltage is steadily increased, until the contacts start injecting heavily at forward bias for voltages higher than V_{OC}.

The device power density, $P = JV$, reaches a maximum at the cell's operating point, or 'maximum power point' (MPP). This occurs at some voltage V_{MPP} with a corresponding current density J_{MPP}, as seen in Figure 3.5. Device efficiency, η, is the power density delivered at the device operating point as a fraction of the incident solar power density, P_s,

$$\eta = \frac{P_{MAX}}{P_s} \tag{3.1}$$

$$= \frac{J_{MPP}.V_{MPP}}{P_s} \tag{3.2}$$

$$= \frac{FF.J_{SC}.V_{OC}}{P_s} \tag{3.3}$$

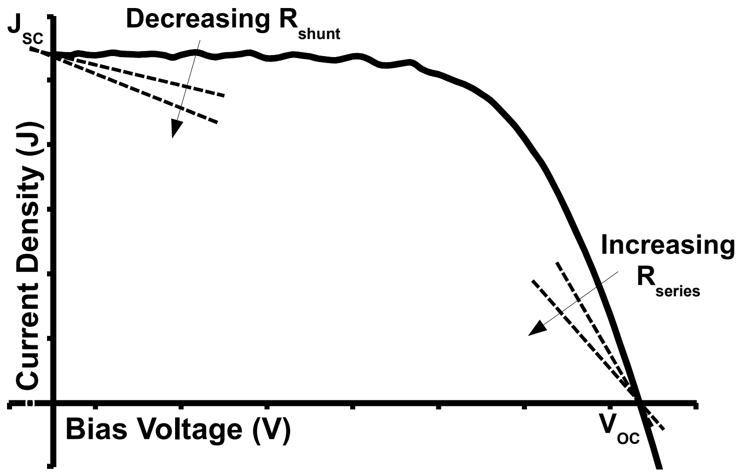

Figure 3.6: Effect of series and shunt resistances (R_{series} and R_{shunt} respectively) on the solar-cell JV characteristics.

where FF is the device fill factor calculated as:

$$FF = \frac{J_{MPP}.V_{MPP}}{J_{SC}.V_{OC}} \tag{3.4}$$

and describes the 'squareness' of the JV curve. In addition to J_{SC}, V_{OC}, FF and η, the JV curve can also indicate the amount of parasitic shunt and series resistances in the device, mentioned earlier in Figure 3.4. These values can be estimated from the slope of the JV curve as shown in Figure 3.6.

All I-V measurements reported in this thesis have been carried out under standard test conditions (STC) of 25°C temperature and an irradiance of $1000\,W/m^2$ with an air mass 1.5 global (AM1.5G) spectrum. According to ASTM (American Society for Testing and Materials) standards, this corresponds to the irradiance and spectrum of sunlight incident on a clear day upon a sun-facing 37°-tilted surface with the sun at an angle of 41.81° above the horizon. The illumination source was an Abet Technologies Class AAB solar simulator with an AM1.5 global filter. The intensity was calibrated with an NREL calibrated silicon reference cell incorporating a KG5 Schott filter in order to minimize the solar spectral mismatch factor when measuring the DSCs, which are typically only photoactive in the visible to near-infrared region. The current and voltage measurements were taken with a Keithely 2400 sourcemeter interfaced to a PC.

For all photovoltaic measurements (both steady-state and transient photocurrent photovoltage experiments), the devices were masked with optical masks such that the effective area of the device was aproximately $0.12\,\mathrm{cm}^2$. The surface of the metallic masks facing the incident light and the probes (typically, alligator clips) were covered with black non-reflecting insulating tape, to prevent any light-scattering related artefacts or short-circuiting [157]. This was especially important in the case of $\mathrm{SnO_2}$-based liquid-electrolyte DSCs, since edge effects were observed to be quite significant. In these devices, Snaith *et al.* have shown that relying on the overlap between the FTO and the metal electrode to define the active area underestimates the active area of the solar cell by ∼25% [148]. In case of solid-state devices, separate measurements were carried out for each of the three pixels for some basic statistical error analysis (Figure 3.3).

3.2.2 IPCE, APCE

The spectral response is determined by measuring the monochromatic incident photon-to-current conversion efficiency, IPCE, of the working devices. Also known as the external quantum efficiency (EQE), IPCE is defined as the number of electrons flowing through the external circuit under short circuit conditions per incident photon at a given wavelength.

$$\mathrm{IPCE}(\lambda) = \frac{\mathrm{n_{electron}}(\lambda)}{\mathrm{n_{photons}}(\lambda)} \tag{3.5}$$

$$= \frac{\mathrm{J_{SC}}(\lambda)\mathrm{hc}}{\mathrm{P_{in}}(\lambda)\mathrm{e}\lambda} \tag{3.6}$$

Here, $\mathrm{J_{SC}}$ is the measured current density in $\mathrm{A/m^2}$, $\mathrm{P_{in}}$ is the input monochromatic power in $\mathrm{W/m^2}$, and λ is the wavelength of irradiation in nanometers. IPCE is typically measured under short-circuit conditions. The standard spectral response measurement is conducted by passing monochromatic light through the device which is mechanically chopped using an optical chopper. A white-light bias at 1 Sun (1000 W/m^2) can be used so that the solar cell is working under true operational conditions, resulting in a background DC signal. The chopped probe beam generates an AC signal on top of the DC signal, which is measured using a lock-in amplifier. This is, therefore, called the AC method. Since DSCs have much slower response time compared to conventional silicon photovoltaics, a very low chopping frequency (5–150 Hz) should be used [158]. This is even more critical in the absence of a white-light bias since the device response becomes even slower. Alternately, the DC method is used which involves exposing the device to continuous irradiation with monochromatic light and measuring the photoresponse without a lock-in. The photocurrent generated in this case may be 2–3 orders of magnitude lower than that in full sunlight, so the results are only valid if the photocurrent scales linearly with light intensity, which is usually the case for DSCs [12, 158].

For the IPCE measurements reported in this thesis, monochromatic light was generated by focusing a 300 W Xenon lamp (Oriel) through a monochromator (Princeton Instruments Acton SP2150i). The spectrally resolved output light intensity was calibrated with a calibrated silicon reference diode incorporating a KG5 Schott filter in order to approximately match the absorption profile of the dyes. The intensity of the monochromatic beam was set at $\sim$1 mWcm^{-2} (about 0.01 Sun). The electrical response of the solar cells and reference diode were recorded under short-circuit conditions with a Keithley 2400 interfaced to a PC. A typical IPCE spectrum measured on a liquid-electrolyte DSC is shown in Figure 3.7.

In order to directly compare the IPCE measurement with the JV measurement carried out under 1 Sun intensity, the spectral response was corrected by integrating the measured IPCE spectrum over the AM1.5G solar spectrum at 100 mWcm^{-2}. The resulting integrated current value is denoted as the spectral mismatch factor, $\mathrm{J_{SC,SpectralMismatch}}$,

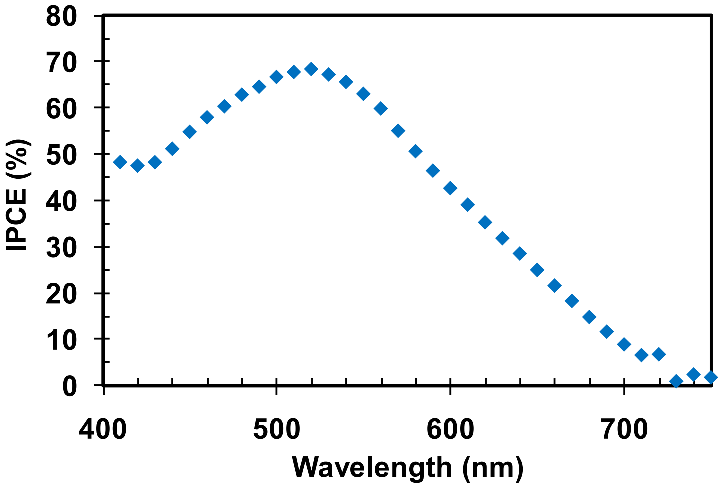

Figure 3.7: Typical IPCE measured on a SnO_2-based liquid-electrolyte DSC sensitized with Z907 dye.

$$\mathrm{J}_{\mathrm{SC,SpectralMismatch}} = \left(\int_{400}^{750} \mathrm{EQE} \times \mathrm{Flux}_{\mathrm{AM1.5G}}\, \mathrm{d}\lambda\right) \times \mathrm{e}, \mathrm{C/s/m^2} \tag{3.7}$$

$$= \frac{(\int_{400}^{750} \mathrm{EQE} \times \mathrm{Flux}_{\mathrm{AM1.5G}}\, \mathrm{d}\lambda) \times \mathrm{e}}{10}, \mathrm{mA/cm^2} \tag{3.8}$$

where $\mathrm{Flux}_{\mathrm{AM1.5G}}$ is a function of spectral power, $\mathrm{Power}_{\mathrm{AM1.5G}}$ ($\mathrm{W/m^2/nm}$), as

$$\mathrm{Flux}_{\mathrm{AM1.5G}} = \frac{\mathrm{Power}_{\mathrm{AM1.5G}}}{\mathrm{hc}/\lambda}, \mathrm{/s/m^2/nm} \tag{3.9}$$

The corrected peak spectral response, $\mathrm{IPCE}_{\mathrm{peak,AM1.5G}}$, can therefore be calculated from the measured peak spectral response measured under 0.01 Sun, $\mathrm{IPCE}_{\mathrm{peak}}$, as:

$$\mathrm{IPCE}_{\mathrm{peak,AM1.5G}} = \frac{\mathrm{IPCE}_{\mathrm{peak}} \times \mathrm{J}_{\mathrm{SC,JVmeasurement}}}{\mathrm{J}_{\mathrm{SC,SpectralMismatch}}} \tag{3.10}$$

In this manner, it is ensured that the corrected integrated short-circuit photocurrent is in close agreement with the maximum photocurrent value measured in the JV curves under standard conditions. This correction has been performed on the IPCE data discussed in Chapter 5.

The absorbed photon-to-electron conversion efficiency (APCE) obtained by dividing IPCE(λ) by the absorption spectrum is extremely useful because it separates the optical (light harvesting) and electrical (charge injection and collection) components of the IPCE. In state-of-the-art DSC devices, APCE can be 100% even though IPCE is approximately 85% [148], indicating that charge injection and collection are optimized for the device even though it is not fully absorbing across the visible spectrum.

3.3 Time-resolved transient photovoltaic characterisation

Small perturbation transient photovoltage and photocurrent decay measurements were carried out on both liquid-electrolyte and solid-state DSCs in order to measure electron transport and recombination dynamics in the complete working devices. The set-up is similar to that of O'Regan *et al.* [159] and as described elsewhere [50, 160]. A white light bias of $100\,\mathrm{mW/cm^2}$ was generated from an array of diodes (Lumiled Model LXHL-NWE8 whitestar) with red-light pulsed diodes (LXHL-ND98 redstar, $200\,\mu$s square pulse width, 100 ns rise and fall time) as the perturbation source, controlled by a fast solid-state switch. The perturbation light source was kept low enough to ensure that the voltage or current decay kinetics were monoexponential. This enabled the charge recombination or transport rate constants to be obtained directly from the exponential decay rate.

For the *transient short-circuit voltage decay measurements*, a Keithley 2400 sourcemeter was connected in series with the solar cell and in parallel with a 1 GHz Agilent oscilloscope which was set on the high impedance ($1\,\mathrm{M\Omega}$) port. The Keithley sourced current through the solar cell kept under bias illumination, such that the voltage was at 0 V (i.e. at short-circuit condition). No extra current was allowed to flow through the device following the light pulse. The extra charges generated due to the perturbation pulse cannot therefore leave the device and can only recombine over time. The voltage decay trace therefore yields the recombination rate, k_{rec}. The decay usually happens on a relatively long timescale of tens to hundreds of milliseconds because the charge density in the film at short circuit is very low in comparison to that under open-circuit conditions.

For the *transient short-circuit current decay measurements*, the voltage bias was fixed at 0 V (i.e. at short-circuit) during the perturbation. The photocurrent dynamics were recorded directly through the low impedance port (50 Ω) of the oscilloscope. In this case, following perturbation, charge transport occurs simultaneously with recombination within the cell. The measured decay rate, $\mathrm{k}_{\mathrm{signal}}$, therefore, is a combination of $\mathrm{k}_{\mathrm{rec}}$ and the transport rate, $\mathrm{k}_{\mathrm{trans}}$, as $\mathrm{k}_{\mathrm{signal}} = \mathrm{k}_{\mathrm{trans}} + \mathrm{k}_{\mathrm{rec}}$.

The charge collection efficiency can then be estimated from these measurements as

$$\eta_{\mathrm{coll}} = \frac{\mathrm{k}_{\mathrm{trans}}}{\mathrm{k}_{\mathrm{trans}} + \mathrm{k}_{\mathrm{rec}}} = \frac{\mathrm{k}_{\mathrm{trans}}}{\mathrm{k}_{\mathrm{signal}}} \tag{3.11}$$

These measurements can be further used to estimate the electron diffusion coefficient and diffusion length in the mesoporous semiconductor matrix, as described in detail in Chapter 4 Section 4.3.1.

This experimental set-up can also be used to estimate the “chemical capacitance” of the dye-sensitized nanocrystalline solar cell. The textbook definition of capacitance refers to an electrostatic geometric capacitance, determined by the electric field between two metal plates with equal amounts of opposite charges, where the excess charges are localised near the respective plates. However, as explained in detail by Bisquert in Ref. 161, the capacitance of a nanocomposite heterogeneous DSC device originates from several different factors. As stated by Bisquert, “a change in electrochemical potential causes, both an accommodation of the field by excess charges and a variation in the Fermi level position with respect to the conduction band in the plates”. This change in Fermi level occurs due to variation in both 1) free electron density in the conduction band (CB) and 2) trapped electrons in the localized levels within the bandgap. The contribution of the density of states, DoS, to the chemical capacitance is given by [161]

$$C_{\mathrm{DOS}} = e^2 \frac{dN}{dE} \tag{3.12}$$

where e is the absolute elementary charge and dN/dE is the total DoS of the mesoscopic capacitor plates [162]. In a DSC such as the one described in Figure 2.1, these are the TiO_2 mesoporous network connected to the transparent conducting oxide (TCO) electrode, and the redox electrolyte connected to the Pt electrode, respectively. In case of macroscopic metal plate capacitors, dN/dE is very large and the corresponding *change* in C_{DOS} component is negligible in comparison to the geometric electrostatic capacitance.

The amount of charge accumulated in the device (ΔQ) due to a known voltage perturbation (ΔV) can be used to calculate the chemical capacitance (C) of the device. ΔQ is estimated by integrating the area under the measured current decay curve at short-circuit condition. ΔV is extracted from the peak of the voltage perturbation under open-circuit conditions under the same bias light intensity. The capacitance is then calculated as

$$C = \frac{\Delta \mathrm{Q}}{\Delta \mathrm{V}} \tag{3.13}$$

The correlation between capacitance and DoS is discussed in further detail in Chapter 6 Section 6.3.4 where this experimental technique has been employed to estimate the change in DoS in SnO_2 due to exposure to light.

Finally, charge extraction measurements can be obtained by exposing the device to a constant white background light at short circuit conditions while the photocurrent response is measured with an oscilloscope. Once the device response is stabilized, the white background light is completely switched off and the subsequent photocurrent decay is measured. The charge density is then extracted by integrating the area under the curve for a known active area volume.

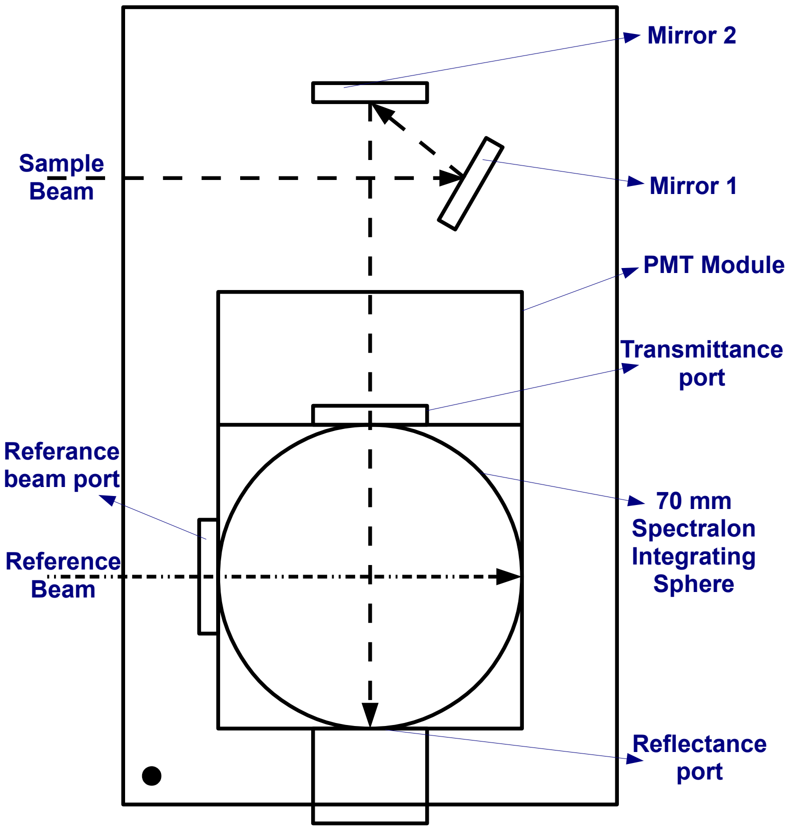

Figure 3.8: Set-up of the Varian Cary 300 spectrophotometer with the Labsphere integrating sphere. The sample and reference beam-paths are indicated with dashed arrows.

3.4 UV-vis-NIR absorption

The total light absorbed within the photoactive layer was measured using a commercially available Varian Cary 300 spectrophotometer equipped with a Labsphere integrating sphere. The set-up is shown in Figure 3.8. The inside of the sphere is coated with a material with very high diffuse reflectivity (>99% from 400 to 1500 nm). A photomultiplier tube (PMT) within the sphere captures almost the entire amount of light incident on the inner walls of the sphere, and can be used to accurately measure the total, diffuse or specular tranmittance and reflectance of the sample, and consequently, the total absorbance in the sample.

All measurements were carried out using the double-beam mode where the beam from the instrument's illumination source is split into two beams; the sample and the reference beams. The integrating sphere, and thus the PMT, is alternately illuminated by the two beams. At any wavelength, the instrument records the ratio of the signal produced by the detector when the sphere is illuminated by the sample beam to that when the sphere is illuminated by the reference beam. This helps in normalizing the responsivity of the PMT detector. A baseline correction is carried out at the start of each set of sample measurements, in order to compensate for any imbalance in the energy of the sample and reference beams, and to account for any changes in sphere efficiency due to the introduction of the sample holder into the system etc.

Transmittance measurement

For all transmittance measurements, the reflectance port R shown in Figure 3.9 was blocked with a plug made with spectralon, a material patented by Labsphere with >99% diffuse reflectivity in the wavelength region of interest. This prevented any light from escaping from the exit port. The only loss was due to any light escaping back through the transmittance port T. Before making any sample measurements, the 100% baseline was first measured with the empty sample-holder at port T and port R blocked with spectralon. The sample was then mounted in the holder at port T, taking care to position the desired face of the sample towards the probe light. In case of devices, the FTO side was always positioned facing the light, while in case of the terahertz spectroscopy samples, the dye-sensitized semiconductor surface was facing the light. This is done to simulate the actual experimental conditions.

As mentioned above, while measuring the transmittance baseline, while most of the incident light is successfully detected by the PMT detector, some of it escapes from the integrating sphere by back-scattering through the entrance port. Once the sample is placed at the entrance port for measurement, reflections from its back surface cause the amount of light escaping through the entrance port to get altered. This results in a slight overestimation of the sample transmittance measurement. This is a function of the reflectance of the back surface of the sample (R_{back}), area of entrance port (A_{entrance}) and total internal surface area of the integrating sphere (A_{sphere}). As a first order estimate, the corrected transmittance can

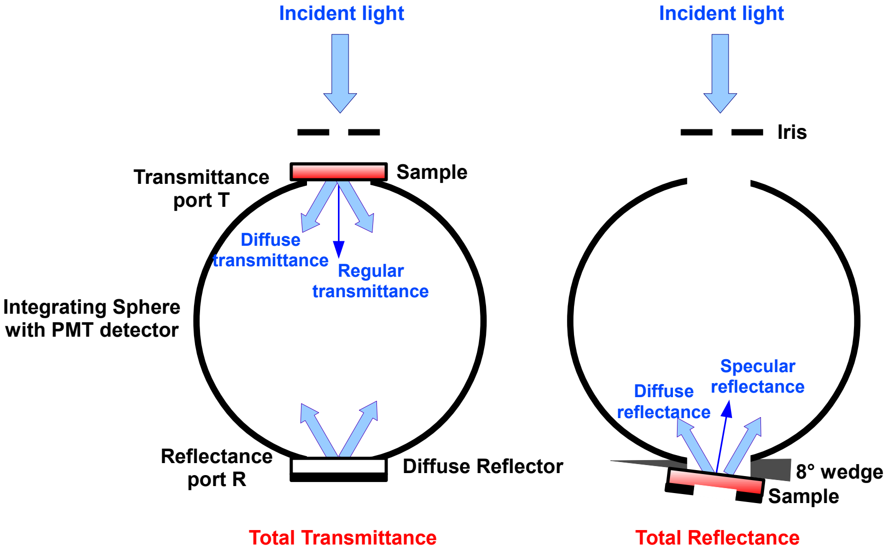

Figure 3.9: Setup used for measuring total transmittance and total reflectance using the Varian Cary 300 spectrophotometer with the Labsphere integrating sphere. The incident light from the monochromator is irised to make it fits within the sample area without scattering from the edges.

be estimated as [148]:

$$T_{corrected} = T_{measured} \times (1 - R_{back} \times \frac{A_{entrance}}{A_{sphere}}) \tag{3.14}$$

The reflectivity of glass is about 10% at 550 nm, the wavelength of interest in most of the experiments reported in this thesis. For a 13 mm diameter sample holder used with the 70 mm internal diameter integrating sphere, the correction factor comes to about $0.1 \times (\pi \times (13/2)^2)/(\pi \times (70/2)^2) \simeq 0.0034$. The correction factor is therefore only about 0.34% and has been ignored in the following discussions.

Reflectance measurements

All reflectance measurements were done with the transmittance port T open and the sample mounted in the sample holder held securely at the reflectance port on a 8° wedge, as shown in Figure 3.9. This ensured that most of the reflected light, especially the specular component, was successfully captured by the integrating sphere and directed towards the PMT detector, rather than being ejected back out of the entrance port. As before, a baseline correction was performed before making any sample measurements, with the entrance port empty and the reflectance port blocked with the high reflectivity spectralon plug. For all sample measurements, the sample was mounted in the sample holder such that only reflected light stays in the sphere while transmitted light is allowed to escape from the sphere.

Since the reflection from the samples is actually more specular in nature than diffuse, the reflectance data had to be calibrated with respect to reflectance spectra measured from an optically thick metallic reference. This reference was made by freshly evaporating silver on a glass slide for each batch of measurements. From the raw reflectance data shown in Figure 3.10, it is obvious that the measured reflectance of 125% at 550 nm is erroneous and needs to be rescaled. For the silver calibration data, reflectance data has been used from literature which has been measured using spectroscopic ellipsometry on a similar optically thick silver film [148, 163], and has been shown in the figure for comparison. A wavelength dependent correction factor is then calculated by dividing the true reflectance values (blue line) with the measured values (black line), and shown with the red line in the figure. All reflectance data reported in Chapters 5 and 6 was measured with respect to a baseline measured with the spectralon standard, and then corrected by multiplying with this correction factor.

Absorbance measurements

The most relevant parameter for this thesis is the total absorbance within the sample, and it was calculated from the measured transmittance (T) and reflectance (R) values as

$$A = 1 - T - R \tag{3.15}$$

Figure 3.11 shows the absorbance measured in z-cut quartz (used as substrate in all terahertz spectroscopy experiments) and FTO (15 Ω/□, Pilkington) respectively. As expected, T, R and A are completely featureless in case of quartz with less than 1% absorbance over

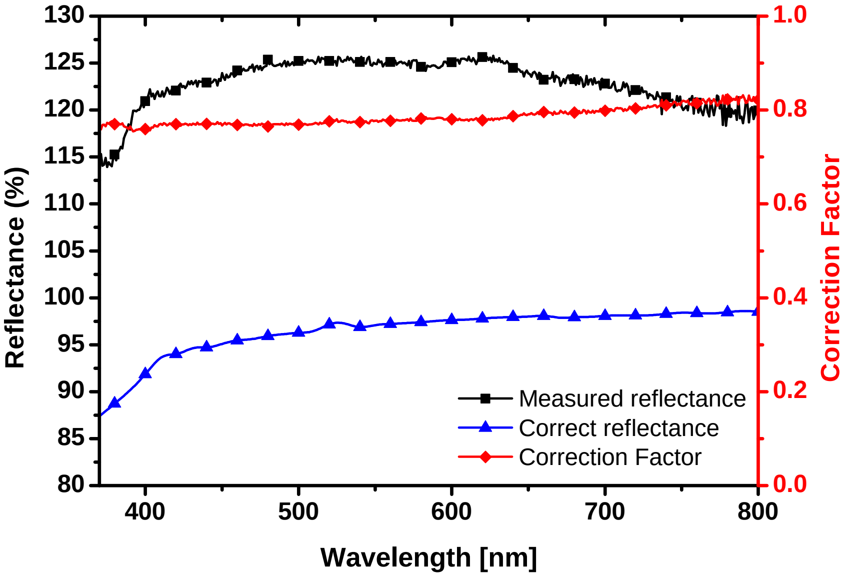

Figure 3.10: As-measured reflectance data on an optically thick silver film on a cover-slide (black squares), correct silver reflectance data from literature [163] (blue triangles), and calculated 'correction factor' (red diamonds). The correction factor measurement and calculation is repeated with a freshly evaporated silver film for each separate batch of UV-Vis measurements.

the visible spectrum. In case of FTO, absorbance varies between 3 and 15% with a minimum at ~550 nm. The reflectance is ~12%, resulting in transmission ~84% at 550 nm. All the steady-state optical absorbance data shown in this thesis has been measured on dye-sensitized semiconductor films on z-cut quartz.

3.5 Optical-pump terahertz-probe spectroscopy

All the terahertz spectroscopy data shown in this thesis has been measured using the set-up sketched in Figure 3.17. A few of the more complex elements are described in detail first, before describing the overall experimental set-up in Section 3.5.5.

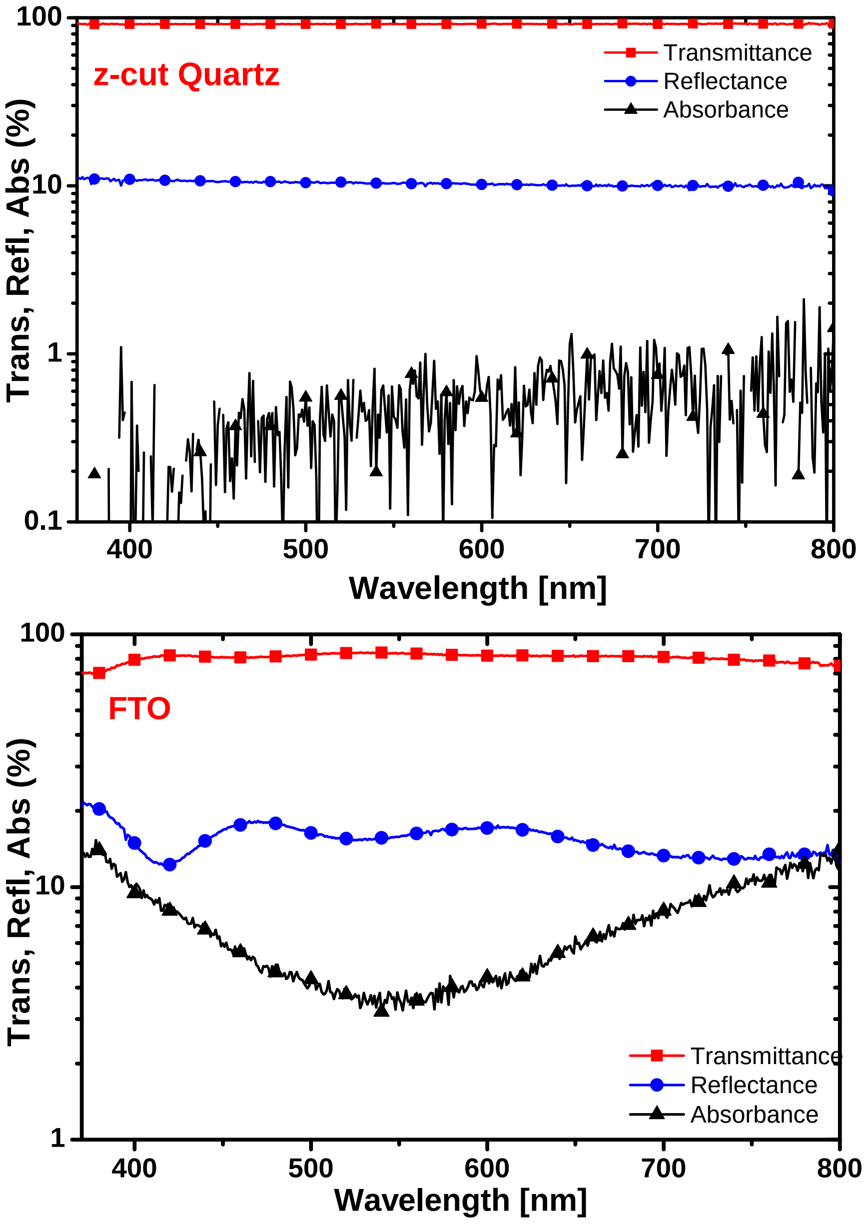

Figure 3.11: Transmittance, reflectance and absorbance in z-cut quartz and FTO glass. In both cases, the reflectance has been corrected using the correction factor shown in Figure 3.10, and absorbance is calculated using Eqn 3.15.

3.5.1 Amplified femtosecond pulses

Ultrashort pulses with centre wavelength 800 nm, ∼35 fs pulse duration, 12 nJ pulse energy at 80 MHz repetition rate are generated using a Spectra-Physics *Tsunami* mode-locked Ti:sapphire laser system. In order to successfully photoexcite the semiconductor films studied in this thesis using OPTP spectroscopy, femtosecond pulses with much higher peak power are required. For this purpose, the Tsunami pulse-train is used to seed a Spectra Physics regenerative amplifier system (*Spitfire Pro*) which has a Ti:sapphire crystal pumped by an intracavity-doubled Q-switched diode-pumped Nd:YLF laser system (neodymium-doped lithium yttrium fluoride) (Spectra-Physics *Empower*). The Empower generates 527 nm pulses at 1 KHz repetition rate with an average power of 7 W. The amount of energy that can be extracted from the Ti:sapphire crystal is limited due to non-linear effects (self-focusing inside crystal) and the damage threshold of the material. This problem increases with increasing pulse energy and decreasing pulse duration, and can be avoided by employing a technique called chirped pulse amplification (CPA). The pulse is first temporally stretched before amplification and then recompressed to the original pulse duration after amplification. One way of stretching the pulse is illustrated in Figure 3.12 where a linear postive chirp (blue lagging behind red) is applied to the 40 fs pulse using a pair of diffraction gratings. The compressor is similar but reversed.

The stretcher and compressor have been implemented in the Spitfire by using a combination of a grating and a retroreflector instead of two diffraction gratings, thus simplifying alignment and maintenance, as shown in Figure 3.13 [164]. Typically, the seed pulse may be stretched up to a nanosecond in duration. These stretched pulses are picked up for amplification from the 80 MHz pulse-train by switching the input Pockels cell. This is controlled by the timing delay generator (TDG) unit synchronized with the Tsunami mode-locking and Empower Q-switching units. When the Pockels cell is switched off, it is transparent to both vertically and horizontally polarized light. When it is switched on, combined with the $\lambda/4$ waveplate behind it, it rotates the beam polarization by 90°. The selected pulse is passed through the gain medium which is pumped with the high energy (∼7 mJ) nanosecond Q-

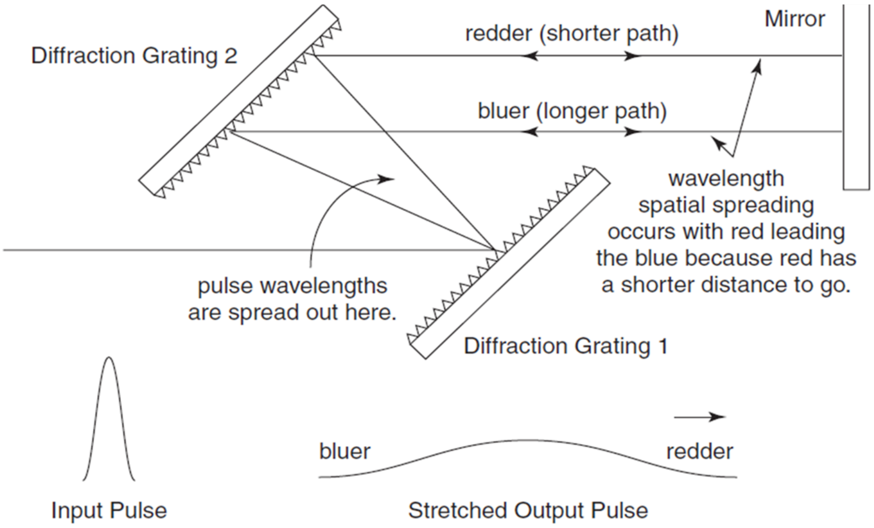

Figure 3.12: Principle of pulse stretching used for 'chirped pulse amplification' in the Spitfire regenerative amplifier. The incident 'seed' pulse is temporally stretched by using a pair of diffraction gratings, inducing a linear chirp in the pulse, with the high frequency (bluer) part of the pulse delayed with respect to the low frequency (redder) part. The pulse compressor implements the same principle but in reverse order. Taken from Ref 164.

switched Empower pulses at 1 KHz repetition rate. A single pass through the Ti:sapphire rod increases the pulse energy by about 3–4 times, without significantly depleting the population inversion in the medium. The pulse power can, therefore, be increased from 12 nJ to 1 mJ by using a regenerative amplification technique. As long as the selected pulse remains horizontally polarized, it remains confined in the cavity. Whenever a pulse arrives at the Ti:sapphire crystal as vertically polarized, it is reflected off the crystal surface because of its Brewster angle, and is hence not amplified. After about 7 round-trips of the cavity, maximum possible amplification is achieved and the population inversion in the gain medium is exhausted. The output Pockels cell is now switched on and the pulse is allowed to escape from the cavity, into the compressor. The pulse is recompressed to the fourier-transform limited pulse duration using a diffraction grating. Through regenerative amplification, therefore, energy amplification greater than 6 orders of magnitude is achieved, resulting in a 1 KHz repetition rate $\sim$40 fs duration pulse-train with pulse energy 1 mJ and centre wavelength 805 nm.

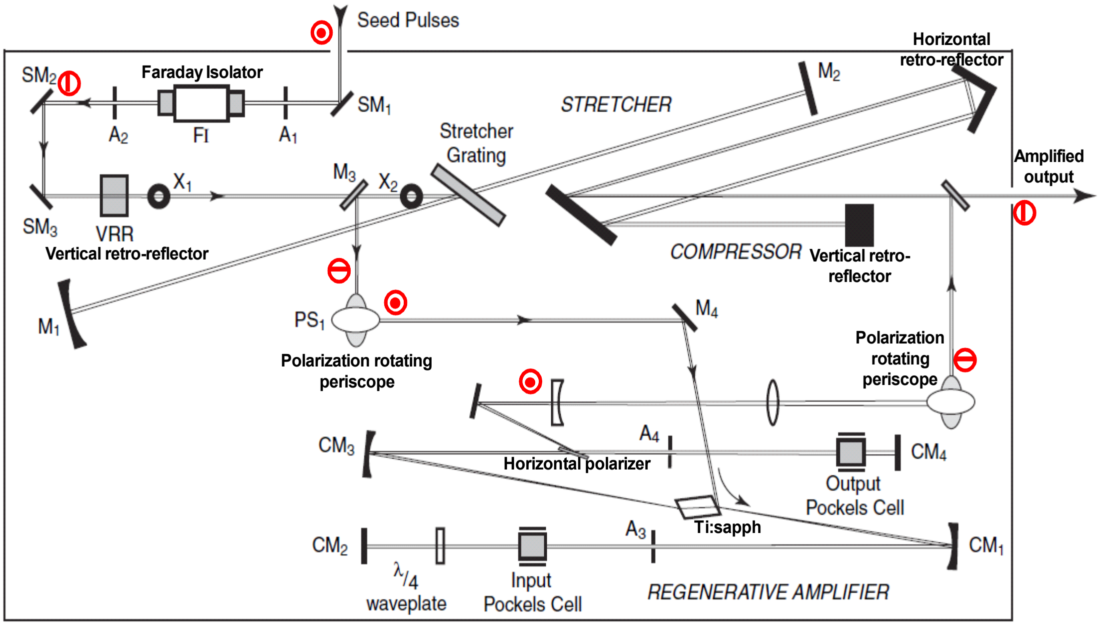

Figure 3.13: Layout of the Spectra-Physics *Spitfire-Pro* Ti:sapphire regenerative amplifier system. The 'seed' pulse from the Tsunami system is first temporally stretched in the *stretcher* (top-centre), then amplified by enabling multiple passes through a Ti:sapphire gain medium in the *regenerative amplifier* (bottom-right), and finally compressed to the transform-limited pulse-duration in the *compressor* (top-right). The beam polarization is carefully controlled in order to amplify selected pulses from the 80 MHz Tsunami seed pulse-train to a 1 mJ 1 KHz repetition rate output. The red symobls show the beam polarization state at different points in the beam-path: ⊙ indicates vertical polarization and ⊖ indicates horizontal polarization. Adapted from figure in Ref 164.

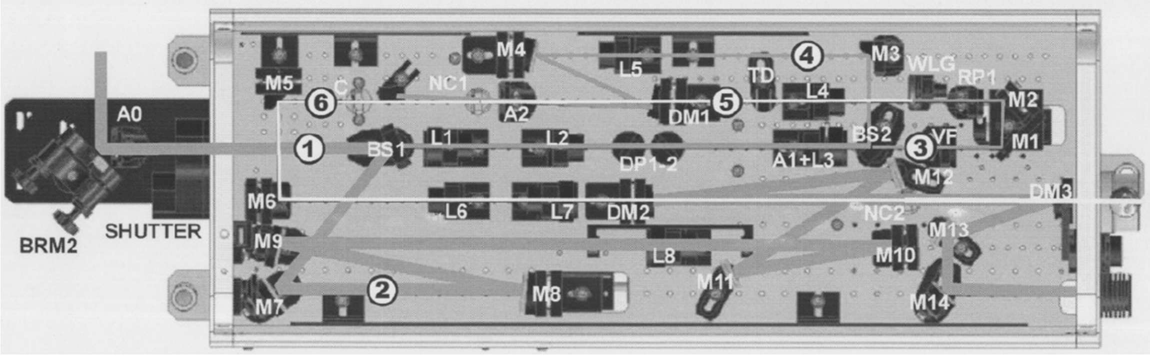

Figure 3.14: Layout of the OPA system (Spectra-Physics *TOPAS*) used for generating optical pump pulses at wavelengths ranging between 475–700 nm. Both the optical components and beam-paths are shown. Numbers have been assigned to specific parts of the beam-path which have been described in detail in the main-text. Taken from Ref 165.

3.5.2 OPA

Amplified femtosecond duration pulses from the Spitfire are used to pump an optical parametric amplifier (OPA) (Spectra Physics *TOPAS-C*) (traveling-wave optical parametric amplifier of white-light continuum) which is capable of generating 240 nm to 20000 nm wavelength pulses while maintaining the pulse duration at ∼40 fs. The full layout of the OPA is shown in Figure 3.14 [165]. The 800 nm ∼500 μJ pump beam entering through the input beam shutter after mirror BRM2 (1) is split into two parts at beam-splitter BS1. The smaller fraction (30–50 μJ) is again split at BS2 and the smaller of the two parts (3) (1–3 μJ) is used to produce white light continuum (WLC) in a sapphire plate WLG. The WLC beam (5) and the larger fraction (4) are timed and overlapped non-collinearly inside the nonlinear crystal NC1 where parametric amplification takes place. The signal beam (6) is directed to the amplification stage while the residual beams and idler beams are blocked with a beam blocker.

The power amplifier stage is pumped with the bulk of the input pump beam (2). The signal beam (6) is collinearly and temporally overlapped with the pump beam (2) at the second nonlinear crystal NC2, resulting in well-collimated signal and idler beams, both of which are allowed to exit from the TOPAS output. The two beams are passed through a combination of frequency mixers outside the TOPAS unit (not shown in Figure 3.14) in order to generate and isolate the desired wavelength. Wavelength tuning is achieved by adjusting the angles of the nonlinear crystals, the delay between the two beams at both the crystals, and the choice of filters after the TOPAS output. This is synchronously done via a software provided with the TOPAS equipment. To achieve wavelengths longer than 2000 nm, the crystal set inside the TOPAS needs to be changed. All work in the thesis has been done using wavelengths between 475 and 700 nm.

3.5.3 THz generation - optical rectification

THz pulses are generated from high energy femtosecond pulses through optical rectification in $< 110 >$ ZnTe [136, 143, 166]. As described by Schmuttenmaer *et al.*, optical rectification is the difference frequency mixing analog of second harmonic generation [135]. When intense light interacts with a non-linear medium, wave-mixing between two frequencies, ω_1 and ω_2, results in sum-frequency generation, $\omega_1 + \omega_2$, and difference frequency generation, ω_1 - ω_2. In the case where $\omega_1 = \omega_2$, this manifests as second harmonic and "dc" pulses, respectively. The optical pulses have a duration of ~100 fs and, thus, a broad bandwidth of a few terahertz. The difference frequency signal, therefore, arises from high frequency components mixing wih the low frequency components within a pulse, with a resulting frequency in the terahertz range, as desired. This signal is, therefore, a dc pulse rather than a steady dc electric field.

The underlying mechanism can be briefly explain as follows. When an electromagnetic wave is incident on any material, the sinusoidally fluctuating electric and magnetic fields induce a similar sinusoidal oscillation in the electrons in the matter at the same frequency but at a phase lag. In the linear optical regime, the induced electric dipoles are proportional to the amplitude of the applied electric field and can be satisfactorily modelled using the classical Lorentzian model [144, 162]. However, this changes when an intense ultrafast laser pulse is incident on a noncentrosymmetric crystal (lacking an inversion symmetry) such as ZnTe. Because of the non-zero second order susceptibility $\chi^{(2)} \neq 0$ component, the higher order terms need to be included in the model [143, 166–171]. If the incident wave is monochromatic, i.e, $E_0 \cos(\omega t)$, it generates second order dielectric polarisation

$$P^{(2)} = \chi^{(2)} E_0^2 \cos^2(\omega t) \tag{3.16}$$

$$= \chi^{(2)} E_0^2 \left[\frac{\cos(2\omega t) + 1}{2} \right] \tag{3.17}$$

$$= \frac{1}{2}\chi^{(2)} E_0^2 \cos(2\omega t) + \frac{1}{2}\chi^{(2)} E_0^2 \tag{3.18}$$

The first term is the second harmonic of the fundamental frequency, while the second term is the DC rectification term. If instead of the CW sinusoidal wave, an ultrashort broadband laser pulse is used for exciting the medium, the rectification term can be written as $\frac{1}{2}\chi^{(2)} E_0^2 \eta^2(t)$, where $\eta(t)$ is the envelop function of the excitation pulse. This is true if the $\chi^{(2)}$ dispersion is negligible near the optical frequency. In case of a Gaussian pulse with duration τ_p and centre frequency ω_c, the rectification induced polarisation will, therefore, be

$$\frac{1}{2}\chi^{(2)} e^{-2a\tau_p^2} E_0^2 \tag{3.19}$$

In the far field the emitted electric field is proportional to the second time derivative of the dielectric polarization [170], leading to a typical single cycle terahertz pulse, as shown in Figure 3.15.

Nonlinear crystals are dispersive both at optical and terahertz frequencies because the refractive index n(ω) is a function of frequency ω. The optical pulse travels through the nonlinear medium at group velocity $v_g(\omega) = \frac{\partial \omega}{\partial k}$ while the induced THz pulse travels with phase velocity $v_{ph}(\omega) = \frac{\omega}{k}$, where $k(\omega) = n(\omega)\frac{\omega}{c}$. Therefore, velocity matching between the femtosecond and terahertz pulses can be obtained only at a certain THz frequency, such that the optical pulse envelop travels at the same velocity as the monochromatic THz wave velocity [143, 170, 172]. ZnTe, therefore, is the most most widely used non-linear crystal for implementing optical rectification because the group refractive index near λ=812 nm

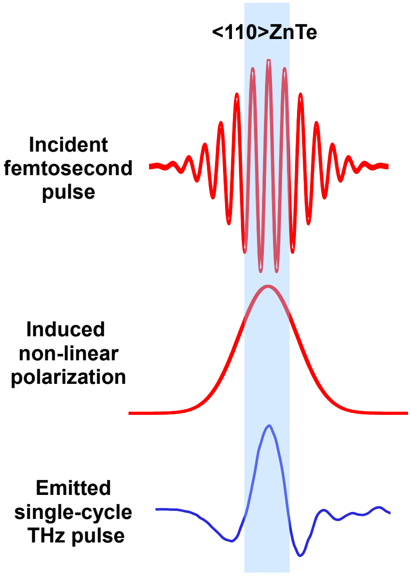

Figure 3.15: An intense ultrashort laser pulse induces 2^{nd} order polarization within the nonlinear $< 110 >$ ZnTe medium, which in turn causes a long wavelength single-cycle terahertz pulse to be emitted due to optical rectification.

matches with the THz refractive index at 1.69 THz.

Despite fulfilling the velocity-matching condition at a certain THz frequency, there is always a refractive index mismatch within the optical and terahertz bandwidth, and the thickness of the nonlinear crystal such as ZnTe has to be optimized in order to ensure constructive interference between THz radiation fields induced in different layers of the crystal. This ensures maximum amplification of the THz signal while traversing the ZnTe crystal. The thickness of the crystal used in the experimental setup depends, therefore, on a compromise between the desired THz bandwidth and THz signal intensity. More details can be found in Chapter 3 of Ref 143.

Because ZnTe has an non-symmetric crystal structure, the non-linear polarization and, hence, the induced THz radiation power depend on the direction of incident optical field with respect to the ZnTe crystal axes. Maximum THz is generated when the linearly polarised femtosecond pulse propagates along the [110] axis of the ZnTe crystal with an angle θ between the optical field and the [001] axis, such that

$$I_{THz}(\theta) = \frac{3}{4} I_{THz}^{max} \sin^2\theta (4 - 3\sin^2\theta) \tag{3.20}$$

The maximum THz intensity I_{THz}^{max} is obtained at $\theta = \sin^{-1}\sqrt{\frac{2}{3}}$, corresponding to the incident electric field being parallel to either the $[\bar{1}11]$ or $[1\bar{1}1]$ axis [143].

The spectral bandwidth of THz generation in a non-linear crystal is limited by absorption in the THz frequency region. The dominant absorption processes are transverse optic (TO) phonon resonances, usually in the range between 5 to 10 THz. ZnTe has a strong resonance at 5.32 THz [173], therefore it can be used only for measuring THz spectra below or above this wavelength range. Alternative crystals can be used to avoid this limitation. Some other well-researched materials include GaSe (6.4 THz) [174], GaP (11 THz) [175], GaAs (8.1 THz) [174] and InP (9.2 THz) [176].

3.5.4 Electro-optic sampling

The THz pulse is detected using free-space electro-optic sampling (EOS) in a thin $< 110 >$ ZnTe crystal. Unlike most other pump-probe measurements where only the electric field intensity is measured, EOS measures the THz electric field (both amplitude and phase information) in the time-domain. This information gives us the complex dielectric constant in the photoexcited sample, as discussed below in Section 3.6.2.

EOS is based on the Pockels effect whereby a voltage applied on the ZnTe detector crystal produces birefringence in the optical medium which is proportional to the applied electric field [135, 136, 143, 171, 177–181]. A low energy femtosecond laser pulse is used as a gate pulse. Since the gate pulse duration is much smaller than the THz pulse (few fs compared to ~1 ps), the terahertz field appears to be quasi-static on the time-scale of the gate pulse. When the linearly polarised gate pulse traverses the nonlinear crystal, its polarisation rotates depending on the birefringence state of the crystal. This, in turn, is a function of the part of the picosecond-long THz waveform currently passing through the crystal. The magnitude and direction of polarisation rotation are directly proportional to the THz field amplitude

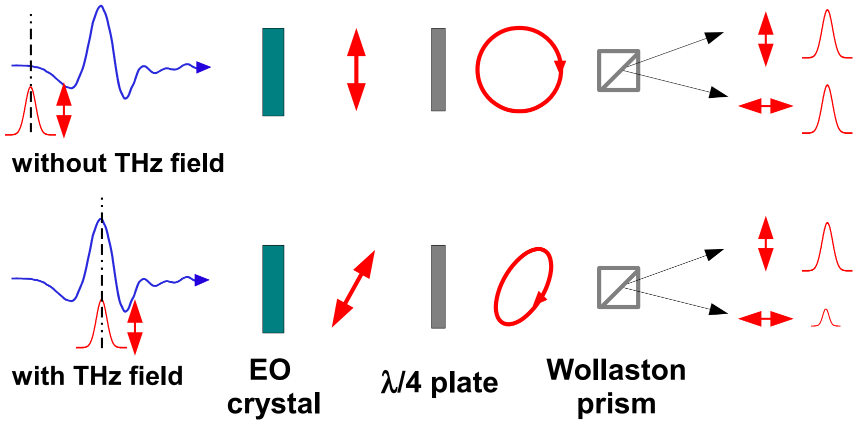

Figure 3.16: A schematic showing free-space electro-optic sampling (EOS) used in the OPTP experimental set-up. The delay between the linearly polarized ∼40 fs gate beam (red pulse) and THz signal (blue pulse) is systematically varied. The electro-optic effect in the nonlinear crystal causes rotation of the gate pulse polarization in the presence of the THz field. The quarter-wave plate balances the two linear polarization components, followed by the Wollaston prism which separates the gate pulse into its s- and p-polarizations. The relative amplitude of each state (indicated by red pulses at the right) provides the differential signal detected by the pair of balanced photodiodes. The amount of gate pulse polarisation is exaggerated for demonstration; typically polarization rotations smaller than 10% are expected.

and sign. In this manner, the entire THz waveform (amplitude and phase) can be mapped out in the time-domain by successively increasing the delay between the gate pulse and THz pulse.

The concept is shown schematically in Figure 3.16 and the implementation details can be found in Section 3.5.5.

In electro-optic sampling, there is a trade-off between the sensitivity and frequency response that is determined by the choice of crystal and its thickness. A thicker crystal produces a longer interaction length and therefore a higher signal-to-noise ratio (SNR), but on the other hand, it reduces the THz bandwidth due to group-velocity mismatch [179, 182]. As discussed earlier in the case of dispersion in $< 110 >$ ZnTe crystal, $n(800\,\text{nm}) = 2.853$ and $n(300\,\text{mm}) = 3.178$, leading to a group-velocity mismatch of around 1 ps/mm between the optical probe and THz radiation [181, 182]. The effective crystal thickness, and thus the effective interaction length depends on the depth of focus of the THz beam at the crystal, and thus on the focusing paraboloid mirror. If the THz beam is focussed to a diffraction limited spot size on the detector crystal, the effective crystal thickness is of the order of the wavelength, about 300 μm. The product of this effective crystal thickness and group-velocity mismatch should be less than the pulse duration to obtain the actual THz waveform without artefacts [180, 182]. $< 110 >$ ZnTe satisfies this condition and is, therefore, used in the experimental setup described in the following section.

The phase retardation $\Delta\phi$ induced in the femtosecond probe pulse due to the Pockels effect over a propagation distance d is directly proportional to the electric field of the THz pulse, given by [143]

$$\Delta\phi = \frac{2\pi}{\lambda_{gate}} d n_{gate}^3 r_{41} E_{THz} \tag{3.21}$$

where λ_{gate} and n_{gate} are the wavelength of the gate pulse and the refractive index of the crystal at λ_{gate} respectively; r_{41} is the electro-optic coefficient of the crystal. Therefore, $\mathrm{E_{THz}}$ can be estimated once $\Delta\phi$ is measured. For ZnTe, $r_{41} = 3.9\times10^{-12}\,\mathrm{m/V}$ [183], $n_{\mathrm{gate}} = 2.8$. The temporal or spectral resolution of this technique is limited by the finite pulse duration of the optical probe, the dispersion of nonlinear susceptibility, and the mismatch between optical group and THz phase velocity as discussed in detail already. The measured EO signal is, therefore, a convolution of $\mathrm{E_{THz}}$ with the detector response [138, 184]. Since the main measurement of interest in the following experiments is the change in the terahertz field due to absorption in the photoexcited sample, measuring the exact absolute terahertz field is not crucial, and hence details such as the calibrated frequency-response of the EO crystal can be neglected in this study.

3.5.5 OPTP Set-Up

Briefly, a 1 mJ 800 nm wavelength pulse of 40 fs generated from the 1 KHz amplified Ti:Sapphire laser [Spectra Physics *Spitfire Pro*] is split into three pathways:

1. **Optical pump pulse**: Approximately half of the pulse energy is used as an optical pump pulse to photoinject carriers into the sample under study. The 800 nm pulse is used to generate either a 400 nm pulse through frequency-doubling using a BBO crystal, or pulses with wavelength between 475–700 nm by pumping an optical parametric amplifier (OPA) (Spectra Physics *TOPAS*).

2. **THz probe pulse**: The other half of the 800 nm beam is used to generate a single cycle of THz radiation using non-resonant optical rectification in a 2 mm thick $< 110 >$ ZnTe crystal. This pulse was used to probe the photoexcited sample in transmission mode. Some of the THz field gets absorbed by any mobile charge carriers within the sample. The remaining transmitted pulse is measured using a double lock-in technique. The change in THz field is proportional to the photoinduced sample conductivity in case of a uniformly excited thin film.

3. **Optical gate pulse**: A very small part of the 800 nm beam ($\sim$2 μJ) is used as a gate pulse for measuring the THz field via free space electro-optic sampling (EOS) using a 1 mm thick ZnTe crystal.

A detailed sketch of the experimental set-up is shown in Figure 3.17. The Spitfire beam is split into three parts using dielectric beamsplitters BS1 and BS2. The beam intended for generating THz pulses traverses a computer controlled linear translation stage (DS-3) and is passed through an optical chopper with frequency f_1 set and phase-locked to half the repetition rate of the amplifier, at 500 Hz. A gold-coated off-axis parabolic mirror (OAP-1) is used to focus the near infrared (NIR) beam along the [110] axis of the non-linear crystal, with an angle θ between the polarized electrical field and the [001] axis optimized for maximum signal, as described in Section 3.5.3. The crystal is placed slightly before the focal plane of OAP-1 in order to avoid crystal damage due to the intense laser fluence at the focal spot. Also, the THz emission efficiency is observed to drop off once two-photon effects start taking place inside the crystal. The resulting single cycle of terahertz radiation exits the crystal surface co-linearly with the leftover femtosecond pulse. A thin sheet of cellulose nitrate (CN) is used to scatter the 800 nm pulse while allowing the THz pulse to pass through unhindered.

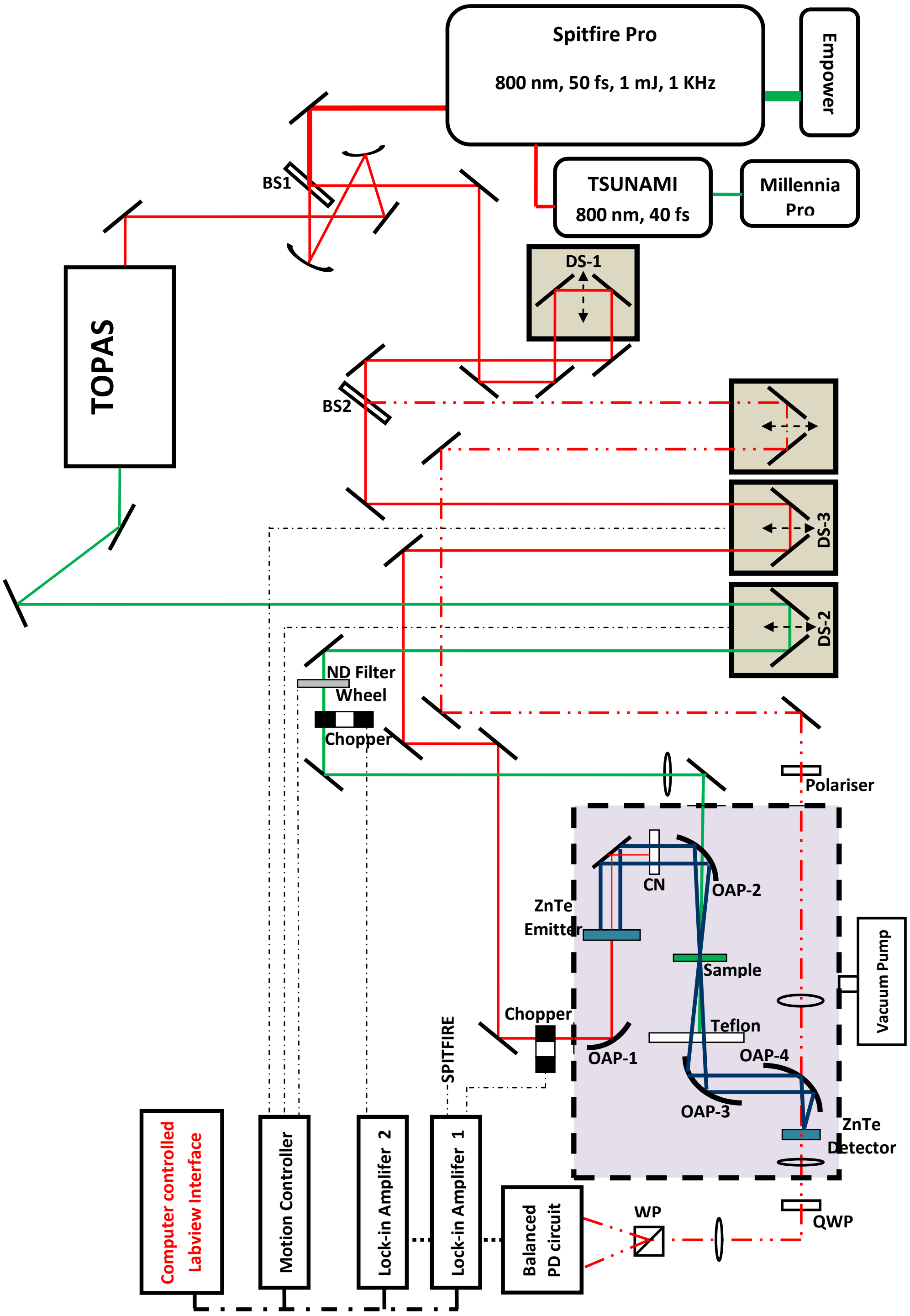

Figure 3.17: Schematic of the OPTP experimental set-up when pump beam is generated using TOPAS. Bold black lines at 45°: mirrors, BS: beam-splitters, DS: delay-stage, OAP: off-axis parabolic mirrors. Red solid line: 800 nm beam, red dash-dot-dot line: gate beam, green line: pump beam generated from TOPAS, blue line: THz beam, black dash-dot line: electrical connections.

The terahertz pulse is focused on the sample surface using another gold-plated off-axis parabolic mirror (OAP-2). The transmitted terahertz pulse is then collimated by the OAP-3 mirror. The sample holder is aligned with respect to both these OAPs such that the sample surface is at the focal planes of both mirrors. The collimated terahertz is finally focussed using OAP-4 on a 1 or 2 mm thick $< 110 >$ ZnTe crystal where the transmitted THz field is measured using electro-optic sampling and the gate pulse. Before reaching the detection crystal, the gate pulse is passed through a polariser in order to ensure a completely linearly polarised ultrashort duration pulse. The pulse train is focused through a small hole in the centre of OAP-4 using a lens which is aligned such that the gate beam is focused a few millimeters beyond the crystal. This is done to prevent any fluence-induced damage to the crystal. The THz pulse-train, on the other hand, is focused exactly on the crystal in order to maximise the signal. Also, this ensures that the gate beam spot size on the crystal is larger than the THz spot size, making sure that all the information carried in the THz pulse gets recorded through the gate pulse polarization state.

When the linearly polarised femtosecond gate pulse and the THz pulse propagate collinearly and simultaneously through the electro-optic crystal, the field-induced birefringence alters the polarisation state of the probe pulse as shown in Figure 3.16. A quarter wave plate (QWP) converts this into a nearly-circular polarisation, which is then split into its two orthogonal components by a Wollaston prism, as shown in Figure 3.17. A pair of biased p-i-n photodiodes are used to measure the relative intensity of the two components. A circuit-diagram of the balanced photodiode circuit is shown in Figure 3.18. In the absence of a terahertz field, the differential output from the photodiodes is forced to zero by rotating the QWP to balance the horizontal and vertical components of the gate pulse. Any deviation from zero could arise if the gate pulse is not completely vertically/horizontally polarized before arriving at the EO crystal or because of slightly different sensitivities of the two photodiodes. The change in polarisation is directly proportional to the difference in voltage measured in the two photodiodes, V_{sig}, and the maximum voltage swing V_{full}, given by

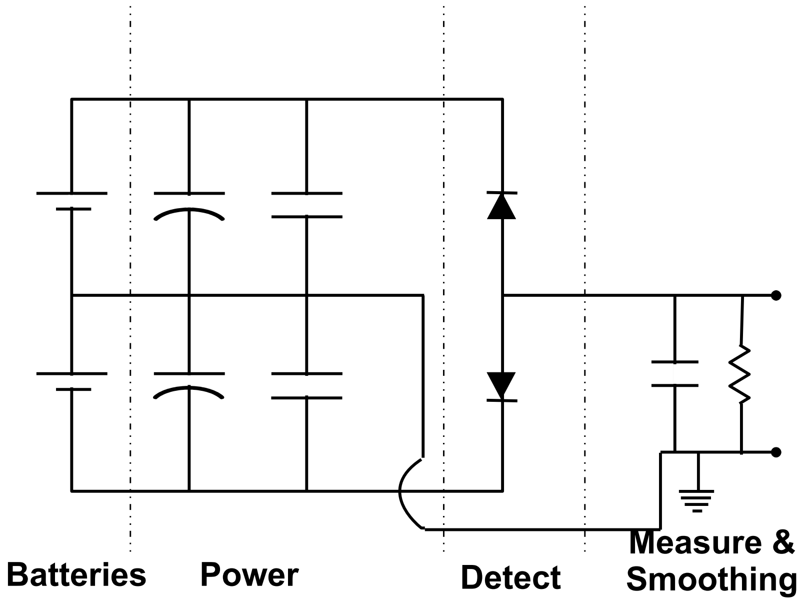

Figure 3.18: Circuit diagram of the balanced photodiodes (pds) used to measure change in polarization of 800 nm gate beam due to the terahertz electric field. Detect: PDs in reverese-bias mode. Power: Current is drawn from batteries (24 V each) every millisecond, when the gate pulse shines on the pds. The supply voltage is filtered by 1000 μF electrolytic capacitors to narrow the ripple voltage caused by the current draw. Smaller 0.1 μF ceramic capacitors are used to compensate for the internal inductance of the electrolytic capacitors at high frequencies. Measure & Smoothing: A resistor R acts at a differential photocurrent-to-photovoltage converter. A capacitor is used to form a RC filter with cut-off frequency logarithmically between the laser repetition rate and THz chopping frequency ($\frac{1}{RC} \approx$ 600–700 Hz). A small ceramic capacitor ($\leq$0.1 μF) is chosen to ensure minimal inductive effect at high frequencies. The RC filter, therefore, filters away the individual 1 KHz repetition rate laser pulses from the desired THz signal at about 500 Hz. R can be adjusted to obtain a voltage signal within the desired sensitivity range of the lock-in. It should be large enough to provide a signal measurable by the lock-in, yet not so large that the lock-in is saturated. Also, increasing R increases the signal-to-noise (SNR) as $R^{1/2}$ [185].

$$\Delta\phi = V_{\mathrm{sig}}/V_{\mathrm{full}} \tag{3.22}$$

E_{THz} can then be calculated using Eqn 3.21. A pair of dual-phase lock-in amplifiers (Stanford Research Systems *SR830*) are used to measure $\Delta\phi$, as described in Section 3.5.6 later.

The sample is photoexcited with the remaining second half of the 800 nm amplifier beam. In order to compensate for the extra pathlength traversed by this beam when passing through the TOPAS, the other half of the Spitfire beam used to generate the THz and gate pulses is passed through a fixed linear delay stage (DS-1). The TOPAS can accept a maximum beam size of about 5–6 mm FWHM so a pair of curved (concave and convex) mirrors is used as a telescope to reduce the ∼8 mm Spitfire beam diameter. Since the relative position and orientation of the crystals inside the TOPAS are varied slightly in order to generate different wavelengths, the output beam alignment is different for different wavelengths and two mirrors placed immediately after the TOPAS exit are used to realign the beam each time the output wavelength is changed. This beam path is shown with the green solid line in the Figure 3.17. The beam traverses another computer-controlled linear translation stage DS-2. The beam energy is controlled using a reflective variable neutral density filter mounted on a computer controlled rotation stage. This can be used to either conduct measurements with a range of excitation fluences or to ensure a constant photon flux for each excitation wavelength. The second optical chopper is set at a frequency f_2 much lower than the pulse repetition rate, at a value which is not an integer multiple of f_1, usually at 44 Hz.

A lens is used to focus the beam through a hole in the centre of OAP-2. The lens is positioned so that its focal plane lies beyond the sample. As before, this avoids any risk of damaging the sample. Also, this can be used to control the optical spot-size on the sample in order to control the incident fluence. The spot-size is measured using the knife-edge method with a razor-blade mounted on a manual translation stage. The total power of the unblocked beam is measured using a bolometer as the blade is translated across the beam cross-section. Assuming a Gaussian beam profile, the power is differentiated along the scan direction, yielding the Gaussian FWHM (full width half maximum) spot-size. The pump spot-size should be much larger and well-overlapped with the THz probe spotsize on the sample surface. While the high frequency components of the terahertz probe can be successfully focused into a tight near-diffraction limited spot-size, the low-frequency components form a larger spot-size. As a result, if the pump spot size is the same size as the THz spot size or smaller, the optical excitation effect would be observed in the high frequency THz spectrum but absent from the low frequency part of the spectrum, thus complicating measurements [134, 186]. Also, the optical and THz beams are collinearly propagated to minimize temporal smearing [134]. Finally, any unwanted optical beam transmitted through the sample is scattered away using a thick teflon block which lets the THz signal through unhindered.

Alternatively, photoexcitation can also be done at 400 nm. As shown in Figure 3.19, in this case, the TOPAS is bypassed and immediately after being split off from the main 1 mJ spitfire beam, the pump beam is redirected using dielectric mirrors towards the delay stage DS-2. The fixed linear translation stage DS-1 is also bypassed. The optical paths travelled by the pump and probe beams are carefully adjusted to make sure the pulses have good temporal overlap at the sample surface. The 800 nm pulse is frequency-doubled using a 300 μm thick BBO (β-BaB$_2$O$_4$) crystal mounted in a manual rotation stage [187, 188]. For Type I phase matching the incident polarization must be parallel with the axis of rotation of the crystal. The horizontally polarized Spitfire beam, therefore, needs to be rotated by 90°. This is done by using a home-built polarisation rotation cube with seven mirrors inside which reflect the beam in orthogonal directions such that the output beam is vertically polarised compared to the input beam polarisation state. The pump beam walks an extra 8 cm inside the polarisation rotation cube and the optical path of the probe beam has to be accordingly increased. The optic axis of the crystal is orientated to maximise the efficiency of frequency-doubling. The blue beam is now focused through the hole in the OAP-2 on to the sample surface as described earlier.

It is useful to note that, as far as possible, all optics on the bench are reflective. This is done to minimize the temporal and spectral broadening of the femtosecond pulse-train due to dispersion and chirp. Dielectric mirrors from Altechna are used on the 800 nm beam path because of their high ($> 99\%$) reflectivity between 700–900 nm. Protected silver mirrors are used on the optical pump delay line after the NIR wavelength is changed to the visible range. In case of photoexcitation at 400 nm, the frequency-doubling is done very close to the sample and the only mirror involved is swapped for a UV-enhanced aluminium mirror. All the optics used for guiding the THz beam towards the sample and the detector crystal are reflective and gold-coated. Gold is used because it exhibits reflectivity higher than 99% over a broad THz

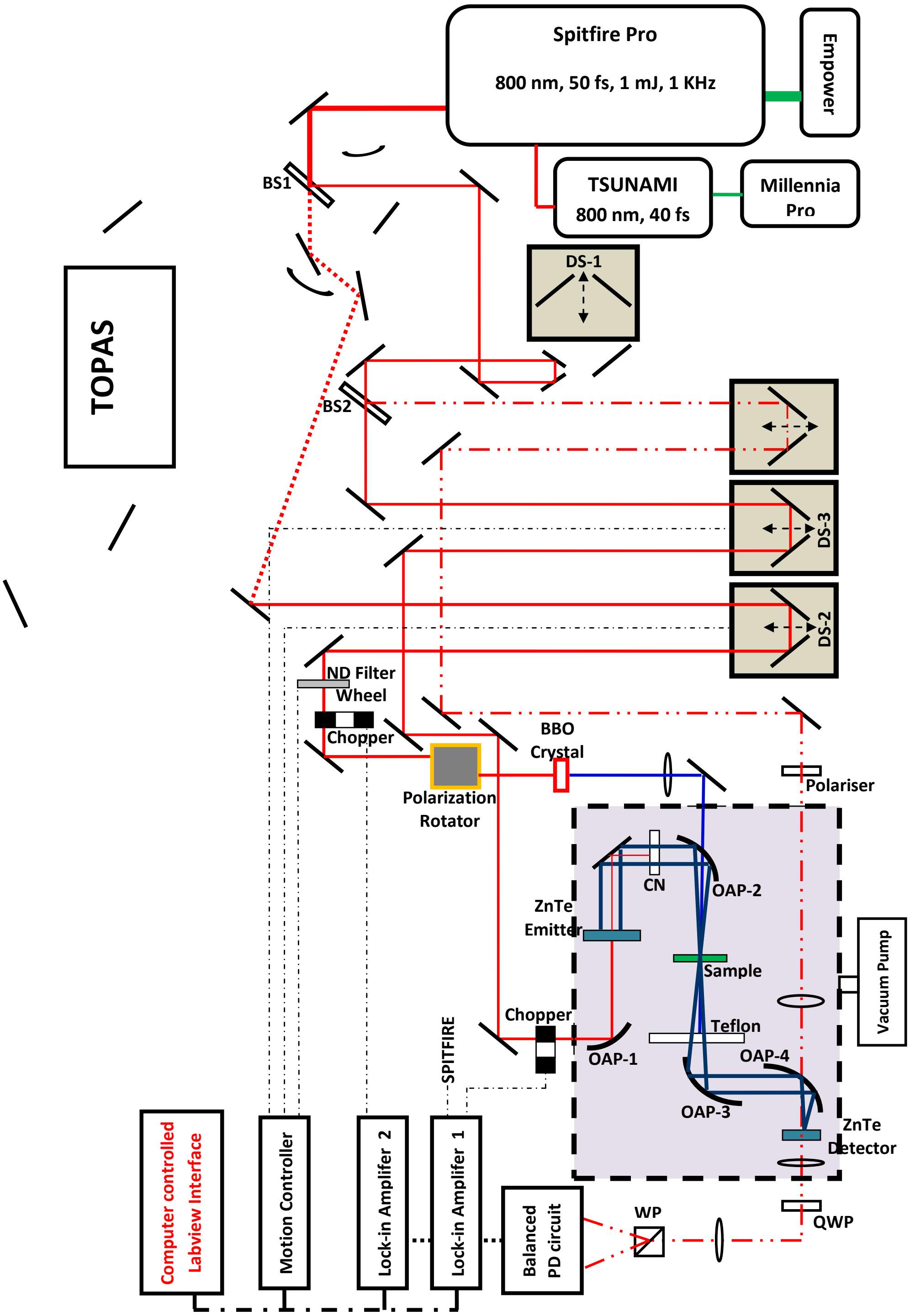

Figure 3.19: Schematic of the OPTP experimental set-up when pump beam is generated using BBO crystal. The TOPAS is bypassed, and the altered pump beam-path is shown with the red dotted line. The polarization rotator flips the beam polarization state to vertical, and the BBO crystal converts 800 nm to 400 nm via frequency-doubling.

spectrum. It is well-understood from the free-electron model that metals are highly reflective for frequencies below plasma frequency and transparent to higher frequencies, and the plasma frequency in gold is very high, in the $10^{15}\,\mathrm{s}^{-1}$ range [143, 144]. Off-axis parabolic (OAP) mirrors are used for focusing or collimating the terahertz beam instead of transmissive lenses because this minimizes any losses due to absorption or Fresnel reflections. Also, parabolic mirrors work over a broad spectral range without spectral aberration and are also free from spherical aberration [189]. This enables focusing a broad collimated beam to a diffraction-limited spot, as required in the OPTP experiments. However, OAP alignment needs to be done extremely precisely since imaging is highly sensitive to astigmatism.

There are three main ways of collecting OPTP data depending on which beamline is scanned. The gate beam delay stage is always kept fixed in all experiments.

1. A **1D probe scan** is obtained by fixing the pump delay line (DS-2) and scanning the THz probe delay line (DS-3). The ∼40 fs pulse temporally overlaps with a certain part of the ∼1 ps THz waveform. By changing the delay τ' between the THz probe and optical gate pulses, the entire THz waveform can be mapped out for a fixed time τ after sample photoexcitation (Figure 2.8). This yields the frequency-dependent optical properties of the sample at a fixed time after photoexcitation.
2. A **1D pump** scan is obtained when the THz probe delay line is fixed at one point of the THz waveform, eg. at the peak of the THz pulse. The optical pump delay line is now scanned, yielding useful information about how the peak or average THz absorption evolves as a function of time τ after photoexcitation.
3. A **2D pump-probe scan** where both the optical pump and THz probe delay lines are scanned synchronously. This allows the full THz waveform (and thus the full THz spectrum) to be measured for increasing delay after photoexcitation. This measurement provides a full time-resolved spectral response of the photoexcited material and, therefore, offers an unambiguous picture of the early-time charge dynamics taking place in the system. Understandably, the measurements are time-consuming and require a long-drawn 2D data-analysis.

3.5.6 Double lock-in detection

A pair of dual-phase lock-ins is used to measure the change in THz transmission $\Delta T/T$ as a result of photoexciting the sample. The first lock-in (LIN1) is referenced to the probe chopper 1 which is phase-locked to half the amplifier repetition rate, at f_1=500 Hz. LIN1 time-constant τ_1 is set such that $\tau_1 \gg 1/f_1$. The second lock-in (LIN2) is referenced to the pump chopper 2 at a much lower rate such that $f_2 \ll 1/\tau_1$, typically at 44 Hz. LIN2 time-constant τ_2 is set such that $\tau_2 \gg 1/f_2$, usually at 1 sec. For each data point measured during the pump or probe scans, the delay stage is paused for time t_{settle} chosen such that $t_{\text{settle}} \gg \tau_2$, typically at 3 sec.

The sample is excited by the pump pulse with a repetition rate f_2. The desired measured quantity is the relative pump induced change in terahertz transmission

$$\Delta E/E_0 = \Delta T/T = (T_{ON} - T_{OFF})/T_{OFF}$$

To this purpose, the first lock-in is set up so that its output is proportional to the terahertz signal E_0 via Eqn 3.21 where $\Delta\phi$ is measured as discussed in Eqn 3.22. The output from LIN2 is proportional to ΔT. In reality, LIN1 output equals the average transmitted THz signal, $(T_{ON} + T_{OFF})/2 \approx T_{OFF}$, if $\Delta T \ll T_{OFF}$. This approximation is true only if the modulated signal is less than 1% of the incident field. The experiments are set-up such that this condition is satisfied, as seen in the results to follow. Typically measured values of $\Delta T/T$ using the double lock-in technique in this experimental set-up is between 10^{-5} and 5×10^{-4}. The interpretation of the measured data $\Delta E/E_0 = \Delta T/T$ will be discussed in Section 3.6.2.

3.5.7 Sample preparation

For all THz experiments reported in this thesis, the samples were prepared by spin-coating a metal-oxide nanoparticle paste on z-cut quartz substrates and sintering them at 500°C over 3 hours in air. Thick films were prepared by applying multiple coats of the metal oxide paste. Between consecutive coats, the films were heated at 140°C for 5 minutes to evaporate the solvent, in order to prevent the previous coat from getting washed away by the solvent in the next coat. The detailed recipes for the TiO_2, SnO_2 and ZnO nanoparticle pastes and their respective sintering temperatures are given in Section 3.1.1. Z-cut quartz is used because of its transparency in the optical and terahertz frequency range and absence of optical birefringence along that axis.

The mesoporous films were sensitized by soaking the samples in dye solution overnight in the dark at room temperature. The dye solution comprised 0.3 mM Z907 ruthenium dye in acetonitrile/tert-butanol (1:1 vol %) solvent (Section 3.1.2). After removing from the dye solution, the samples were rinsed briefly with acetonitrile and allowed to dry. The optical density of the films was measured using a spectrophotometer (Section 3.4) to ensure sufficient coverage of the nanoparticles with the dye molecules. The samples were then immediately stored in a nitrogen glovebox away from light, until they were used for the terahertz measurements. The steady-state UV-vis absorption of the samples was measured before and after each THz pump-probe experiment in order to verify negligible sample degradation due to photo-oxidation.

3.6 THz data analysis

3.6.1 Steady-state THz time-domain spectroscopy

When a terahertz pulse passes through a sample, the complex refrative index $\tilde{n}$ of the sample causes both retardation and attenuation of the transmitted THz pulse, as seen in Figure 3.20. Since the electro-optic sampling technique enables the transient electric field to be measured, and not just its intensity, this enables both the amplitude and phase of the transmitted THz pulse to be measured. The Fourier transform of the time-domain data can be used to calculate the absorption coefficient and index of refraction of the sample as a function

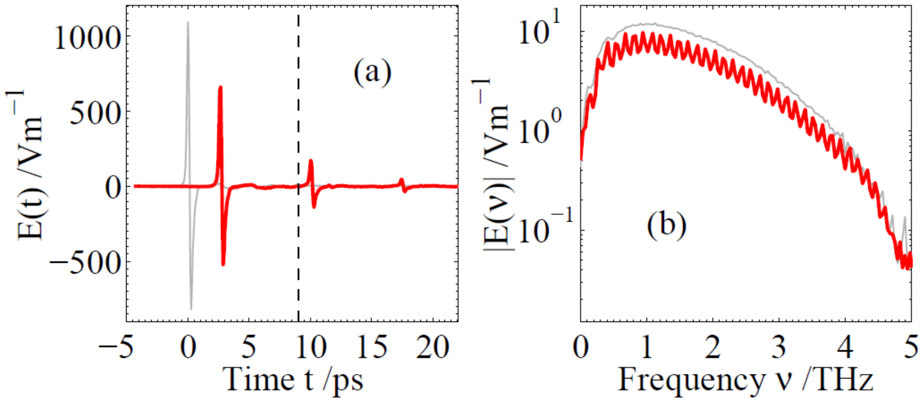

Figure 3.20: Typical THz-TDS data obtained when transmitted through an optically thick sample (high resistivity silicon, 0.33 mm thick). (a) Time-domain terahertz pulse transmitted through sample (thick red line) is delayed by 2.6 ps with respect to reference terahertz pulse (thin grey line) due to the medium's refractive index. Absorption and reflection in the sample explain the reduction in amplitude of the transmitted pulse. Two internal reflections are shown in this data-set, at 10.0 ps and 17.4 ps. (b) Fourier transform spectra of respective time-domain data shown in (a). The multiple internal reflections produce the oscillatory shape of the transmitted THz spectrum, and can be minimized by restricting the time domain data to up to 9 ps (dotted line in a). Taken from Ref 190.

of frequency. Thus the complex refractive index and, hence also, the complex dielectric constant of the material can be measured without the need for invoking the Kramers-Kronig relationships [144].

As seen in example shown in Figure 3.20, most time-domain THz probe scans show more than one THz pulses due to multiple reflections within the sample or reflections from the THz emitter or EOS detector crystals. In order to account for all the reflections, precise knowledge of the complex refractive indices of the different optical components is required. Iterative numerical methods for calculating the sample refractive index in the presence of Fabry-Perot reflections has been explored in detail by various research groups [190–194]. This calculation can be significantly simplified by making sure that either the samples and sample substrates are so thin that the reflections overlap ($L < 10$ nm) or so thick ($L > 1$ mm) that the reflections are far enough to be ignored by selecting the appropriate time-window, as shown by the dotted vertical line in Figure 3.20.

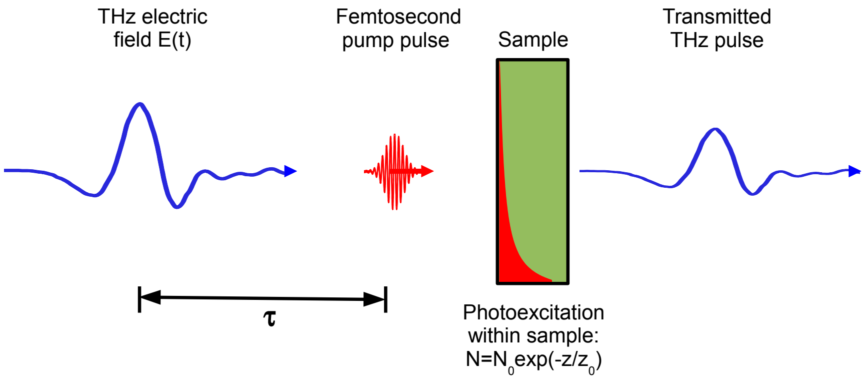

Figure 3.21: The optical pump pulse at wavelength λ_{pump} gets absorbed within a certain depth z_0 inside the sample (optical penetration depth, OPD), depending on the sample optical density at that wavelength. The transmitted terahertz pulse, therefore, is absorbed within this photoexcited region. In all cases discussed in the following chapters, OPD $\gg$ sample thickness, and the photoexcitation profile can be assumed to be constant within the sample, as discussed in the subsection 'limitations' in Section 3.6.2.

3.6.2 Time-resolved OPTP spectroscopy

In an optical pump terahertz probe experiment, an ultrashort pump pulse excites the sample, typically creating or exciting charge carriers. These photoexcited charge carriers are then probed with the broadband pulse of terahertz radiation. A typical case is depicted schematically in Figure 3.21. This is similar to the more conventional optical pump-probe spectroscopy, apart from the fact that it is possible to measure the full time dependence of the electrical field of the THz probe pulse, instead of only its energy or energy spectrum. By means of Fourier analysis, the full complex absorption spectrum can be obtained, which describes both amplitude change and the phase shift due to photoexcitation as a function of frequency.

Data analysis - probe scan

In the case of a 1D probe scan, the pump delay is kept fixed while the THz probe pulse is delayed with respect to the optical gate pulse. Figure 3.22 shows a typical output from both lock-ins, where LIN1 measures T(t) and LIN2 measures ΔT(t), both in V/m units, as

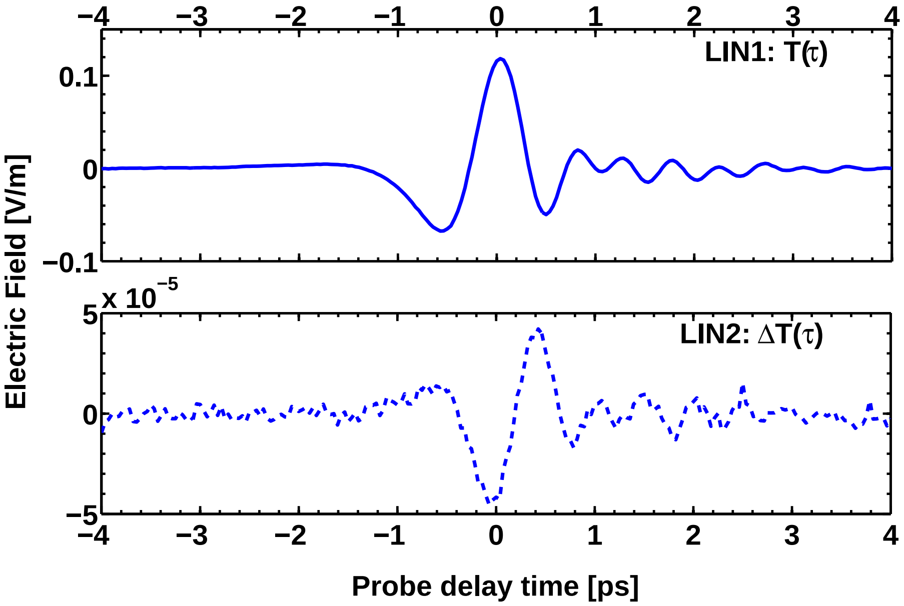

Figure 3.22: A 1D time-domain THz probe scan conducted on a nanostructured film of TiO_2 photoexcited at 400 nm with an incident fluence of ∼10^{14} photons/cm^2. The x-axis depicts delay τ' between the THz probe and optical gate pulse, as defined in Figure 2.8. The two graphs show T and ΔT signals measured using lock-ins 1 (LIN1) and 2 (LIN2) respectively.

described in Section 3.5.6. The measurements have been conducted on a mesoporous film of sintered TiO_2 nanoparticles photoexcited at 400 nm. The probe scan was conducted at τ=5 ps after photoexcitation. The time-window has been selected so that the reflected THz pulses (discussed in Figure 3.20) are excluded. $E_0(t)$ and $\Delta E(t)$ can be directly calculated from these measurements via Eqn 3.21.

The electric field of the THz pulse generates a current density J(t) within the thin photoexcited sample. It can be derived from Maxwell's equations that the current density can be obtained experimentally from the difference between the reference THz field $E_0(t)$ passing through the non-photoexcited sample and the field E(t) passing through the photoexcited sample of thickness L [138, 184, 195–198] via

$$\mathrm{J(t)} = -\frac{\epsilon_0 \mathrm{c}(\mathrm{n_a} + \mathrm{n_b})}{\mathrm{L}}[\mathrm{E(t)} - \mathrm{E_0(t)}] \tag{3.23}$$

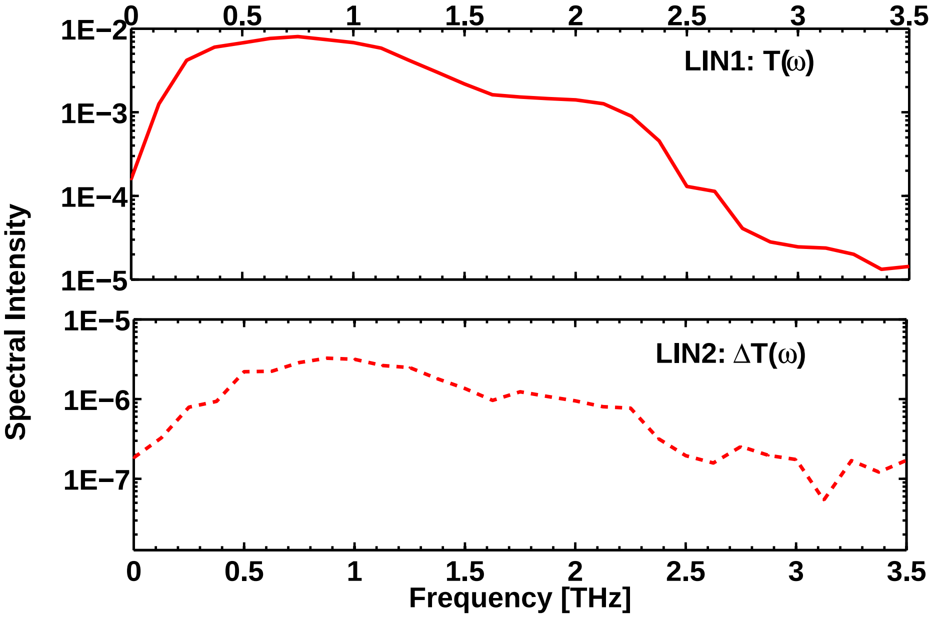

Figure 3.23: Fourier transforms of the time-domain signals shown in Figure 3.22. Meaningful signal is meausured between ∼0.2–2.2 THz, allowing almost two orders of magnitude between the signal peak and noise floor.

where $\mathrm{n_a}$ and $\mathrm{n_b}$ are the refractive indices of the surrounding materials, ϵ_0 is the dielectric constant of vacuum, and c is the speed of light. The intrinsic sample conductivity $\sigma(\omega)$ can be measured from these experimentally measurable parameters from

$$\mathrm{J(t)} = \mathrm{Re}[\sigma(\omega)\mathrm{E_0e^{-i\omega t}}] \tag{3.24}$$

To perform this calculation, the incident terahertz electric field $\mathrm{E_0(t)}$ and the measured time-domain current density waveform J(t) must first be Fourier-transformed to obtain the equivalent spectral information, using

$$\mathcal{F}[\mathrm{f(t)}](\omega) \equiv \int_{-\infty}^{\infty} \mathrm{f(t)e^{i\omega t}dt} \tag{3.25}$$

Figure 3.23 shows the spectral response in the terahertz frequency regime for both $\mathrm{T}(\omega)$ and $\Delta\mathrm{T}(\omega)$ shown earlier in Figure 3.22.

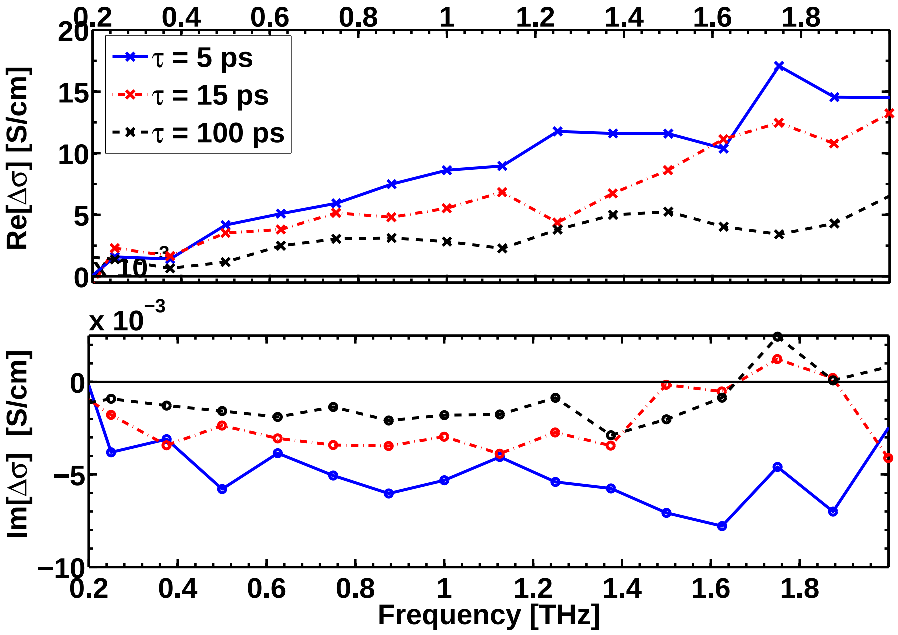

Figure 3.24: Real and imaginary parts of conductivity in nanostructured TiO_2 in the 0.2–2.0 THz regime, calculated by applying Eqn 3.28 on the data shown in Figure 3.23.

Therefore, Eqns 3.23, 3.24 and 3.25 can be combined to solve for the complex conductivity spectrum $\sigma(\omega)$ of the sample.

$$\begin{aligned}
\Delta\sigma(w) &= \frac{\mathcal{F}[J(t)](\omega)}{\mathcal{F}[E_0(t)](\omega)} \qquad (3.26)\\
&= -\frac{\epsilon_0 c(n_a+n_b)}{L}\frac{\mathcal{F}[E(t)-E_0(t)](\omega)}{\mathcal{F}[E_0(t)](\omega)} \qquad (3.27)\\
&= -\frac{\epsilon_0 c(n_a+n_b)}{L}\frac{\mathcal{F}[\Delta T(t)](\omega)}{\mathcal{F}[T(t)](\omega)} \qquad (3.28)
\end{aligned}$$

Carrying out this operation on the data shown in Figures 3.22 and 3.23 yields the complex conductivity of photoexcited TiO_2 as shown by the real and imaginary components in Figure 3.24. Here, ΔT/T has been measured at different time-delays after photoexcitation (at $\tau =$ 5, 15 and 100 ps). The character of the spectrum is typical for carriers exhibiting localization at nanometer scale, in agreement with published reports [104, 129, 199]. Re[$\Delta\sigma$] increases with frequency and Im[$\Delta\sigma$] is negative, unlike the free-carrier Drude response observed in single TiO_2 crystals [105, 144]. Unlike the Drude response where maximum conductivity is observed at $\omega \rightarrow 0$, the DC conductivity in nanoparticle samples is supressed (Re[$\Delta\sigma_{DC}$]$\approx$0), suggesting very poor long-range mobility in the nanostructured samples. DC measurements are dominated by the slowest conduction step as charges are moved over relatively large distances and DC conductivity is, therefore, negligible in the case of nanostructured films. Much higher conductivity values are observed in the terahertz frequency range because the higher frequency THz radiation probes intrinsic material properties and is not much affected by macroscopic disorder or sparse defects. This is discussed in more detail in Chapter 4.

Figure 3.24 also shows that both the real and imaginary components of $\Delta\sigma$, and thus, both the photoinduced change in refractive index and absorption coefficient are decreasing with increasing delay after the photoexcitation. This follows logically from the data shown ahead in Figure 3.25. In addition to identifying free charge carriers, the spectral signature of the complex conductivity in the terahertz frequency range can be used to distinguish between other charge quasiparticles such as excitons (bound electron-hole pairs), polarons (lattice deformations associated with free carriers), surface plasmons (coherent electron oscillations at a metal-dielectric interface), exciplexes etc [83, 100, 105, 140, 141, 200] (details in Appendix A).

Limitations

It is important to note here that Eqn 3.23 is valid only for very thin samples, such that the optical penetration depth (OPD) $\gg$ sample thickness, L, unlike the case depicted in Figure 3.21. This constraint forces the excitation density to be nearly constant as a function of distance along the sample. The calculated sample conductivity can, therefore, be assumed to be constant along the z-direction. However, if OPD<L, the z-dependence of conductivity needs to be accounted for and the analysis is much more complicated [184].

This is also a reminder that because the true conductivity is a function of the depth, z, inside the sample, the conductivity evaluated in Eqn 3.28 is the average value across the entire sample photoexcited volume,

$$\sigma(\tau) = \int_0^L \sigma(\tau, \mathrm{z})\mathrm{dz} \tag{3.29}$$

Also, the above analysis is valid only in the steady-state case and is more complicated in the following two cases [138, 184]. First, at early pump-probe delay times the visible excitation pulse arrives at the sample as the THz pulse is propagating through it. The visible pulse affects only the trailing part of the THz pulse; therefore, the THz pulse experiences a different set of propagation parameters at the trailing end of the pulse than it did at the beginning. Second, the properties of the sample change rapidly during the excitation by the pump pulse, or the sample properties change faster than the duration of the terahertz pulse. The analysis is much more complicated in these cases and has been avoided by ignoring data before $\tau = 3\,\mathrm{ps}$. Additionally, as discussed in Section 3.5.4, the steady-state assumption also allows for the detector response function to be ignored, as it simply gets divided out in data analysis [138].

Data analysis - pump scan

In this case the relative delay between the THz probe pulse and 800 nm gate pulse, τ', is kept fixed such that only one point of the terahertz waveform is measured, typically the peak of the terahertz pulse (Figure 2.8). The optical delay between the optical pump and terahertz probe pulses, τ, is varied in order to map the change in THz absorption in the photoexcited sample as a function of τ. Here, $\tau = 0$ is defined as the temporal overlap of the femtosecond excitation pulse with the peak field strength of the THz probe pulse. The experiment is set up such that the trend can be measured over a delay of up to 1250 ps after excitation.

As discussed in the previous section, in the steady-state case, $\Delta\sigma(\tau)$ can be calculated as

$$\Delta\sigma(\tau) = -\frac{\epsilon_0 \mathrm{c}(\mathrm{n_a} + \mathrm{n_b})}{\mathrm{L}} \frac{\Delta\mathrm{T}(\tau)}{\mathrm{T}(\tau)} \tag{3.30}$$

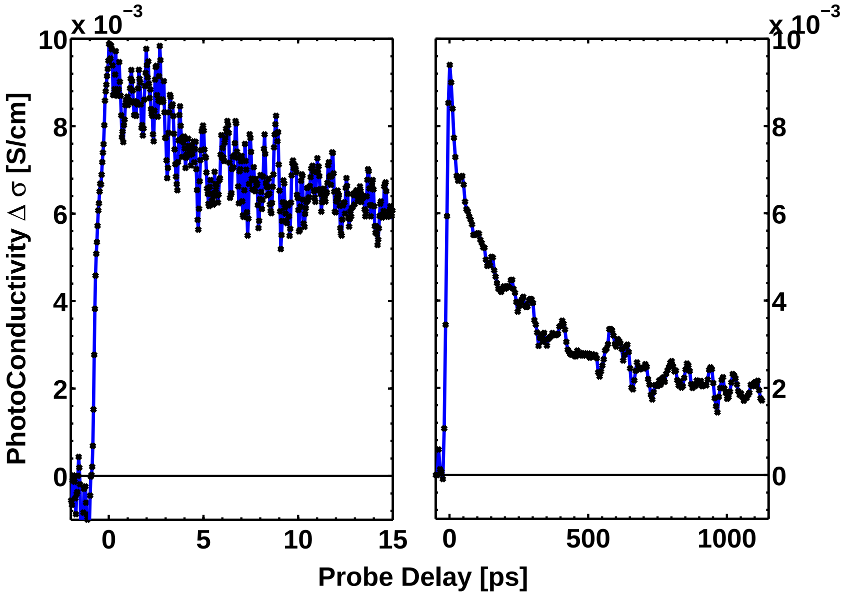

Figure 3.25: Early- and later-time photoconductivity scan measured on a nanostructured TiO_2 film kept under vacuum and photoexcited with 400 nm ∼40 fs pulses with 3×10^{14} photons/cm^2 incident fluence. The x-axis depicts the increasing delay τ between the optical pump and THz probe pulses, and the y-axis shows $\Delta\sigma \propto \Delta T/T$ as calculated from Eqn 3.30.

An example of a pump-scan can be seen in Figure 3.25, showing the measured change in photoinduced conductivity as a function of time, in a sintered nanostructured TiO_2 film after photoexcitation at 400 nm.

3.6.3 General comments about experimental conditions

As mentioned in Section 3.5.3, ZnTe has a strong resonance at 5.32 THz, thus setting the upper limit for the measurable spectral bandwidth. The usable bandwidth is however limited to 0.2–2.2 THz. This is because of the phase-matching constraint in both the emitter and detector ZnTe crystals used in the experimental set-up. Since the main interest in the results shown in the following chapters was in measuring the 1D pump-scans, thick ZnTe crystals were employed for maximizing the THz field strength at the cost of narrow spectral bandwidth. Typical photoinduced change in terahertz transmission measured was $\Delta T/T \approx 4\times10^{-4}$.

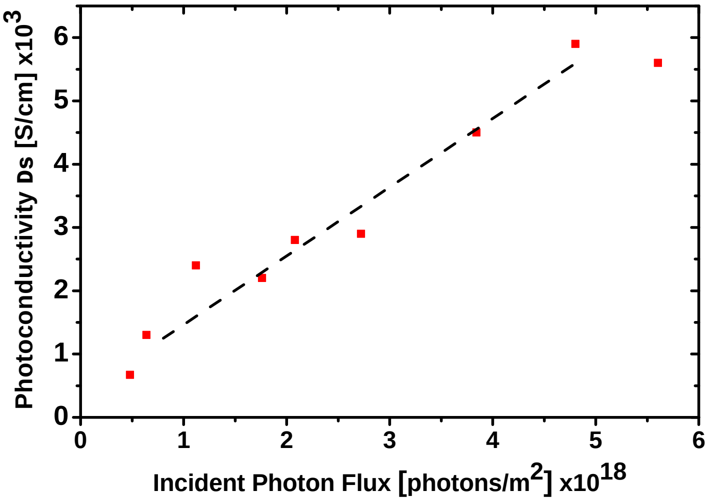

Figure 3.26: Linear fluence dependence of ΔT/T observed in a nanostructured TiO$_2$ film photoexcited at 400 nm. In all OPTP measurements reported in this thesis, it has been ensured that the photoexcitation fluence is kept low enough to be in the linear regime.

The entire terahertz beam path is enclosed in an evacuated box and all measurements are performed at room temperature at pressures below 10^{-3} mbar. This is done to minimize the water-vapour and oxygen content of the local environment around the terahertz beam and the sample. This is because water vapour has many terahertz frequency absorption lines which degrade the signal-to-noise ratio [201]. Also, the oxygen content is minimized to prevent degradation of the photoexcited samples through photooxidation.

The incident pump fluence was kept low in order to avoid charge-charge interactions [202], typically at about 10^{13}–10^{14} photons/cm^2/pulse. This is equivalent to the solar energy incident on a DSC under standard operating conditions. An example of the power dependence of the photoinduced terahertz conductivity in nanostructured TiO$_2$ excited at 400 nm is shown in Figure 3.26. It can be seen to be in the linear regime as desired.

3.6.4 Extracting carrier mobility information

The early-time photoconductivity measured via OPTP spectroscopy can be used to measure the charge carrier mobility in the material. This is a more useful material parameter than conductivity because it is independent of both the excitation fluence and the sample geometry, and it is easy to compare between different OPTP measurements and different experimental techniques. Section 4.3.1 gives details for estimating the ‘effective carrier mobility’ $\phi_{\mathrm{inj}}\mu_{\mathrm{peak}}$ while Eqn 5.1 gives a detailed methodology for extracting the carrier mobility from this data, once the charge injection efficiency has been estimated through photovoltaic related measurement techniques.

Chapter 4

Electron Dynamics in Nanostructured TiO_2 Electrodes in DSCs

This chapter reports the experimental results obtained from optical-pump terahertz-probe (OPTP) spectroscopy on mesoporous anatase TiO_2 films, commonly employed as the electron-transporting electrode in dye-sensitized solar cells. The intrinsic electron mobility value is calculated to be $\sim 0.1\,\mathrm{cm^2/Vs}$ with an approximately 20 nm diffusion length for electron motion through the TiO_2 matrix. The photoconductivity dynamics in TiO_2 films, both before and after sensitization with Z907 ruthenium dye, are examined in order to study the charge injection, trapping and recombination time-scales. Biphasic electron injection is observed, with a fast sub-500 fs component followed by a slower 70–200 ps component. This is followed by photoconductivity decay over the first few nanoseconds, predominantly reflecting charge carrier trapping. In addition, terahertz spectroscopy is employed to investigate the influence of treating the titania surface with $TiCl_4$ on early time charge dynamics. In the solar cells, surface treatment of the mesoporous TiO_2 with $TiCl_4$ is critical to enable efficient operation. Here, OPTP reveals that neither early-time charge mobility, nor charge injection rate or decay times are significantly affected by the treatment, which suggests that it may instead have an impact on phenomena occurring on longer time scales.

4.1 Introduction

TiO_2 is currently the most popular choice for the electron-transporting layer in high efficiency DSCs. Section 2.3.2 emphasises the need for a suitably fast electron transport mechanism within the mesoporous semiconductor matrix in order to enable satisfactory overall device performance. Over the past few decades, a large amount of theoretical and experimental work has been carried out to allow a better understanding of electron injection into and movement through the semiconductor matrix towards the electrode, with the aim of increasing the charge generation and collection efficiency [62, 104, 105, 117, 139, 145, 203–209]. However, most of the current understanding of the electron dynamics in TiO_2 is based on indirect estimates derived from the application of electron-transport models. These include various modifications of the Drude model [104, 134], effective medium theory [105] or Monte Carlo [61, 210] or FTDT simulations [211]. Time-resolved microwave conductivity (TRMC) spectroscopy offers a useful probe for directly mapping electron dynamics in the semiconductor, but can only achieve nanosecond temporal resolution [145].

In this chapter, OPTP spectroscopy has been used to measure the change in photoconductivity in TiO_2 as a function of time after excitation, in the sub-picosecond to nanosecond time range. Measurments carried out on mesoporous TiO_2 films with and without dye-sensitization are used to estimate the early-time electron mobility and electron injection rate, and also to estimate the early-time trapping and recombination rates. The effect of treating TiO_2 films with $TiCl_4$ on charge injection and trapping rates has also been probed, with the intention of identifying the mechanisms that result in increased photocurrent and efficiency in $TiCl_4$-treated DSCs. Information obtained from studying photoconductivity dynamics can be crucial in answering questions about the efficacy of different dye-sensitizers and of various surface treatments in improving charge injection and electron diffusion lengths in the DSCs and therefore provides valuable input for the optimization of electron transport and device performance.

4.2 Experimental Details

Samples were prepared as outlined in Section 3.5.7 by spin-coating multiple coats of TiO_2 paste on z-cut quartz. The TiO_2 paste was procured from the Grätzel lab at EPFL. Some samples were also prepared using a TiO_2 paste purchased from Dyesol (18NR-T) and diluted with ethanol. Both pastes comprised of ∼20 nm diameter anatase TiO_2 nanoparticles. The sintered films were transparent, 2–4 μm thick, and ∼60% porous[3] [10].

In order to understand the effect of $TiCl_4$ treatment on TiO_2-based DSCs, some of the TiO_2 films were soaked in a 20 mM aqueous solution of $TiCl_4$ for 4 hours at room temperature

---

[3] Measurement done by Michael Grätzel's group at EPFL

in the dark (Section 3.1.6). After rinsing with DI water and drying in air, the films were then resintered to 500°C for 45 minutes. This was followed by dye-sensitization with Z907 dye, as described in Section 3.1.2

Complete solid-state DSCs were fabricated using the methodology outlined in Section 3.1.6. Dyesol $\mathrm{TiO_2}$ paste was applied on the FTO substrate by doctor-blading and the resulting sintered film thickness was 1.4 μm. Similar to the THz samples, some of these films were treated with $\mathrm{TiCl_4}$. The devices were then completed with Z907 dye, spiro-OMeTAD HTM with *t*BP and Li-TFSI salts, and silver electrodes. Current-voltage characteristics of the DSCs were measured under 1 Sun AM1.5G conditions, as described in Section 3.2.1.

The OPTP spectroscopy technique has been described in detail in Section 3.5.5. A 1-D pump scan was conducted and the measured change in amplitude of the peak value of the THz pulse, $\Delta\mathrm{T}/\mathrm{T}$ was used to infer the change in sample photoconductivity $\Delta\sigma(\tau)$ as a function of probe delay, τ, using Eqn 3.30, rewritten below:

$$\Delta\sigma(\tau) = -\frac{\epsilon_0 \mathrm{c}(\mathrm{n_a} + \mathrm{n_b})}{\mathrm{L}} \frac{\Delta\mathrm{T}(\tau)}{\mathrm{T}(\tau)}$$

Here, L is the sample thickness (l) or the optical penetration depth (OPD), whichever is smaller. In case of the undyed $\mathrm{TiO_2}$ films, $l \ll$ OPD. In the presence of the dye molecules, $l \approx$ OPD for excitation wavelengths below 550 nm and much smaller otherwise, as seen in Figure 4.1 c). $\mathrm{n_a}$ and $\mathrm{n_b}$ are the refractive indices of the media immediately before and after the photoexcited material, respectively, in the THz frequency range. n_b is, therefore, the refractive index of either the substrate (quartz, 1.95) or of non-photoexcited $\mathrm{TiO_2}$ ($\sim$2.5) [104], depending on OPD (which is a function of wavelength).

4.3 Results and Discussion

4.3.1 Carrier mobility in bare TiO_2

First, the photoconductivity dynamics in bare TiO_2 samples are probed (without dye sensitization). Figure 4.1 a) and b) show the early- and later-time variation in photoconductivity as a function of probe delay τ, for an as-sintered TiO_2 sample excited at either 400 nm or 550 nm with $\sim 3\times 10^{14}$ photons/cm^2 incident fluence, measured under low vacuum. Figure 4.1 c) shows the UV-Vis absorption spectra for mesoporous TiO_2 films with and without dye, and with and without $TiCl_4$ treatment. For photoexcitation at 400 nm, close to the anatase TiO_2 bandgap [57, 209], a resolution-limited rise time $t_{1/2}$ of $\sim$500 fs in the photoconductivity is observed. It has already been demonstrated that the photoconductivity in TiO_2 is dominated by the electron response [139, 205]. This ultrafast rise, therefore, indicates direct excitation of electrons into the conduction band (CB) or into sites lying close to the CB which may form a mobility edge. On the longer time scale, a slower decay in photoconductivity is observed with a lifetime of $\sim$1.5 ns. The photoconductivity, $\sigma(\tau)$, is a function of both the carrier mobility $\mu(\tau)$ and the number of mobile carriers $\mathrm{N}(\tau)$ which can interact with the THz pulse, as $\sigma(\tau) = \mathrm{N}(\tau)\mathrm{e}\mu(\tau)$, where e is the electronic charge. Thus the observed decay in conductivity illustrates either reduced mobility as τ increases, or decreased number of mobile electrons due to charge trapping and/or recombination, or a combination of all three factors.

Monte Carlo simulations in combination with transient photocurrent and transient absorption spectroscopy measurements have revealed that the electron transport through the TiO_2 network predominantly occurs in the conduction band, with the conduction band electrons being populated by multiple trapping-detrapping events from the energetically distributed intra-bandgap states [62, 203]. This multi-trapping mode of charge transport will result in decreasing average charge mobility $\mu(\tau)$ with increasing time τ after photoexcitation. As τ increases, mobile electrons will become immobilized in sub-band gap traps in TiO_2, while some electrons will be lost through recombination within the TiO_2 film. The

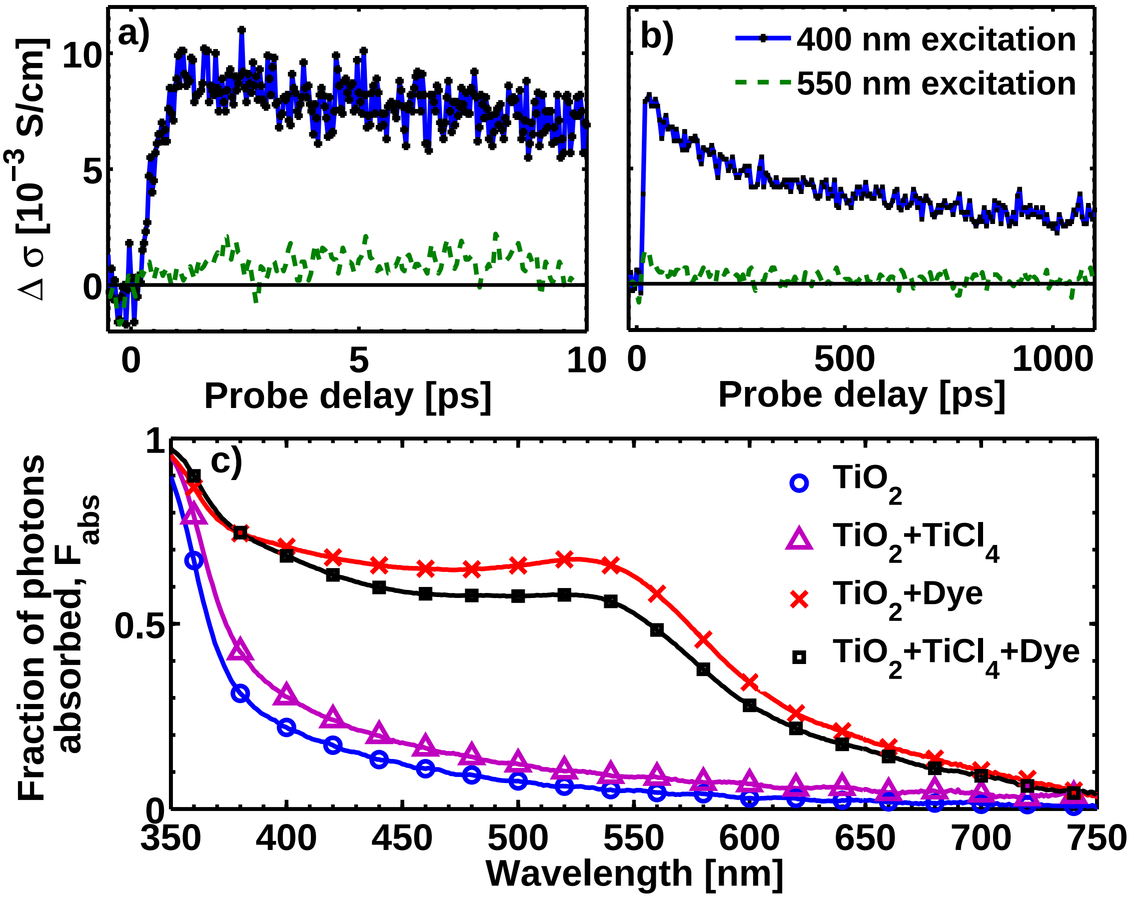

Figure 4.1: a) Early-time and b) later-time photoconductivity dynamics in mesoporous TiO_2 upon photoexcitation at 400 nm (blue solid line with black crosses) and 550 nm (green solid line), with incident fluence ~3×10^{14} photons/cm^2, and pulse duration ~40 fs. A photoconductivity rise 'half-time' of ~500 fs is observed, followed by a slow decay over 1-2 ns. c) Steady-state absorption spectra of TiO_2 samples with and without $TiCl_4$ treatment, both before and after dye-sensitization.

observed photoconductivity decay over the first couple of nanoseconds corroborates this discussion and suggests that this is a typical trapping time-scale.

For practical analysis, extraction of the carrier mobility value is more useful than the photoconductivity since the mobility is independent of both sample geometry and excitation fluence. Therefore, the term 'effective mobility" $\phi_{\mathrm{inj}}\mu_{\mathrm{peak}}$ is introduced, defined as the product between the peak charge mobility value μ_{peak} at delay time $\tau = \tau_{\mathrm{peak}}$ (when the highest photoconductivity signal $\Delta\sigma_{\mathrm{peak}}$ is measured), and the quantum yield ϕ_{inj} for charge separation per absorbed photon (or electron injection efficiency in the case of a dye-sensitized sample). $\phi_{\mathrm{inj}}\mu_{\mathrm{peak}}$ is calculated from experimental observables through

$$\phi_{\mathrm{inj}}\mu_{\mathrm{peak}} = \frac{\Delta\sigma_{\mathrm{peak}}}{\mathrm{eF_{abs}N_{incident}}} \tag{4.1}$$

where e is the electron charge, N_{incident} is the incident photon density, and F_{abs} is the fraction of photons absorbed in the photoexcited region of the sample, derived from the steady-state absorption spectrum of the sample (Section 3.4).

Figure 4.2 shows values of $\phi_{\mathrm{inj}}\mu_{\mathrm{peak}}$ extracted in this manner for different films as a function of excitation fluence. For as-sintered TiO_2 obtained from EPFL (black △'s), an average value of $0.1\pm0.03\,\mathrm{cm^2/Vs}$ is observed while samples made using the Dyesol TiO_2 paste (blue ○'s) exhibit a similar value of $0.06\pm0.01\,\mathrm{cm^2/Vs}$. The charge generation efficiency from direct light absorption into TiO_2 near its bandgap is expected to be near unity. The $\phi_{\mathrm{inj}}\mu_{\mathrm{peak}}$ values derived here, therefore, should be very close to the actual peak mobility values of the respective materials, or at least should mark the lower limit on the mobility values.

In addition, Figure 4.2 shows that the carrier mobility is independent of the absorbed photon fluence for most of the range explored, with a small decrease at very high fluences that may however be due to experimental variation. In agreement, other researchers have noted that the incident fluence range over which this data were taken is low enough to avoid charge-charge interaction effects [104, 105, 145]. This also suggests that the early-time conduction band mobility is being probed in the present study, rather than trap-limited

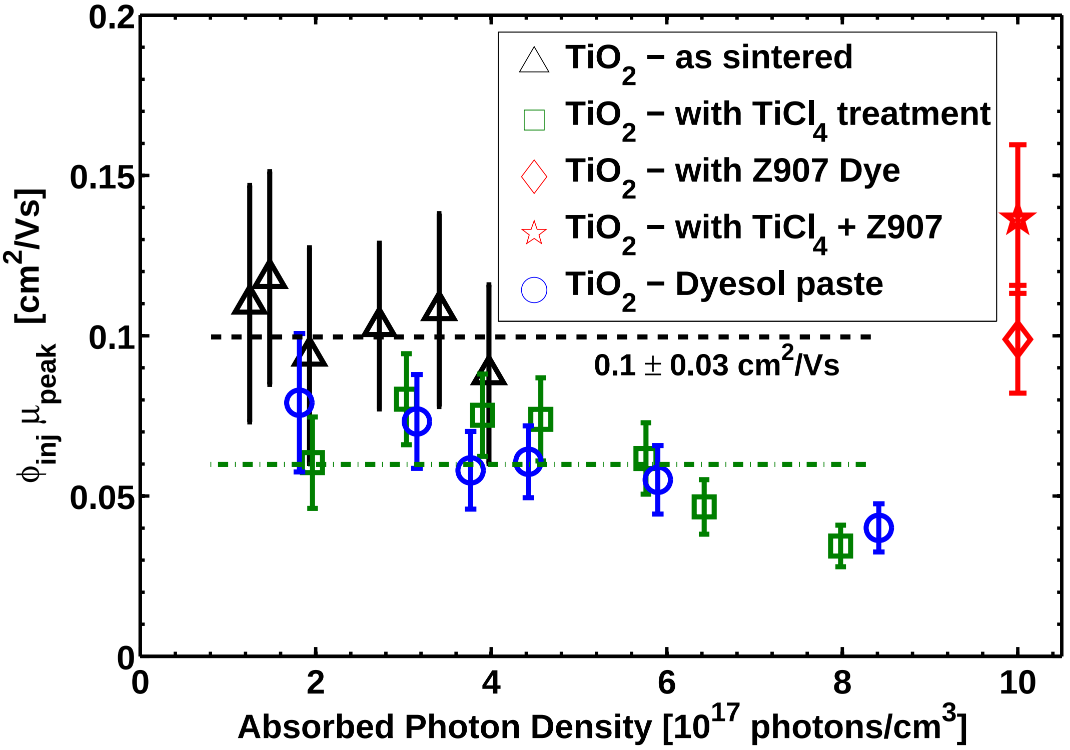

Figure 4.2: Fluence dependence of the effective carrier mobility in TiO$_2$ upon photoexcitation at 400 nm. The absorbed photon density was calculated from the incident fluence and the UV-Vis absorption at 400 nm. All but one of the data sets were measured on samples prepared with home-made TiO$_2$ paste. The samples were: as-sintered TiO$_2$ (black △), TiO$_2$ with TiCl$_4$-treatment (green □), TiO$_2$ with Z907 dye (red ◇), TiO$_2$ with TiCl$_4$-treatment and Z907 dye (red ★), and TiO$_2$ made with dyesol paste 18NR-T (blue ◯). Assuming near unity charge injection efficiency, the average carrier mobility is determined to be 0.1±0.03 cm^2/Vs for TiO$_2$ samples made with home-made paste (black dashed line) and 0.06±0.01 cm^2/Vs for TiO$_2$ films treated with TiCl$_4$ (green dash-dot line).

mobility, which is understood to increase with increasing fluence owing to the gradual filling of the deep bulk trapping sites as the intensity (total number of electrons formed) increases [145, 206].

The carrier mobility values extracted from these measurements can be compared with those previously determined by others for mesoporous TiO$_2$ films. Hendry *et al.* reported a mobility value of 0.01 cm^2/Vs measured using a THz pump-probe technique similar to the one used in this study [105]. However, Hendry's study was based on a TiO$_2$ paste made using Degussa P25 nanoparticles which are a mixture of 80% anatase and 20% rutile TiO$_2$, unlike the 100% anatase TiO$_2$ paste used in this study (as determined by XRD). On the other hand, a much higher mobility value of $15\,cm^2/Vs$ was reported by Turner *et al.* also for a mixture of anatase and rutile TiO_2 nanoparticles [104], using data analysis based on the Drude-Smith model [212]. In addition to the standard Drude model which describes a free electron gas undergoing random elastic scattering events, Turner *et al.* have introduced an extra factor attributed to 90% back-scattering from the grain-boundaries and nanoparticle surfaces. As a result, the modified Drude model yields higher scattering time values as compared to estimates from other models such as the effective medium theory [105]. This results in the extracted mobility value being higher by a couple of orders of magnitude. In contrast, in the results presented here, the carrier mobility has been directly extracted from experimentally measurable parameters, without employing any data-fitting models, and is, hence, the most direct method for estimating the true ac mobility in mesoporous TiO_2.

Time-resolved microwave conductivity (TRMC) experiments at 9 GHz probe frequency have yielded carrier mobility values similar to the ones shown here, ranging between $0.034\,cm^2/Vs$ (using 9 nm anatase TiO_2 nanoparticles purchased from Solaronix [145]) and $0.5\,cm^2/Vs$ (thin anatase TiO_2 film deposited using electron beam evaporation [205]). However, much lower mobility values of $\sim 1\times 10^{-3}\,cm^2/Vs$ and $\sim 7\times 10^{-6}\,cm^2/Vs$ have been reported with transient and quasi-steady state photocurrent experiments [207, 208] and time-of-flight (TOF) measurements [209] respectively, carried out at room-temperature. This difference is not unexpected since the latter experimental techniques probe electron motion over a longer time-scale (microsecond to second time range) corresponding to charge transport over longer distances for which initially mobile electrons have already experienced multiple trapping and detrapping events. The effect of probe-frequency dependence of the conductivity in mesoporous TiO_2 is also demonstrated in Figure 4.3, which shows that the real part of sample conductivity, and hence carrier mobility, increases as the probe frequency increases from DC (steady-state measurements) to terahertz domain, in agreement with other THz studies on TiO_2 [104, 105, 129, 213]. As discussed in Section 3.6.2 and depicted in Figure 3.24, the spectrum is obtained by calculating the Fourier transform of the time-domain THz waveform transmitted through the sample. Transient THz time-domain spectroscopy thus provides crucial information regarding both the time- and frequency-dependence of the photoinduced

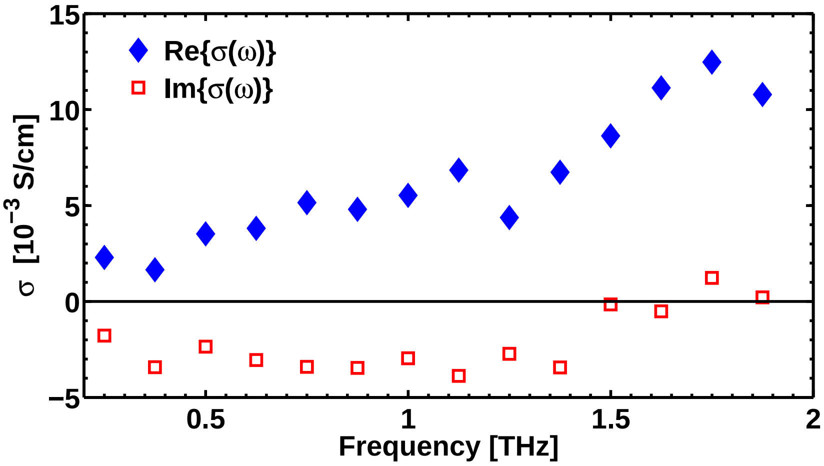

Figure 4.3: Real and imaginary parts of the TiO$_2$ conductivity spectrum in the 0.2–2.0 THz range. Re$\{\sigma(\omega)\}$ increases as frequency increases from DC to 2 THz.

charge conductivity.

The extracted mobility values can be used to estimate the electron diffusion coefficient, $\mathrm{D_e}$, using the Einstein equation:

$$\mathrm{D_e} = \frac{\mathrm{k_B T}\mu}{\mathrm{e}} \tag{4.2}$$

where $\mathrm{k_B}$ is the Boltzmann constant and T the temperature. $\mathrm{D_e}$ is calculated to be approximately $2.5\times10^{-3}\,\mathrm{cm^2/s}$ which is further used to calculate the electron diffusion length through the relationship

$$\mathrm{l_e} = \sqrt{\mathrm{D_e}\tau_\mathrm{e}} \tag{4.3}$$

Based on the typical later-time THz conductivity decay scans shown in Figure 4.1 b), the electron lifetime τ_e is taken to be ∼1.5 ns. This yields a diffusion length, $\mathrm{l_e}$, of 20 nm, which is surprisingly close to the nanoparticle diameter (∼20 nm). This value is, however, much larger than the estimated electron mean free path of 1–2 nm in nanostructured TiO$_2$ [104, 139], promoting the question as to whether the motion of mobile electrons in the mesoporous matrix is limited more by the presence of sub bandgap trap sites or by the physical geometrical constraints of the network. Since the traps are likely to predominantly reside near the nanoparticle surface, this is rather difficult to distinguish.

In their previous work, Hendry *et al.* reported the electron mobility and diffusion coefficient in bulk rutile TiO_2 to be $\sim 1\,\mathrm{cm^2/Vs}$ and $0.025\,\mathrm{cm^2/s}$ respectively [105, 139], and attributed the low values to the strong electron-phonon coupling in TiO_2 (Appendix A.1). In addition to this factor, the values measured in this chapter for mesoporous TiO_2 are further reduced by an order of magnitude, suggesting restricted electron movement because of both geometrical constraints and increased trap-sites in the nanostructured material.

Additionally, in the current experimental study, carrier dynamics in sintered TiO_2 nanoparticles have been probed in a low pressure air matrix. The measured mobility value, therefore, reflects charge dynamics in the nanostructured composite material. Since carrier mobility is a function of the dielectric constant of the medium in which the TiO_2 nanoparticles are embedded [105, 127, 137], the THz pump-probe measurements are expected to yield somewhat different results when performed on TiO_2 infiltrated with the hole-transporter in the complete photovoltaic device.

4.3.2 Effect of dye-sensitization

As a subsequent part of the investigation, TiO_2 films sensitized with Z907 dye were probed using OPTP. Compared to bare TiO_2 samples, sensitization results in higher photoinduced conductivities when exciting at 400 nm. However, this increase can be entirely accounted for by the increased light absorption in the sample at 400 nm due to dye-loading (see Figure 4.1 c)): the effective mobility $\phi_{\mathrm{inj}}\mu_{\mathrm{peak}}$, calculated as described above, is found to be similar to that for the un-dyed films. This is shown in Figure 4.2 (compare $\triangle$ with $\diamondsuit$).

Figure 4.4 shows the early-time photoconductivity transients following excitation of dye-sensitized TiO_2 at longer wavelengths (∼475–700 nm) for which almost all charge injection into TiO_2 occurs via dye excited states, rather than through direct excitation of TiO_2. This was confirmed by the low photoconductivity signal observed in Figure 4.1, when un-dyed

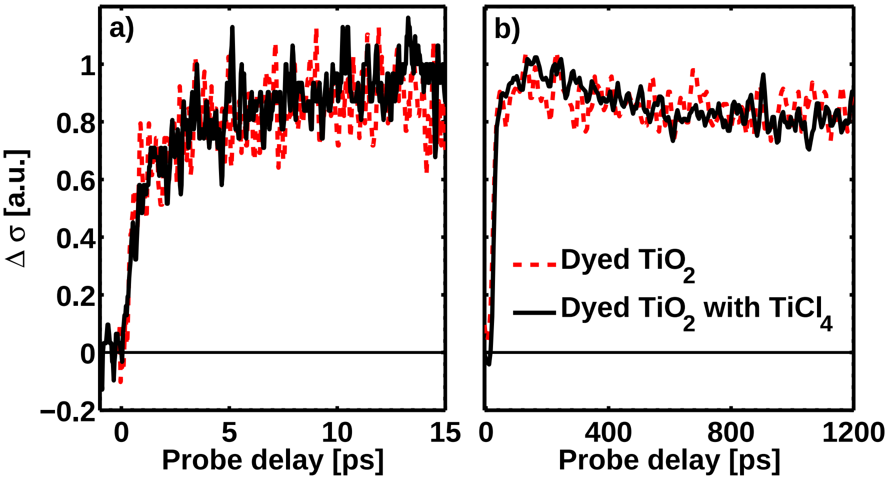

Figure 4.4: a) Early-time (excitation at 625 nm) and b) later-time dynamics (excitation at 500 nm) in dye-sensitized TiO_2 *with* (black solid line) and *without* (red dashed line) $TiCl_4$ treatment for an excitation fluence of ~3 × 10^{14} photons/cm^2. The curves have been normalized at their respective maxima. Similar trends are observed for excitation at wavelengths between 475 and 700 nm, although only selected data is shown here.

TiO_2 was excited at 550 nm. A biphasic charge injection process is observed, with the initial sub-500 fs rise time followed by a slower 70–200 ps rise component. This is in stark contrast with the single-phase ultrafast injection observed in un-dyed TiO_2 upon photoexcitation at 400 nm as shown in Figure 4.1 a). Similar biphasic charge injection kinetics have been observed by other groups, who have suggested that they are caused by injection from the singlet and triplet excited states of the ruthenium complex [71, 76], injection from energetically or spatially diverse sites from the dye into TiO_2 [79], or because of aggregated or loosely attached dye molecules on the TiO_2 surface [77]. Some of these factors have been discussed in general terms in Section 2.3.3. They are also discussed in further detail in the next chapter where this electron injection rate in dye-sensitized TiO_2 has been quantified more rigorously and compared with the electron injection dynamics in other metal oxide films (ZnO and SnO_2).

The nanosecond photoconductivity dynamics of dye-sensitized TiO_2 are shown in Figure 4.4 b) for excitation at 500 nm. The photoinduced conductivity decays over this time window, similar to the case of bare TiO_2, albeit over a slower time period of ~4–5 ns. Transient absorption studies, which probe the charge density, do not usually show such a rapid early time decay, suggesting that the decay in THz conductivity observed here is predominantly due to trapping of mobile electrons, rather than recombination of electrons and holes [117, 206]. Recombination in dye-sensitized TiO_2 has been observed to extend well into the longer microsecond–millisecond time regime, as summarised in Figure 2.5 [10, 51]. On the other hand, faster decay observed in bare TiO_2 in Figure 4.1 b) could be attributed to recombination of the mobile electrons with the holes generated in TiO_2 during photoexcitation, in addition to electron trapping. This change in decay rate upon dye-sensitization has been noted in the past [205]. Very similar early- and later-time trends are observed when the dye-sensitized sample is photoexcited with wavelengths ranging between 475 and 700 nm, although data for only two excitation wavelengths is presented in Figure 4.4. The later-time photoconductivity scans have been fitted with monoexponential decays to estimate the decay times, shown in Figure 4.5 b) as a function of excitation wavelength. Constant values are observed, which suggests that the trapping times are independent of the excitation wavelength. This is consistent with photo-electron transfer taking place directly into the conduction band for all excitations above the optical band gap of TiO_2.

In addition, the effective mobility $\phi_{\mathrm{inj}}\mu_{\mathrm{peak}}$ has been plotted as a function of excitation wavelength in Figure 4.5 a). A constant value of $\sim 0.1\,\mathrm{cm}^2/\mathrm{Vs}$ is found for excitation across the entire absorption spectrum of the dye. Assuming that charge mobility is largely independent of excitation wavelength, the data shown in Figure 4.5 a) mainly reflects changes in the wavelength-dependence of charge injection efficiency. Within experimental error, and accounting for sample-to-sample variation, the injection efficiency appears to be independent of the excitation wavelength. The similarity between the $\phi_{\mathrm{inj}}\mu_{\mathrm{peak}}$ values for un-dyed and dyed TiO_2 further suggests that the charge generation efficiency for the two cases is similar. Since this dye has been used to fabricate high efficiency devices, near unity injection efficiency is not unexpected [27, 65].

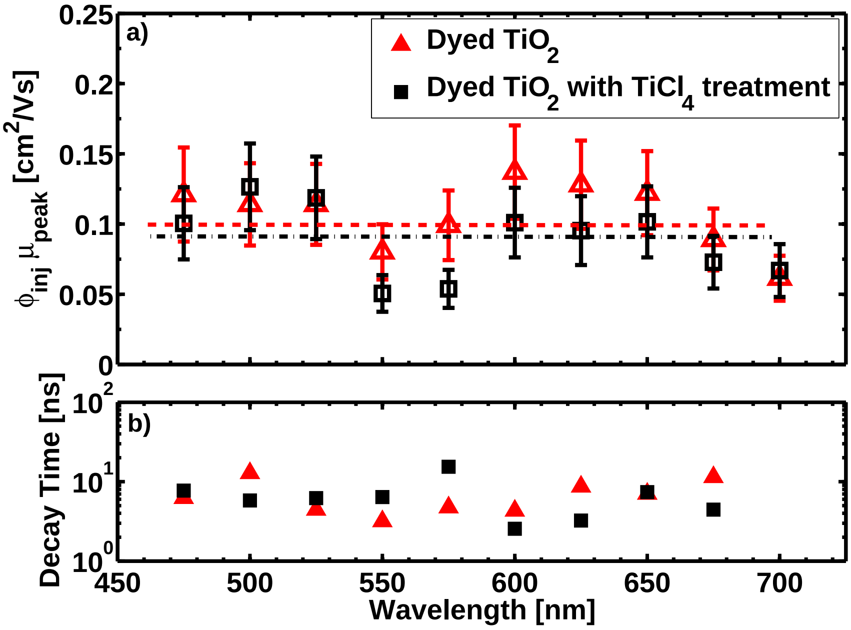

Figure 4.5: Variation in a) effective mobility and b) decay time as a function of excitation wavelength. Red triangles represent dye-sensitized TiO$_2$ and black squares represent dye-sensitized TiO$_2$ treated with TiCl$_4$. The absorbed fluence was about 10^{14} photons/cm^2. The dotted lines in a) indicate the average mobility value for dye-sensitized TiO$_2$ *with* (0.09 cm^2/Vs) and *without* (0.1 cm^2/Vs) TiCl$_4$-treatment.

4.3.3 Effect of TiCl$_4$ treatment

Several research groups have previously reported consistently improved device performance when an extra layer of TiO$_2$ is grown on the surface of the sintered TiO$_2$ nanoparticles by treating the films with TiCl$_4$ [63, 78, 146, 154, 155]. However, the mechanisms underlying this improvement are still poorly understood. This section reports the work done to investigate the impact of such TiCl$_4$ treatment on the early-time (sub-nanosecond) charge carrier injection and mobility in the TiO$_2$ mesoporous film.

To confirm the impact of TiCl$_4$ treatment on device performance, solid-state DSCs were fabricated with and without the surface treatment of the sintered TiO$_2$ film with TiCl$_4$, as described in the experimental section. As expected, the resulting photocurrent-voltage characteristics of the devices (shown in Figure 4.6) demonstrate a dramatic improvement in short-circuit current and efficiency with TiCl$_4$ treatment.

As discussed in detail by Sommeling *et al.* [154], this improvement could be a result

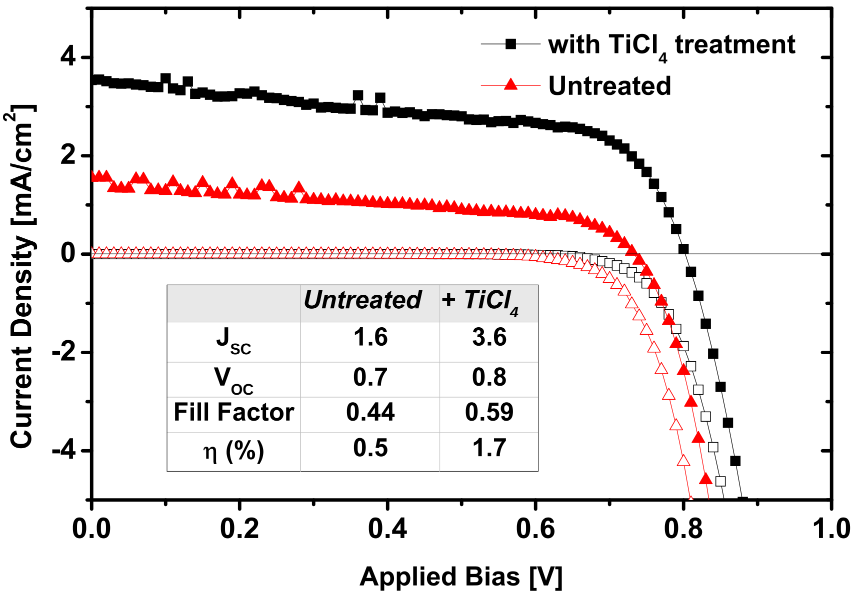

	Untreated	*+ $TiCl_4$*
J_{SC}	1.6	3.6
V_{OC}	0.7	0.8
Fill Factor	0.44	0.59
η (%)	0.5	1.7

Figure 4.6: Current-voltage (JV) curves for solid-state DSCs fabricated with and without prior $TiCl_4$ treatment of the sintered TiO_2 electrodes, measured under simulated AM1.5G solar illumination at an intensity of 100 mW/cm^2. The devices employ Z907 as the sensitizer dye and spiro-OMeTAD with Li-TFSI and *t*BP additives as the hole-transporter.

of increased light harvesting, higher charge injection efficiency and/or increased collection efficiency, which, in turn, is a function of charge transport and recombination times. Increased particle necking between the TiO_2 nanoparticles caused by the $TiCl_4$ treatment has also been suggested as a reason for the improved charge transport [54, 146, 155]. Transient photocurrent measurements, however, have revealed only a marginal improvement in charge transport [63, 154]. Decreased recombination and increased dye-loading have also been observed by Sommeling *et al.*, but they noted that the changes were not enough to explain the increased photocurrent. In agreement with their conclusion, the samples fabricated for this study show improved device performance after $TiCl_4$ treatment even though there is a consistent decrease in dye adsorption (see Figure 4.1 c)). This difference could be attributed to different fabrication protocols. In their conclusion, Sommeling *et al.* have proposed that a positive shift in the TiO_2 conduction band could lead to increased charge injection, and that this may be the main reason for the enhanced device performance.

With this motivation, OPTP has been employed probe the charge dynamics in TiO_2

films treated with $TiCl_4$, in order to investigate if the charge injection rate, carrier mobility or trapping rate in the picosecond to nanosecond time-range are affected as a consequence of the treatment. Figure 4.4 shows the resulting early- and later-time photoconductivity dynamics for dye-sensitized TiO_2 films with $TiCl_4$ treatment in comparison to as-sintered dyed TiO_2 films for a similar absorbed photon fluence. Contrary to expectation, there is no observed increase in charge injection rate as a result of the treatment, even when the samples are photoexcited at a range of wavelengths. In addition, the $TiCl_4$-treatment appears to have little effect on the early-time carrier mobility. Figure 4.2 shows the effective mobility extracted from un-dyed TiO_2 films treated with $TiCl_4$ after excitation at 400 nm. Values of $\phi_{\text{inj}}\mu_{\text{peak}}$ $\sim$0.06 cm^2/Vs are observed, similar to those for samples without $TiCl_4$ treatment. In addition, the effective mobility was again determined for excitation of dyed samples across the absorption spectrum of the dye, as shown in Figure 4.5 a) for both $TiCl_4$-treated and untreated films. There is no discernable difference between the two samples, suggesting that ϕ_{inj} is also largely unaffected by the $TiCl_4$ treatment. Finally, the effect of the treatment on the photoconductivity decay rate has been examined. Figure 4.4 b) shows identical decay dynamics for samples with and without $TiCl_4$ treatment, while Figure 4.5 b) demonstrates that the extracted decay times are identical for the two cases across the whole dye absorption spectrum. These observations demonstrate that the treatment does not affect carrier trapping at early times (up to a nanosecond), and thus appears to have no significant effect on the density of sub-bandgap states in TiO_2.

While these measurements are unable to yield the cause of the DSC performance enhancement with $TiCl_4$ treatment, they help in eliminating a number of possible scenarios. In particular, it is clear that the $TiCl_4$ treatment has no effect on the pico- to nanosecond charge-injection, decay and mobility dynamics in dye-sensitized TiO_2. These findings suggest that the origin of the increased photocurrents with $TiCl_4$ treatment may be found by investigating more closely the processes occurring on longer time scales (nanosecond to millisecond), such as hole transfer, charge separation and longer time recombination processes [4]. Finally, as a caveat to these findings, it is noted that careful spectroscopic analysis of com-

---

[4] This has recently been confirmed by Marchioro *et al.* [214]

plete devices under working conditions may yield information not attainable by studying dissected components, such as the dye-sensitized TiO_2 probed here.

4.4 Conclusions

Optical-pump terahertz-probe technique has been employed to investigate photoconductivity dynamics in mesoporous TiO_2 films. The intrinsic electron mobility values in films made with either a home-made (EPFL) or a commercial (Dyesol) TiO_2 nanoparticle paste is calculated to be $\sim 0.1\,\mathrm{cm^2/Vs}$. For TiO_2 films sensitized with Z907 dye, biphasic charge injection is observed, with an initial sub-500 fs fast component followed by a slower 70-200 ps rise component. This is followed by a decay in photoconductivity over the first few nanoseconds, which appears to be caused by carrier trapping. In addition, experiments have been done to probe the effect of $TiCl_4$-treatment of sintered TiO_2 in order to identify reasons for improved device performance seen in $TiCl_4$ treated DSCs. Repeated measurements on multiple samples show that the carrier mobility, charge injection efficiency and charge trapping times are not affected by the treatment with $TiCl_4$, and are independent of the photoexcitation wavelength. A thorough understanding of such charge generation and transport mechanisms can help identify the bottlenecks, and hence to design better materials and material-combinations for optimized photovoltaic device performance.

Chapter 5

Electron Dynamics in Mesoporous ZnO, SnO_2, and TiO_2 Films

High-performance dye-sensitized solar cells are usually fabricated using nanostructured TiO_2 as a thin-film electron-collecting material. However, alternative metal oxides are currently being explored that may offer advantages through ease of processing, higher electron mobility or different interface band energetics. This chapter reports a comparative study of electron mobility and injection dynamics in thin films of ZnO, TiO_2 and SnO_2 nanoparticles sensitized with Z907 dye. Time-resolved THz photoconductivity measurements show that for ZnO and SnO_2 nanoporous films, electron injection from the sensitizer has substantial slow components lasting over tens to hundreds of picoseconds, while for TiO_2 the process is predominantly concluded within a few picoseconds. These results correlate well with the overall electron injection efficiencies determined from photovoltaic cells fabricated from identical nanoporous films, suggesting that such slow components limit the overall photocurrent generated by the solar cell. Detailed experiments and analysis lead to the conclusion that these injection dynamics are not substantially influenced by bulk energy level offsets but rather by the local environment of the dye-nanoparticle interface that is governed by dye binding modes and densities of states available for injection, both of which may vary from site to site. In addition, the electron mobility has been extracted from THz conductivity measurements for the three nanoporous metal-oxide films at early time after excitation and compared with the time-averaged, long-range mobility determined for working devices based on identical films. Comparison with established values for single-crystal Hall mobilities of the three materials shows that while electron mobility values for nanoporous TiO_2 films are approaching theoretical maximum values, both early-time, short distance and inter-particle electron mobility in nanoporous ZnO or SnO_2 films offer considerable scope for improvement.

5.1 Introduction

Over the past two decades, dye-sensitized solar cells (DSCs) with the highest performance have generally been those fabricated using TiO_2 nanoporous films as the electron-transporting electrode [11]. However, a significant amount of effort is currently being invested into trying to find alternative metal oxides, such as SnO_2, ZnO, Nb_2O_5 and WO_3[13, 34–37] that may offer additional advantages in terms of device fabrication and characteristics. ZnO and SnO_2 [215–218] are two particularly promising candidates, because the electron mobility in their bulk single-crystal phases is over two orders of magnitude higher than that for TiO_2 [219]. As a result, it should also be possible to achieve higher overall electron mobility in the respective nanostructured films of ZnO and SnO_2, which may in turn minimize interfacial charge recombination losses to oxidized redox species in the electrolyte or solid-state hole transporter, thus improving device performance.

For comparison, the conduction (CB) and valence (VB) band energies of TiO_2, ZnO and SnO_2 [13, 34–36, 220, 221] are illustrated schematically in Figure 5.1 a). The band-gap of ZnO is similar to that of TiO_2 at 3.2 eV, while SnO_2 displays a significantly larger band-gap of 3.8 eV. As a result, SnO_2 is less likely to generate holes in the VB through direct photon absorption and devices based on the material ought to be more robust under UV-illumination than those made from TiO_2 or ZnO. In addition, the CB edge of SnO_2 is about 500 mV more positive than that of TiO_2 thus suggesting that charge injection in SnO_2-based DSCs could be faster than in their TiO_2 counterparts, even though at the cost of lower open-circuit device voltage, V_{OC}.

Despite the apparent advantages of ZnO and SnO_2, photovoltaics cells based on thin nano-structured films incorporating these materials have so far failed to overtake the best TiO_2-based devices in terms of performance. In order to examine the reasons for this discrepancy, a combined study has been conducted correlating the THz conductivity dynamics of dye-sensitized thin films made of sintered pastes of TiO_2, ZnO and SnO_2 nanoparticles, with the properties of photovoltaics cells incorporating identical films.

5.2 Experimental Details

ZnO, TiO_2 and SnO_2 nanoparticle pastes were prepared or procured as detailed in Section 3.1.1. OPTP samples were prepared as described in Section 3.5.7, yielding films with thick-

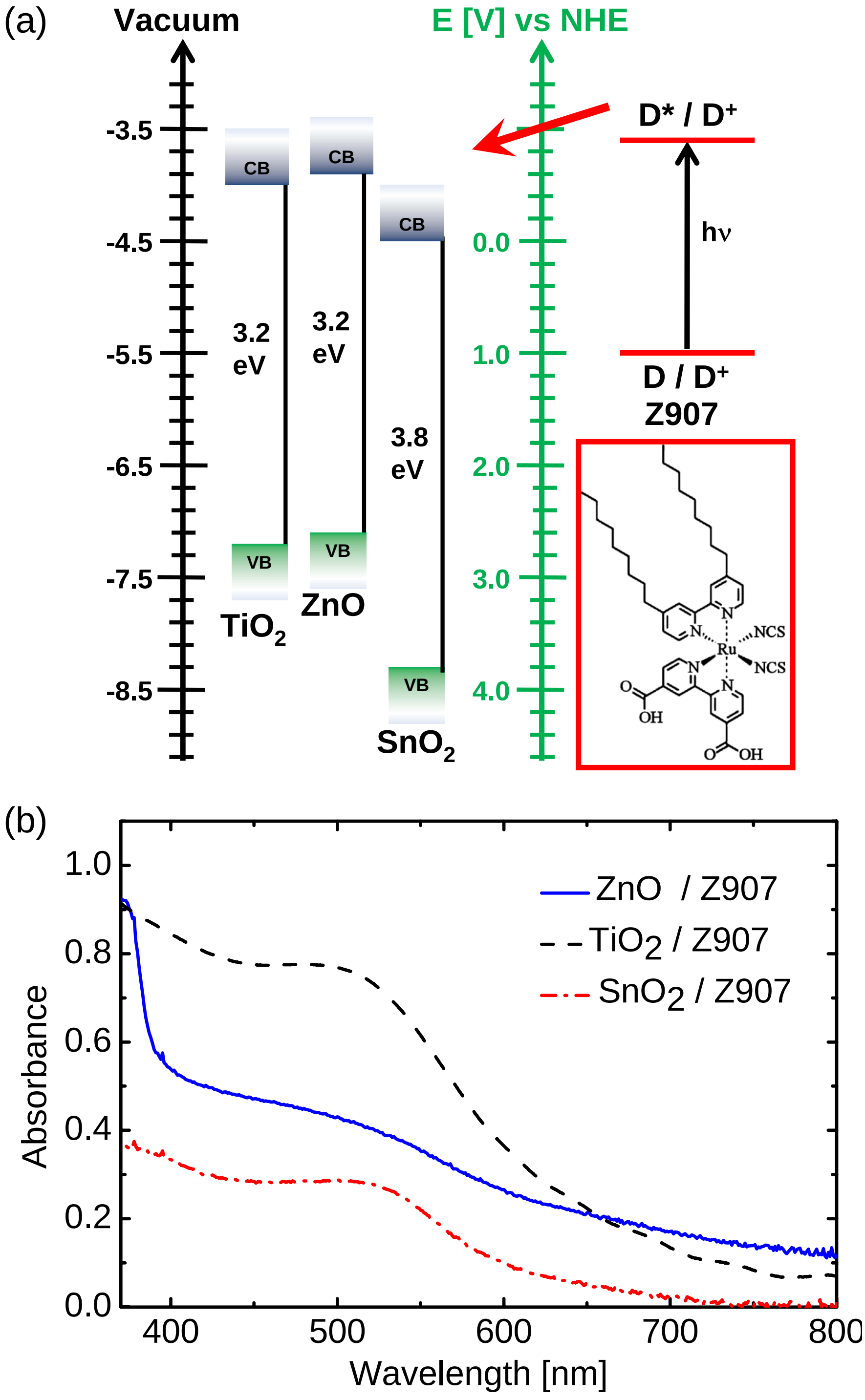

Figure 5.1: a) Schematic diagram illustrating the energy levels of the conduction band (CB) and valence band (VB) of TiO_2, ZnO and SnO_2 as taken from Ref 13, 34–36. Also shown is the approximate redox potential of ground and excited states of Z907 ruthenium-based dye [27] (molecular structure shown in inset). The red arrow indicates electron injection from the dye LUMO states into the respective metal-oxide CB. b) Steady-state absorption spectra measured for sensitized nanoporous films of ZnO (blue solid line, film thickness 0.6μm), SnO_2 (red dash-dot line, film thickness 1μm) and TiO_2 (black dashed line, film thickness 3μm) using an integrating sphere. Spectra were taken for film samples used in the THz photoconductivity measurements and these data were used to calculate the THz effective mobility $\phi_{\mathrm{inj}}\mu_{\mathrm{THz}}$. The films used for the solar cells are much thicker and therefore display a higher optical density (OD>2) at the absorption maximum.

nesses of $0.6\,\mu$m for ZnO, $3\,\mu$m for TiO_2, and $1\,\mu$m for SnO_2 films, as measured with a Veeco DekTak 150 surface profiler. Dye-sensitization was done with Z907 dye as described in Section 3.1.2. Typical steady-state absorption spectra measured using the equipment and protocol described in Section 3.4 are shown in Figure 5.1 b).

The OPTP experimental set-up and data-analysis methodology have been described in detail in Section 3.5.5. Dye-sensitized films were photoexcited at 550 nm (ZnO and SnO_2) or 475 nm (TiO_2) and the change in sample photoconductivity was measured as a function of probe delay. This has been used to quantify the electron injection rate and the peak early-time carrier mobility in the different mesoporous films.

Liquid electrolyte devices were fabricated using the recipe outlined in Section 3.1.5. The nanoparticle pastes were screen-printed on the FTO substrates, resulting in $\geq 7\,\mu$m thick films. Z907 dye adsorption resulted in optical densities (OD) at peak absorption of OD>2. ‘Robust’ (0.8 M PMII, 0.15 M iodine, 0.1 M GuNCS, and 0.5 M NMBI in 3-methoxypropionitrile) was used as electrolyte.

The current-voltage measurement set-up is described in detail in Section 3.2.1. The spectral response, IPCE, was measured under ∼0.01 Sun illumination, as outlined in Section 3.2.2, and is then corrected by integrating the measured spectra over the 1 Sun AM1.5G solar spectrum, such that the integrated short-circuit photocurrent is in close agreement with the maximum photocurrent value measured in the JV curves under simulated standard solar conditions. Transient photovoltage and photocurrent decay experiments were carried out under short-circuit conditions as described in Section 3.3. The charge transport and recombination rates measured in these experiments are used to determine the charge collection efficiency, η_{coll}, electron diffusion coefficient and the device mobility, discussed in more detail later.

5.3 Results and Discussion

5.3.1 Charge injection dynamics in ZnO, TiO_2 and SnO_2

Figure 5.2 shows the OPTP normalized conductivity curves for the three dye-sensitized metal-oxides nanoporous films as a function of time after excitation of the Z907 dye. All three metal oxide materials have sufficiently large band gaps (see Figure 5.1) in order for the 550 and 475 nm excitation pulses to generate excitations almost solely on the dye sensitizers, see Figure 4.1. The measured photo-conductivity signal originates from mobile electrons subsequently injected into the metal oxide films, since in comparison the remaining holes on the dye molecules are essentially stationary. Such measurements allow both an investigation of the dynamics of the conductivity, and the initial electron mobility achieved in the material. The first half of this chapter focuses on analysing the electron injection dynamics, followed by an in-depth examination of the THz mobility in comparison to bulk and device mobilities.

Multiphasic electron injection dynamics are displayed by all three metal oxide films, with an initial fast injection component followed by slow rise phases, albeit with different weightings. In order to quantify the components contributing to the conductivity dynamics of electrons in the CBs or the metal oxides the curves have been fitted with a sum of three exponentials, as displayed in Figure 5.2 together with the data. Table 5.1 shows the time constants and weightings extracted from these fits. Remarkably, all three systems display a fast component with rise time $\sim$1 ps followed by a slower electron injection phase with time constants of a few tens of picoseconds. Overall, electron injection from Z907 into TiO_2 evidently proceeds fastest, followed by that into SnO_2 while ZnO shows the slowest overall injection rate.

Multiphasic charge injection involving slow delayed components has been previously reported for dye-sensitized ZnO [35, 36, 74, 75, 83, 222], TiO_2 [71, 76, 77, 79, 107, 223] and SnO_2 [35, 36, 72, 82, 85, 107] studied by various experimental techniques such as ultrafast transient absorption spectroscopy [83, 222], mid-IR probe [35, 74, 75], and microwave [36] or THz [107, 223] conductivity measurements. However, absolute rise times reported even

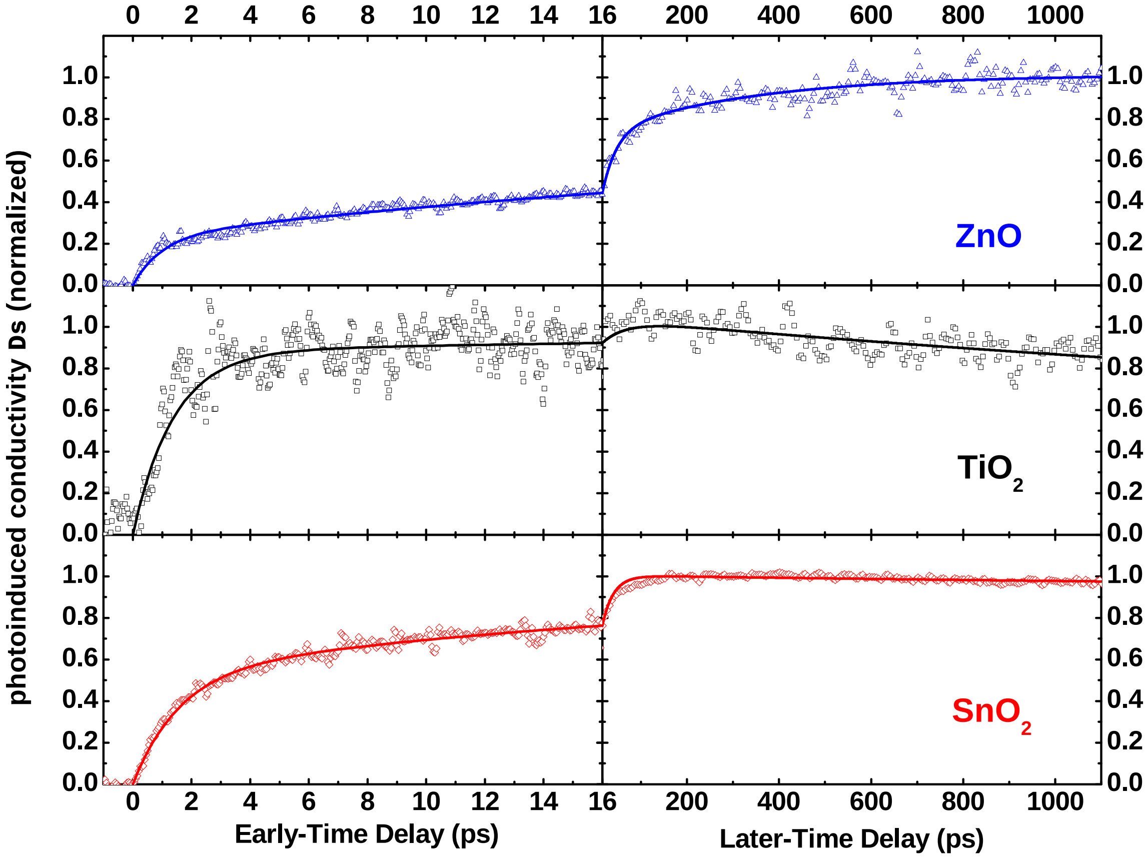

Figure 5.2: Early and later-time photoconductivity dynamics in nanoporous ZnO, TiO_2 and SnO_2 films sensitized with Z907 dye. Early-time trends (up to 16 ps) are shown on the left and later-time trends (up to 1.1 ns) on the right. Dye-sensitized ZnO and SnO_2 were photoexcited at 550 nm, while TiO_2 was excited at 475 nm. Identical dynamics were observed for TiO_2/Z907 when the excitation wavelength was varied across the dye absorption spectrum between 475–700nm and a linear dependence of the photoconductivity on excitation fluence was found at these excitation densities. In all three cases, incident photoexcitation fluence was $\sim 3\times 10^{14}$ photons/cm^2, with pulse duration ~40 fs. The curves have been normalized at the respective maxima measured for each material. Solid lines are the result of fitting the sum of three exponentials to the data, with the extracted parameters given in Table 5.1.

	τ_1 (ps)	τ_2 (ps)	τ_3 (ps)	A_1	A_2	A_3
ZnO	1.0±0.1	31±2	335±42	-0.232±0.006	-0.49±0.02	-0.29±0.02
TiO_2	1.4±0.1	51±25	3000 (set)	-0.88±0.02	-0.16±0.02	0.61±0.09
SnO_2	1.6±0.1	24±1	3000 (set)	-0.538±0.008	-0.47±0.01	0.10±0.02

Table 5.1: Parameters extracted from exponential fits to the time-dependent photoconductivity data on sensitized nanoporous films of ZnO, TiO_2 and SnO_2. A fitting function of $\Delta\sigma = \sum_{i=1}^{3}(A_i \exp(-t/\tau_i) - A_i)$ was used and the resulting curves are shown in Figure 5.2 together with the data. Negative amplitudes A_i reflect rise components while positive ones correspond to intensity decay.

for the same metal oxide material vary substantially between the different studies. These discrepancies should not be surprising since these studies involved films made with nanoparticles of varying shapes and sizes, with varying recipes, sensitized with different ruthenium dyes and with different surface conditions. As demonstrated by Ai *et al.* [85], different film environments can change the flatband potential of the semiconductor and the reorganization energy which affects the injection rate as a result of its dependence on the interfacial proton concentration. In this experimental study, effort has been made to minimize such effects by preparing films in a comparable manner, sensitizing them with an identical and commonly used dye (Z907), and measuring THz and photovoltaic dynamics under the same conditions.

The relative rates of electron injection observed for the three different oxides (Figure 5.2) are surprising at first: for ZnO, injection is slower than in TiO_2 even though both metal oxides have almost identical interface band energetics (Figure 5.1). SnO_2 exhibits somewhat slower electron injection than TiO_2 even though the CB edge of SnO_2 is more positive by $\sim$500 meV compared to TiO_2, which should increase the number of the SnO_2 acceptor states at the dye excited-state energy. There are, however, a number of other factors contributing to the electron transfer kinetics at the dye/metal oxide interface. One possibility is that different amounts of dye loading for the three materials may result in slow charge injection caused by the presence of dye agglomerates on the metal-oxide film, as proposed previously [77, 224]. However, Anderson *et al.* used detailed experimental pump-probe studies carried out on ZnO/N3 and ZnO/N719 to show that although excess dye-loading can lead to reduced overall injection yield, it does not affect the ultrafast injection rate [74, 75]. Similarly, repeated experiments conducted for the work reported in Chapter 4 show that the slow injection component in mesoporous TiO_2 sensitized with Z907 is unaffected by moderate changes in dye loading. Given the standard optical densities for dye absorption for these samples (Figure 5.1 b), it is, therefore, assumed that changes in dye loading are not the cause of the observed slow injection phases. As an alternative explanation, multiphasic electron injection into TiO_2 [71, 76] and SnO_2 [72] has been attributed to different injection speeds from the singlet and triplet excited states of the dye's ruthenium complex with the femtosecond component arising from the initially excited singlet state (^{1}MLCT), and the picosecond part from the thermalized triplet ^{3}MLCT excited state. However, since the same dye is used as sensitizer for all metal oxides, this mechanism alone cannot explain the differences in injection speeds between the three metal oxide films.

A likely scenario is that electron injection between the three oxides is influenced by the electronic structure of the CB of the metal oxide and the coupling of the dye molecule to the interface. The CB structure of the metal oxides investigated differs drastically between TiO_2 on the one hand and ZnO and SnO_2 on the other hand. The effective mass of CB electrons in TiO_2 is about 5–10 $\mathrm{m_e}$ as opposed to a corresponding value of $\sim$0.3 $\mathrm{m_e}$ for ZnO and SnO_2 [85, 225, 226]. Therefore, the available density of states (DoS) is almost two orders of magnitude higher in TiO_2 than in ZnO or SnO_2 [35, 75, 85, 225] which should facilitate faster injection into TiO_2. An additional prerequisite for efficient electron injection is that there has to be significant extension of the dye excited state wavefunction into the metal oxide. The electron-donating π^* orbital of the carboxylated bipyridine unit on Z907 has a stronger overlap with the electron-accepting d orbitals of Ti^{4+} than with the 4s orbital of Zn^{2+} [35, 75, 227]. Similarly, for SnO_2 a weaker electronic overlap at the interface with N3 or N719 dyes has been suggested [82, 85] which is consistent with the slower injection seen in Figure 5.2.

As an alternative explanation, Furube *et al.* suggested that the presence of intermediate charge transfer complexes may cause slow electron injection dynamics from sensitizers into metal oxide films [83, 222]. For ZnO nanoporous films sensitized with N3 dye, they observed that the fast (sub-picosecond) generation of N3 cations following photo-excitation was not matched by the rise of the free-electron signal from ZnO, which occurred on the time scale of ∼150 ps [83]. They concluded that electron transfer from N3 to ZnO occurred via a two-step process involving an intermediate state between the photoexcited dye and a surface state in ZnO (details in Appendix A.3). For nanoporous TiO_2 sensitized with N3, on the other hand, fast electron injection was observed suggesting that intermediate states do not play a strong role here. These measurements were corroborated later for the same systems by Neměc *et al.*, who proposed that the slow injection was the direct result of the higher static dielectric constant of TiO_2 (∼100) compared to that of ZnO (∼10), as in the former such electron-cation complex interactions may be efficiently screened [100]. The current study shows slow injection dynamics for both ZnO and SnO_2, both of which have similar low static dielectric constants [228]. However, the presence of multiple rise times for all three metal oxides investigated suggests that such screening effects alone cannot be the explanation for the slow injection dynamics. All three metal-oxide systems have a fast picosecond injection component suggesting that for all of them, fast injection pathways are available from certain sites. These findings are in agreement with further studies by Furube *et al.* [222] on nanoporous ZnO sensitized with a coumarin dye and Ai *et al.* [85] on nanoporous SnO_2 sensitized with various ruthenium dyes, for which the authors observed multi-phasic electron injection into the metal oxide with different time constants ranging from a picosecond to tens of picoseconds. To summarize these arguments, electron injection from most dye/metal oxide systems appears to be influenced by site disorder with injection pathways and dynamics being governed by the local interface environment which may vary considerably between each dye/metal oxide site. The particular mode of coupling of the dye to the surface and the local electronic density of states in the CB of the metal oxide have a strong influence on electron injection dynamics, with pure energy level offsets and bulk dielectric constant playing only a secondary role.

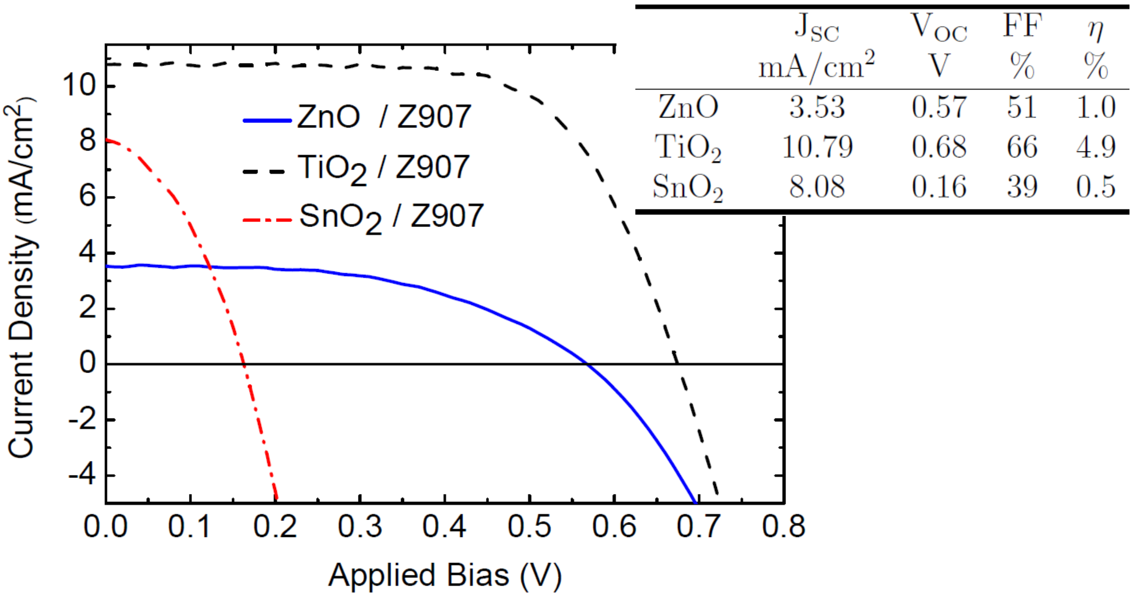

	J_{SC} mA/cm^2	V_{OC} V	FF %	η %
ZnO	3.53	0.57	51	1.0
TiO_2	10.79	0.68	66	4.9
SnO_2	8.08	0.16	39	0.5

Figure 5.3: Current-voltage characteristics under simulated solar conditions measured for three typical liquid-electrolyte photovoltaic cells fabricated from either TiO_2, ZnO or SnO_2 nanoporous films sensitized with Z907 dye. IPCE and transient photovoltage and photocurrent measurements were performed on the same devices to calculate the data summarized in Table 5.2

5.3.2 Carrier mobilities in ZnO, TiO_2 and SnO_2

Another relevant piece of information that can be extracted from OPTP measurements is the "effective THz mobility" $\phi_{\mathrm{inj}}\mu_{\mathrm{THz}}$ of electrons within the nanoporous semiconductor film, which was introduced in Section 4.3.1 Eqn 4.1. Here, ϕ_{inj} is the charge injection efficiency per absorbed photon and μ_{THz} the peak value of the film's time-dependent THz mobility. Being independent of sample geometry and excitation fluence, carrier mobility is a more useful material characteristic than conductivity. Using the respective measured peak photoconductivity values, incident excitation fluences, and steady-state absorption at the excitation wavelength (data shown in Figure 5.1 b), $\phi_{\mathrm{inj}}\mu_{\mathrm{THz}}$ is determined to be $0.08\pm0.01\,\mathrm{cm}^2/\mathrm{Vs}$ for nanostructured ZnO, $0.1\pm0.03\,\mathrm{cm}^2/\mathrm{Vs}$ for TiO_2 and $0.8\pm0.14\,\mathrm{cm}^2/\mathrm{Vs}$ for SnO_2.

In order to extract the actual mobility μ_{THz} from these values, ϕ_{inj} is first determined from measurements on liquid-electrolyte DSCs based on the three metal-oxides films. Figure

5.3 shows the JV curves measured for three typical devices. As expected, solar cells based on SnO_2 show a markedly lower open circuit voltage than those based on TiO_2 or ZnO [148, 229] predominantly as a result of the differing CB levels. However, recombination losses at open circuit also contribute to the lowering of the open-circuit voltage for bare SnO_2. IPCE measurements of these devices are related to the charge injection efficiency, ϕ_{inj} through:

$$\mathrm{IPCE} = \mathrm{LHE} \times \phi_{\mathrm{inj}} \times \eta_{\mathrm{coll}} \tag{5.1}$$

LHE is the light harvesting efficiency of the device, or in other words, the fraction of incident photons successfully absorbed within the active layers in the DSC. Since all mesoporous layers (ZnO, TiO_2 and SnO_2) in the devices were thick enough ($\geq 7\,\mu$m) to be fully absorbing, the main losses were due to reflection and absorption in the light-facing FTO glass. These are measured to be 12.3% and 3.6% respectively at 550 nm, as shown in Figure 3.11. LHE is thus determined to be 84% for all three sets of devices. The charge collection efficiency, η_{coll}, is calculated using Eqn 3.11, based on the small perturbation transient photovoltage and photocurrent decay measurements. The measured IPCE and η_{coll} values for the three types of devices are listed in Table 5.2.

The average ϕ_{inj} values, deduced from Eqn 5.1, are also listed in the table. For the case of TiO_2/Z907, a charge injection efficiency of 100% indicates that this dye-semiconductor system is highly optimized, in comparison to the other two materials. Interestingly, ZnO performs worse (ϕ_{inj}=0.47) than SnO_2 (ϕ_{inj}=0.79) in agreement with the delayed charge injection components shown in Figure 5.2. This combination of OPTP with device measurements suggests that the more pronounced a slow component is in the electron injection dynamics for the metal oxide films, the lower the overall charge injection efficiency of the solar cell will be. Better matched dyes thus need to be designed specifically for ZnO and SnO_2 that allow near-unity charge injection from the dye at rates significantly faster than the dye's excited-state lifetime. It is important to note that the charge collection efficiency at short circuit for devices fabricated from all three oxides is higher than 0.95, consistent with the change in the injection efficiency being the performance-limiting factor.

	THz Effective Mobility[a]	IPCE (max)[b]	Photocurrent decay rate[c]	Photovoltage Decay Rate[c]	Collection Efficiency	Injection Efficiency[d]	**THz Mobility[e]**	**Bulk Mobility** [215, 216, 219]	Device Diffusion Coefficient	**Device Mobility[e]**	Static Dielectric Constant [228]
	$\phi_{\mathrm{inj}}\mu_{\mathrm{THz}}$ $\mathrm{cm^2/Vs}$	IPCE	k_{signal} $\mathrm{s^{-1}}$	k_{rec} $\mathrm{s^{-1}}$	η_{coll}	ϕ_{inj}	μ_{THz} $\mathrm{cm^2/Vs}$	μ_{bulk} $\mathrm{cm^2/Vs}$	D_e $\mathrm{cm^2/s}$	$\mu_{\mathrm{N-E}}$ $\mathrm{cm^2/Vs}$	ϵ_{rs} $\parallel, \perp$
ZnO	0.08	0.38	571.9	24.6	0.96	0.47	**0.17**	**200**	1.1E-4	**0.004**	$8, 12$
TiO_2	0.1	0.83	1040	20.4	0.98	1.00	**0.10**	**1**	4.3E-4	**0.017**	$173, 89$
SnO_2	0.8	0.63	368.2	19.6	0.95	0.79	**1.01**	**250**	7.3E-5	**0.003**	$9.9, 14$

Table 5.2: Charge injection and mobility parameters determined for nanoporous dye-sensitized ZnO, TiO_2 and SnO_2 films together with literature values for some bulk properties. Detailed references to each parameter are given in the main text. [a] $\phi_{\mathrm{inj}}\mu_{\mathrm{THz}}$ was taken from OPTP measurements of the highest $\Delta\sigma$ value, see Section 4.3.1 for details. [b] Peak spectral response in optically thick liquid-electrolyte DSCs. [c] Measurements were taken under short-circuit conditions and decay curves fitted with mono-exponential functions to extract rates shown. [d] ϕ_{inj} was estimated using Eq. 5.1 with light absorption within DSCs estimated to be 0.84 with deviation from unity caused by losses through absorption and reflection from FTO glass. [e] Values were determined within an experimental error of ∼25%.

It should also be noted that the overall device performance seen in Figure 5.3 is worst in case of SnO_2, despite faster charge injection and good charge collection as shown above. This poor device efficiency is due to the extremely low V_{OC} of only 0.16 V. This is justified by the large energy difference between Z907 dye LUMO state and SnO_2 CB, shown schematically in Figure 5.1. SnO_2-based DSCs with higher V_{OC}, and hence higher device efficiency, can be achieved by employing a sensitizer dye with lower LUMO energy level and by coating the SnO_2 nanoparticles with a wide bandgap material such as MgO or Al_2O_3 [38, 148, 229–232]. The latter technique is described in further detail in Sections 6.1 and 6.3.5.

These ϕ_{inj} values are now used to extract the THz peak mobility μ_{THz} of the films as $0.17\pm0.04\,\mathrm{cm^2/(Vs)}$ for ZnO, $0.10\pm0.03\,\mathrm{cm^2/(Vs)}$ for TiO_2, and $1.01\pm0.20\,\mathrm{cm^2/(Vs)}$ for SnO_2. It should be stressed that these results reflect the THz conductivity conditions within the first nanosecond after electron injection into the metal-oxide films, while in the longer term the conductivity is likely to be lowered by charge trapping and surface scattering events [105].

5.3.3 Comparison between μ_{THz}, μ_{NE}, and μ_{bulk}

It is useful to compare μ_{THz} with the electron mobility obtained for liquid electrolyte DSC devices incorporating the nanoporous films. The device mobility is estimated using the Nernst-Einstein relation [33]:

$$\mu_{\mathrm{NE}} = \frac{\mathrm{eD_e}}{\mathrm{k_B T}} \quad \text{and} \quad \mathrm{D_e} = \frac{\mathrm{d^2\,k_{trans}}}{2.35} \tag{5.2}$$

where $\mathrm{D_e}$ is the effective electron diffusion coefficient (shown in Table 5.2) and d is the film thickness. The charge transport rate, $\mathrm{k_{trans}}$, is calculated from the transient photovoltage and photocurrent measurements at short-circuit as $\mathrm{k_{trans}} = \mathrm{k_{signal}}$ - $\mathrm{k_{rec}}$, both of which are listed in Table 5.2 (experimental details in Section 3.3). It is useful to note that the same relationship was invoked in the previous chapter in Eqn 4.2 to estimate that the electron diffusion coefficient based on μ_{THz} is $\sim 2.5\times10^{-3}\,\mathrm{cm^2/s}$. Here, on the other hand, the relationship is used to calculate D_e and mobility for the complete working device for long-distance transport - both values are, therefore, lower than the early-time values by an order of magnitude.

A third measure of mobility against which these results may be compared are the values determined by others for bulk single crystals of the three metals oxides. In single crystals surface scattering and trapping are likely to be minimised and the electron mobility determined can therefore be seen as an upper limit of what may be achieved in the nanoporous film. Table 5.2 lists bulk mobility values (μ_{bulk}) found in the literature for room-temperature Hall measurements on single crystals of ZnO [215], TiO_2 [219], and SnO_2 [216], together with those extracted from THz (μ_{THz}) and device (μ_{NE}) measurements.

A number of interesting observations can be made by comparing these three measures of electron mobility for the three different metal oxides. First, a comparison between μ_{THz} and μ_{bulk} reveals that, while for TiO_2 the THz mobility is within an order of magnitude of the bulk mobility value, for ZnO and SnO_2 this discrepancy widens to 2–3 orders of magnitude. Hendry *et al.* previously measured an early-time THz charge mobility for un-sensitized porous TiO_2 films of $10^{-2}\mathrm{cm}^2/(\mathrm{Vs})$, i.e. two orders of magnitude below the bulk crystal mobility [105]. They attributed this discrepancy to the nanoporous nature of the films in which dipoles induced in the TiO_2 particles with high dielectric constant screen the applied electric field, thus resulting in the flux density to be higher in the medium surrounding the particle than within. As a consequence the mobility of the nanoporous TiO_2 film is likely to be intrinsically lower than that of bulk, by a factor which may be approximated from Maxwell-Garnett (MG) theory [105]. The THz mobility value for nanoporous TiO_2 calculated here is one order of magnitude higher than that found by Hendry *et al.* This may be a consequence of the nanoparticles examined in this study being embedded in a medium of higher dielectric constant (the sensitizer) and perhaps different fabrication protocols. It is therefore concluded that for sensitized nanoporous TiO_2 films a slight (factor $\sim$0.1) reduction of the achievable mobility below that of single crystals may have to be accepted as a result of MG effects. However, for ZnO and SnO_2 this situation is markedly different: Table 5.2

lists values for the static dielectric constant ϵ_{rs}, which approximate those at THz frequencies, for the three different metal oxides as found in Ref. 228. For ZnO and SnO_2, the dielectric constant is over an order of magnitude lower than that for TiO_2, and therefore MG effects are likely to be much less significant for these two metal oxide nanoporous materials. Given that for TiO_2, MG effects lead to a mobility reduction of at most a factor 0.1, these effects are likely to be insignificant for ZnO and SnO_2. The observed THz mobility reduction for ZnO and SnO_2 nanoporous films of over two orders of magnitude below the corresponding single-crystal electron mobilities is therefore surprising and points towards electron mobilities on the nanometer scale that are significantly below what should in theory be achievable.

A second useful comparison to make is between the electron mobility found in complete devices and that found in bulk crystals. The values given in Figure 5.2 show that there is little positive correlation between μ_{NE} and μ_{bulk}; in fact, TiO_2 exhibits the highest device mobility ($0.017\,\mathrm{cm^2V^{-1}s^{-1}}$) but lowest bulk crystal mobility ($1\,\mathrm{cm^2V^{-1}s^{-1}}$) while SnO_2 gives lowest device mobility ($0.003\,\mathrm{cm^2V^{-1}s^{-1}}$) at highest bulk crystal mobility ($250\,\mathrm{cm^2V^{-1}s^{-1}}$). The electron mobility measured for the nanoporous thin-film devices (μ_{NE}) reflects the time-averaged mobility throughout the film and is therefore significantly affected by *inter-particle* transfer, surface scattering and trapping. In contrast, the THz mobility (μ_{THz}) indicates conditions within the first nanosecond after electron injection into the metal-oxide films and thus reflects *intra-particle* transfer, and is strongly affected by short-distance electron transport and scattering. While ZnO and SnO_2 exhibit bulk crystal mobilities over two orders of magnitudes higher than that for TiO_2, the early-time, short-distance THz mobilities are similar for the three metal oxide nanoporous films, and the corresponding device mobilities are almost an order of magnitude lower for ZnO and SnO_2 than for TiO_2. Taken together, these comparisons show that while TiO_2 nanoporous films are reaching near optimum results for a porous effective medium of high dielectric constant, the standard ZnO and SnO_2 nanoporous films investigated here are still 4–5 orders of magnitude away from what could theoretically be achieved in terms of electron mobility. These findings on ZnO are in agreement with those of Baxter *et al.* showing that a wide variation in THz mobility values can be found for samples fabricated from ZnO films, nanowires, and nanoparticles, with the lowest mobility measured in the nanoparticles [127]. Improving both nano- and micro-meter scale conduction pathways in ZnO and SnO_2 should therefore allow significant advances to be made in photovoltaic device performance.

Even though this study demonstrates that the charge collection efficiency at short-circuit is high for all three oxides, under forward bias working conditions the charge collection efficiency reduces considerably [20] and almost by definition is close to zero at open-circuit. Therefore enhancing the charge transport in the oxide will significantly improve the photocurrent under working conditions and hence the fill factor and efficiency for solar cells based on nanostructured ZnO and SnO_2.

5.4 Conclusion

This chapter reports a comparative study of electron injection and mobility in nanoporous films of three different metal oxides, TiO_2, ZnO and SnO_2 sensitized with Z907 dye. The change in THz conductivity in the metal oxide as a function of time after photoexcitation of the dye is used to examine the dynamics of electron injection from the dye into the metal oxide. There are significant slow injection components lasting predominantly over a few hundred picoseconds after excitation for ZnO, and tens of picoseconds for SnO_2. For TiO_2, on the other hand, such delayed electron injection plays a minor role and mostly features within the first few picoseconds. These results correlate well with the overall electron injection efficiencies determined from photovoltaic cells fabricated from identical nanoporous films of the three oxides. Such slow injection components thus allow effective competition between charge injection and excitonic recombination on the sensitizer and must be overcome for further device efficiency gains. The extent to which slow injection components are present was found to be largely independent on the energetic positioning of the metal oxide conduction and valence bands. It is therefore concluded that other factors such as the density of states for the bands and the local binding and orbital overlap of the sensitizer on the metal oxide surface are more important. The design of dyes that are better matched and attached to the electron acceptor should hence lead to improvements in charge generation efficiencies for ZnO and SnO_2.

In addition, the THz conductivity measurements in combination with transient device photocurrent measurements have been used to determine the electron mobility in the nanoporous metal-oxide films both at early-time after injection (μ_{THz}), and for the time-averaged long-distance motion of electrons through the film (μ_{NE}). Comparison between these results and the established values for Hall-mobility in single-crystal of the three metal oxides (μ_{bulk}) reveals that while ZnO and SnO_2 have μ_{bulk} values 2–3 orders of magnitude higher than that for TiO_2, the values obtained for the early-time μ_{THz} are identical within an order of magnitude for the three metal oxides. Furthermore, device mobility values μ_{NE} for the three different materials show the reverse trend from those for μ_{bulk}: here, TiO_2 yields μ_{NE} significantly higher than those obtained for either ZnO or SnO_2 nanoporous films. These results show that both the early-time, short distance and the inter-particle electron motion in ZnO or SnO_2 are far from optimized. To conclude, while electron mobility values for devices incorporating TiO_2 nanoporous films are now approaching optimum theoretical values, those for ZnO or SnO_2 still offer room for improvement of several orders of magnitude.

Chapter 6

Improved Device Performance in SnO_2 SDSCs with Exposure to Light

An extremely strong “light-soaking” effect has been observed in SnO_2 based solid-state dye-sensitized solar cells (SDSCs). As measured under AM1.5G sun light, white LED illumination with no UV component, and red LED illumination, the device short-circuit photocurrent and efficiency increase significantly over 20–30 minutes, until steady-state is achieved. Transient photovoltage and photocurrent measurements show that while the electron transport rate does increase with light-soaking, there is also an accompanying increase in the recombination rate. The overall result is that the charge collection efficiency gets slightly poorer as the exposure to light increases, clearly not accounting for the increase in photocurrent. To probe the initial electron injection into dye sensitized SnO2, optical-pump terahertz-probe (OPTP) spectroscopy experiments have been employed. A monotonic speeding up of electron transfer from the photoexcited dye into the semiconductor is observed, accompanied with a rise in the overall photoconductivity signal at 1 ns, as a function of the measurement time, where the exposure is due to the pulse train at 550 nm wavelength. This can be explained by a positive shift in the conduction band edge, or an increase in the density of states (DoS) below the band edge induced by continued exposure to light. To check this hypothesis, capacitance measurements have been conducted on SnO_2 SDSCs illuminated with red light (no UV) which show an increase in DoS as a result of light soaking. The increased availability of states into which electrons can be transferred justifies the increase in both the charge injection rate, and ensuing photocurrent, and is also corroborated by a slight drop in cell open-circuit voltage. The cause for the shift in surface potential or increase in density of states is not clear, but is likely to be due to the photoinduced charging of the SnO_2 inducing a rearrangement of charged species or loss of surface oxygen at the dye-sensitized heterojunction.

6.1 Introduction

TiO_2 is the most commonly employed oxide in dye-sensitized solar cells and represents the highest efficiency electrode employed to date. However, in many respects the electronic properties of SnO_2 should be superior and as such it has raised a lot of interest in the dye-sensitized solar cell community [38, 148, 229]. The main drivers for employing SnO_2 are its high band-gap resulting in low photocatalytic activity, which should lead to increased device stability (though not proven to date) and that the bulk mobility of SnO_2 is almost 2 orders of magnitude higher than that of TiO_2 [216, 219]. There is hence potential for fabricating mesoporous SnO_2 films with high mobility which result in significantly higher charge collection efficiency under working conditions, and reduced series resistance losses which should result in improved fill factors and efficiency [38, 88, 148]. Additionally, the SnO_2 conduction band (CB) edge is about 500 mV more positive than that of TiO_2 as shown in Figure 5.1, which implies that SnO_2 should be more suitable for use with very narrow band-gap sensitizers, opening prospects for tandem DSCs.

Despite all these potential advantages of SnO_2, various research groups have shown that the performance of "bare" SnO_2-based solar cells is not very high and is limited by both poor short-circuit current (J_{SC}) and open-circuit voltage (V_{OC}) due to severe recombination losses. A popular solution to the problem is to apply a conformal coating of a high band-gap material such as MgO, Al_2O_3, ZrO_2, TiO_2, etc. on the SnO_2 nanoparticles [38, 148, 229–232]. This treatment results in a drastic improvement in device efficiency by primarily enhancing the V_{OC}, and also the J_{SC} to some extent, both in liquid-electrolyte [38, 229–232] and solid-state DSCs [148, 233]. Recently Snaith *et al.* showed that for solid-state DSCs (SDSCs) there is almost a 3–5 fold reduction in recombination rate when the SnO_2 nanoparticles have a sub nm shell of MgO around them, and further still with a shell of TiO_2 [148]. However, for SDSCs it is also important to prevent direct contact of the top metallic electrode with the mesoporous SnO_2, since this can result in a shunting path which inhibits open-circuit voltage and photocurrent [234].

While conducting OPTP measurements for the work reported in Chapter 5, an interesting "light-soaking" phenomenon was observed in the SnO_2 films sensitized with Z907 dye and photoexcited at 550 nm. Both the electron injection rate and the overall photoconductivity signal were observed to increase with exposure time until a "steady-state" was achieved. This correlated with similar observations made on SnO_2-based SDSCs employing spiro-OMeTAD as the hole-transporter, whereby a significant improvement in short-circuit photocurrent was observed as a function of the exposure time to sunlight (simulated by solar simulator or LEDs). Generally the devices are light-soaked for up to 20 minutes before a stabilized photocurrent is recorded. The OPTP measurements suggest that light-soaking enhances photoinduced electron injection and transfer, but notably, without the requirement for any direct light absorption in the metal oxide. This hypothesis is contradictory to the usual interpretation of UV induced light soaking effects in TiO_2 based DSCs [235–238] and has been explored in detail in this chapter. It is worth mentioning here that the photoconductivity trend in SnO_2/Z907 shown in Figure 5.2 was achieved after the above-mentioned steady-state had been reached.

6.2 Experimental Details

Solid-state DSCs were fabricated as described in Section 3.1.6. SnO_2 paste procured from EPFL, prepared as described in Section 3.1.1, was applied on the FTO sheets using blade-coating and sintered at 500°C, yielding 1.8 μm thick films. Some of the films were coated with a thin MgO layer by immersing the substrates in 20 mM magnesium acetate in a boiling ethanol bath maintained at 100°C for exactly 1 minute. After removing the substrates from the bath, they were allowed to drip-dry and then rinsed in ethanol. After drying the substrates again, they were kept on a hot-plate at 100°C for 10 minutes. The temperature was then increased to 500°C. After 45 minutes at 500°C, they were allowed to cool down naturally to 70°C. The SnO_2 films were then dye-sensitized with an indolene dye termed D102 for 1 hour (molecular structure in Figure 3.1). Following this, spiro-OMeTAD dissolved in chlorobenzene, with added *t*BP and Li-TFSI salts, was spin-coated on the substrates. Finally, 150 nm thick silver electrodes were evaporated over the HTM layer to complete the devices.

JV measurements were conducted as described in Section 3.2.1. Transient photovoltage and photocurrent decay experiments were carried out under short-circuit conditions as described in Section 3.3. All decay curves were fitted with monoexponentials to estimate the recombination and transport rates. Based on these measurements, the charge collection efficiency and the chemical capacitance of the device were estimated (Eqns 3.11 and 3.13, respectively).

The OPTP experimental set-up and data-analysis methodology have been described in detail in Section 3.5.5. 1-D pump scans were conducted on 1 μm thick transparent films on z-cut quartz substrates prepared using the EPFL SnO_2 paste, as outlined in Section 3.5.7. Some of these films were given a conformal MgO coating as described above. Dye sensitization was done by soaking the samples in Z907 dye for about 14 hours at room temperature. All THz samples were stored in the dark in a nitrogen atmosphere when not being measured in the OPTP set-up.

6.3 Results and Discussion

6.3.1 JV measurements

Current voltage measurements discussed here have been conducted on SDSCs fabricated from mesoporous SnO_2 coated with a thin shell of MgO and sensitized with D102 dye. Snaith *et al.* have previously demonstrated that this specific system can generate charge very efficiently, with an estimated absorbed photon-to-electron conversion efficiency (APCE) of close to unity [148]. However, to obtain optimum performance of these devices, they are required to be exposed to light, or "light soaked", for up to 20 minutes. This is illustrated in Figure 6.1 a), showing typical current-voltage curves measured after exposing MgO-treated SnO_2-based SDSC devices to simulated sun light over a period of 18 minutes[4]. A steady improvement in both J_{SC} and device efficiency is observed over a period of about 20–30 minutes till steady-state is achieved, as shown in Figure 6.1 b). The fill-factor (FF) improves marginally while a slight decrease in V_{OC} is observed over this measurement time, as seen in Figure 6.1 c).

---

[4] All SDSC devices discussed in this chapter were fabricated by Dr. Henry Snaith

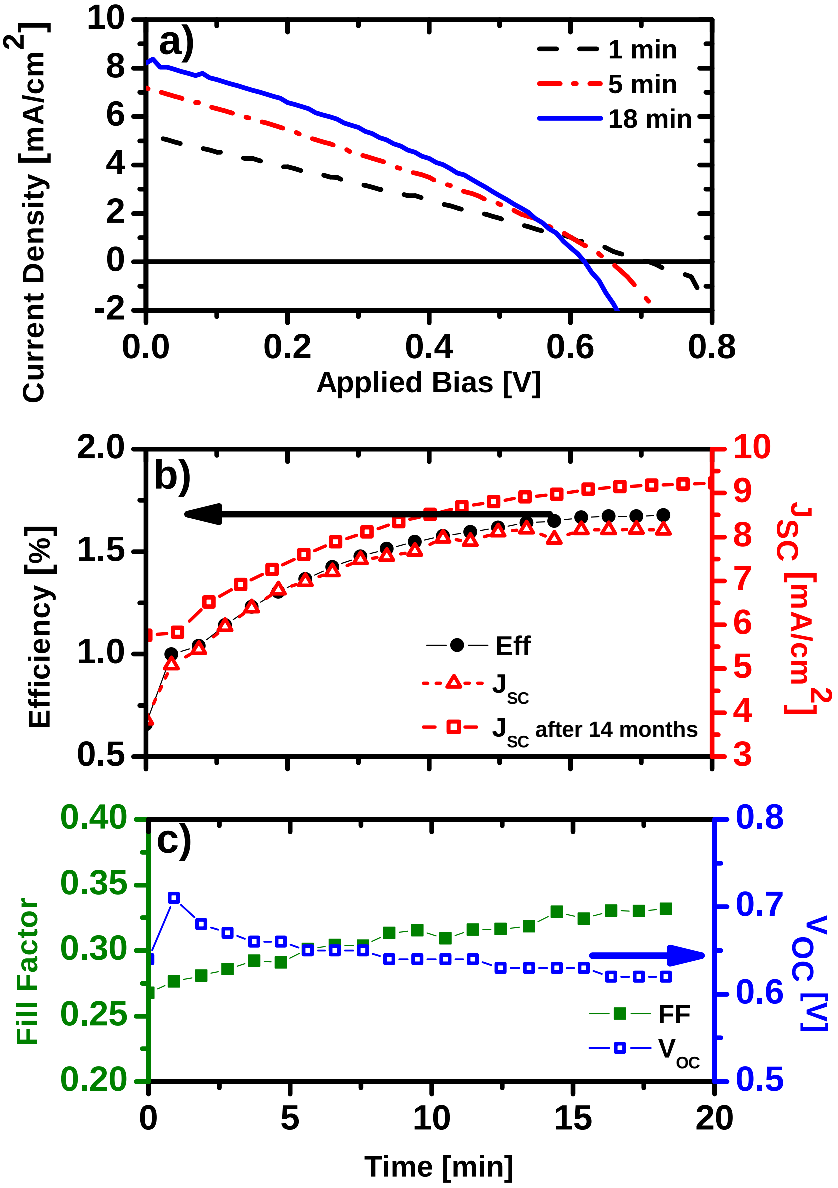

Figure 6.1: Typical current-voltage (JV) measurements for solid-state DSCs incorporating MgO-treated SnO_2 sensitized with D102 dye a) JV curves measured at different times after exposure to simulated AM1.5G sunlight at 100 mW/cm^2 equivalent intensity b) Device efficiency and J_{SC} show a steady increase over 20–30 minutes until steady state is achieved. The short-circuit current evolution was remeasured after 14 months on a similar device, measured under a white LED array where no UV light was present, as shown by red open squares c) Change in fill factor and V_{OC} as a function of time under AM1.5G light soaking at 100 mW/cm^2 irradiance.

A light soaking effect has been previously observed for TiO_2 based liquid electrolyte devices [64, 235–239], however such phenomena are not usually observed in solid-state devices, and certainly not to the extent observed here, where the photocurrent more than doubles over the measurement time. When a similar effect has been observed in the past for electrolyte based DSCs, it has been interpreted by considering the influence of the ultraviolet light upon the TiO_2 surface states [235–238]. UV exposure to TiO_2 can result in increased oxygen vacancy density which results in a relative positive shift in the surface potential. Dye-sensitizers which were previously poor at injecting charge into the TiO_2 then become capable of undergoing efficient photoinduced electron transfer, resulting in improved device photocurrent and efficiency [235].

Here, this phenomenon is observed in SnO_2 based devices, where the band gap of SnO_2 is approximately 3.8 eV, compared with 3.2 eV in TiO_2. To test whether UV absorption in the SnO_2 is at the root of this phenomenon, some devices were measured under exposure to white light generated from an array of LEDs (LXHL-NWE8) where there is no light emitted under 400 nm (3.1 eV). Figure 6.1 b) shows the evolution of a device J_{SC} under such illumination (red open squares), and once again the same trend with increasing photocurrent over 20 minutes is observed. The devices return to their pre-illuminated state after being left in the dark for about 30 minutes, illustrating that the process occurring is reversible. Remarkably, the device shown in Figure 6.1 b) was measured 14 months after fabrication (stored in air in the dark without encapsulation) and exactly the same "kinetics" were observed, indeed even 2 years after fabrication the performance remains the same. To further conclude that UV light is not required, the same trends in increasing photocurrent are also observed when the device is illuminated with red LEDs (data not shown)[5]. JV measurements carried out on SnO_2 SDSCs without MgO treatment show very poor efficiency and J_{SC} values [148, 233], and are therefore not discussed here.

---

[5] This experiment was conducted by Pablo Docampo as part of capacitance measurements

6.3.2 Transient photovoltaic measurements

Since high-energy (UV) photons are clearly not a prerequisite for the observed light-soaking effects, it appears that photo induced charge generated in the device is responsible for this effect, and not necessarily a chemical change to the oxide surface under direct light absorption. This improvement in photocurrent could be due to enhanced charge collection (i.e. fewer losses due to recombination of free electrons and holes) or enhanced charge generation. In order to probe the charge collection, a series of small perturbation transient photovoltage and photocurrent decay measurements were conducted on the SnO_2-MgO/D102 SDSCs under short-circuit conditions. The white light bias was maintained at an equivalent of $100\,\mathrm{mW/cm^2}$ irradiance for comparison with the results obtained under simulated sun light. Typical trends for the transport and recombination rates are shown in Figure 6.2. The electron transport rate k_{trans} is seen to increase as a direct result of exposure to light. Surprisingly however, the recombination rate k_{rec} also increases, but marginally faster than the transport, negating any potential improvements from faster charge collection. This is in contrast to the longer term light soaking study performed by Listorti *et al.* on TiO_2 based electrolyte cells who found a notable reduction in the recombination rate as a function of light soaking [64]. Contrary to expectations, therefore, charge collection efficiency (η_{coll}), calculated using Eqn. 3.11 and shown with red stars in Figure 6.2, is seen to decrease as a result of light-soaking, even though J_{SC} (red diamonds) measured simultaneously during the same experiment is seen to increase with time. These measurements indicate that improved charge collection is not the cause for the enhanced photocurrent under light soaking.

6.3.3 Optical Pump Terahertz Probe Measurements

Assuming the trend observed in the transient measurements to be correct, and that improved charge collection is not the cause for the enhanced photocurrent, other possible factors are now considered. Photocurrent is a product of the absorbed light, charge generation efficiency and charge collection efficiency. The charge collection appears not to improve, the films do not appear to change considerably in colour, hence charge generation is most likely to

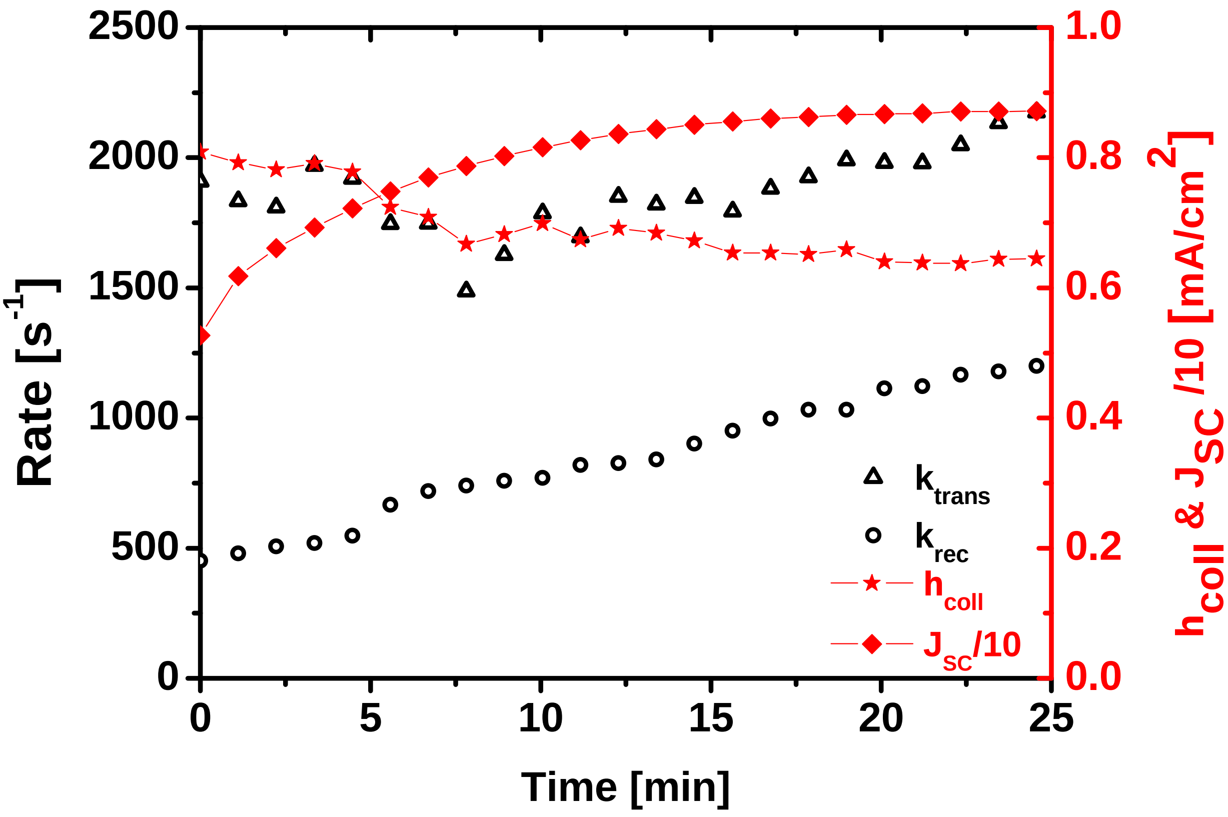

Figure 6.2: Transport (black open triangles) and recombination (black open circles) rates as a function of light-soaking time, along with short-circuit current (red diamonds) and estimated charge collection efficiency η_{coll} (red stars), determined by transient photovoltage and photocurrent measurements performed under short-circuit conditions.

influence this improvement in photocurrent under illumination. A recent study on long term light soaking effects in TiO_2 based DSCs by Listorti *et al.* showed a strong correlation between enhanced photoluminescence quenching rates of the dye-sensitizer and enhanced photocurrent [64]. This finding is interpreted to imply that enhanced electron transfer in that system is the mechanism behind the increase in photocurrent. This correlation is surprising, not because of the inferred mechanism, but since the time-correlated single photon counting technique employed has a temporal resolution on the 100 ps timescale, which is much slower than the typical observed electron transfer rate of fs to ps.

In order to directly probe the electron transfer process in this system, and to shed more light upon the possible correlation between fs and ns measurement techniques, optical-pump terahertz-probe (OPTP) spectroscopy has been employed on dye-sensitized SnO_2 films. These measurements have been conducted using the ruthenium-based Z907 sensitizer since the organic dye D102, which operates best in the solar cells, degrades when photoexcited during the OPTP measurements (less photostable). On the other hand, device results have been shown only for D102 sensitized SDSCs because SnO_2/Z907 SDSC performance was too poor for any light-soaking effect to be significant. The SnO_2/Z907 films were photoexcited with very short duration pulses (∼40 fs) at 550 nm wavelength. The photoexcitation fluence was equivalent to the photon densities absorbed by the cells when exposed to simulated sunlight at 100 mW/cm^2 irradiance. The 550 nm photons are absorbed by the dye and promote it to the excited state, from which photoinduced electron transfer occurs into the SnO_2 CB due to a favourable electronic driving force. These relatively mobile CB electrons interact with the weak terahertz (THz) probe pulse incident on the sample at time τ after the initial excitation pulse. The amount of THz radiation absorbed gives a direct estimate of the product of the number and mobility of charge carriers in the photoexcited sample.

Figure 6.3 a) shows the rise in photoconductivity in SnO_2/Z907 samples over the first 15 picoseconds after photoexcitation at 550 nm. As noted earlier, this increase is primarily due to electron transfer from the dye photoexcited states into the SnO_2 CB. The different curves show successive scans, where each scan took about 70 minutes to complete. It

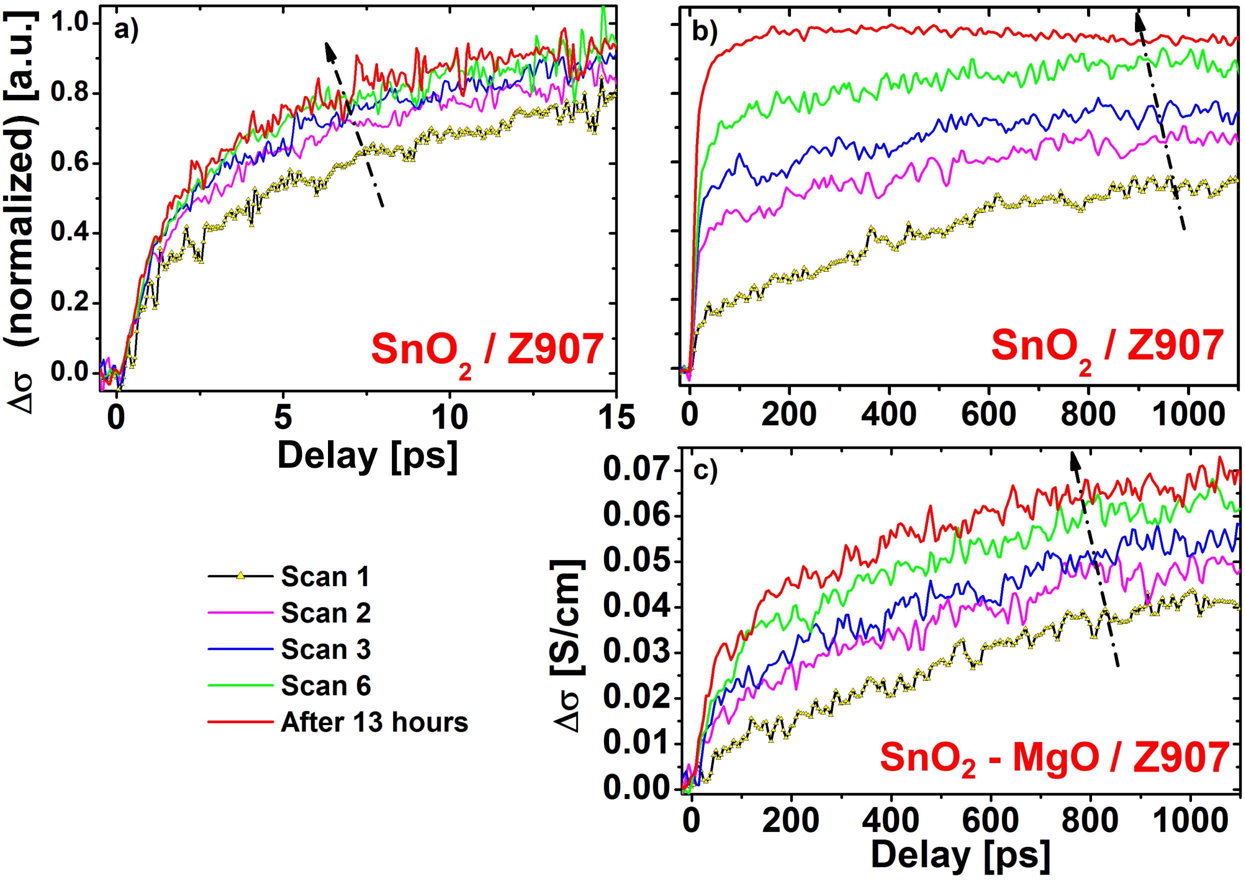

Figure 6.3: a) Early-time photoconductivity dynamics in Z907-sensitized SnO_2. Each scan was 71 minutes long and all scans were carried out in succession, without a break; b) Long-time photoconductivity scans, each 38 minutes long. Note a) and b) are separate measurements. c) Long-time scans measured on SnO_2 with a conformal MgO coating, sensitized with Z907, each 22 minutes long. In all cases, the red curve at the top shows the final “steady-state” trend measured after at least 13 hours of continuous photoexcitation. Photoexcitation was carried out with 550 nm wavelength 40 fs pulses with $\sim 7 \times 10^{14}$ photons/cm^2 fluence on samples kept under vacuum. All scans were carried out from τ=0 to longer times. Curves in a), b) have been normalized so that the peak photoconductivity value (at ∼200 ps, red curve in b) is 1.

is interesting to see that as time progresses, both the charge injection rate and the peak photoconductivity value ($\Delta\sigma$) increase significantly, until 'steady-state' is achieved after a few hours of exposure to the light pulse train. The trend can be seen more distinctly in the long-time scans shown in Figure 6.3 b). Each scan in this graph took 38 minutes to complete. The final red curve, achieved after 13 hours of light-exposure, is different from the previous scans because charge transfer is completed by about 200 ps instead of over a nanosecond. Once steady state is achieved, there are only two fast electron transfer phases (fs and sub 100 ps), followed by a slow decrease in conductivity. This decrease can be attributed to electron trapping, rather than recombination of the electrons with holes in the dye. This is because the recombination lifetime has been shown to be much slower, in the 0.1–1 ms time range, as shown schematically in Figure 2.5 [78, 79].

It should be mentioned that the final red scan in Figure 6.3 b) was measured on the same sample as that in Figure 6.3 a) after it had already been light-soaked for more than 13 hours. All the other scans in Figure 6.3 b) were measured on a different sample (prepared under identical conditions), which shows a similar light-soaking effect. Since the absolute photoconductivity values for the two samples are different, only the normalized values are shown here for easy comparison. There is a significant variation in the relative contribution of the fast and slower injection phases with exposure time, but the time constants of the phases appear to remain relatively unchanged. In Chapter 5, the relative fractions of fast to slow injection phases in TiO_2, SnO_2 and ZnO DSCs were correlated with the charge generation efficiency. The fast phase is clearly least likely to compete with other loss mechanisms in the photoexcited dye (eg. natural decay), and therefore these OPTP measurements shown here are perfectly consistent with the increase in photocurrent observed in the solar cells as a function of illumination time.

The above measurements were performed on 'bare' SnO_2 sensitized with Z907, but to be consistent with the solar cell measurements, OPTP spectroscopy was also performed on SnO_2 films coated with a thin shell of MgO and sensitized with Z907 dye (SnO_2-MgO/Z907), shown in Figure 6.3 c). As seen with the bare films, the charge injection rate and photoconductivity are seen to rise steadily with each successive scan. This suggests a similar effect in MgO-treated SnO_2 films, in excellent agreement with the JV measurements shown on SnO_2-MgO based SDSCs in Figure 6.1. The overall injection rate is slower for the MgO coated dye-sensitized photoanodes. This is discussed in more detail later in Section 6.3.5.

The same trend of light exposure dependent increase in photoconductivity is observed when photoexcitation is carried out with half the fluence, indicating that the light-soaking effect is a feature of the material combination, and not just an artifact due to high excitation fluences. For this case of photoexcitation at 550 nm at lower energy, the absorbed photon fluence in SnO_2/Z907 is approximately 7.5×10^{16} photons/cm^2/s. In comparison, the corresponding absorbed photon fluence in the SnO_2-MgO/D102 devices exposed to AM1.5G light at 100 mW/cm^2 is equivalent to about 7×10^{16} photons/cm^2/s when integrated between 300–800 nm (minimum and maximum limits set by the solar spectrum and SnO_2-MgO/D102 absorption respectively). While these figures cannot be directly compared because the OPTP samples are excited with femtosecond duration pulses at 500 Hz repetition rate compared to steady-state illumination of the solar cells, this suggests that the exposure is roughly equivalent.

These early-time photoconductivity trends confirm that light soaking of the dye-sensitized SnO_2 film leads to improved charge generation, consistent with the increased photocurrent and device performance. However, the cause for the increased electron transfer rate and efficiency is not directly apparent. To summarize the findings so far: 1. The presence of a UV component is not critical for device improvement, eliminating the hypothesis that direct light absorption in the metal oxide results in the creation of new surface states and a resultant positive shift in the conduction band edge. 2. The process is relatively slow yet reversible. 3. Since it appears in both 'bare' dye-sensitized films and MgO coated films, it is not an artifact of the surface coating. 4. It is not explicitly a result of lithium-TFSI salt migration or redistribution [235, 239], nor results from a change in photo doping of the hole-transporter since it is observed by OPTP spectroscopy in the neat dye-sensitized films. It should also be noted that in the case of the aforementioned measurements under red light illumination negligible light is absorbed in the hole-transporter.

It appears evident therefore that the build-up of electronic charge in the SnO_2 is triggering this favourable trend. There are two possible explanations: The first is that the net negative charge of the SnO_2 forces a rearrangement of charged states or species at the surface of the metal oxide, which could cause a shift in surface potential or indeed alter the precise energy distribution of the sub bandgap states. These species could be protons, partially reduced Sn^{4+} states or hydroxide species. The second is related but arises from considering the nature of the bonding between the oxygen and tin ions in the oxide material. With the bonding being predominantly ionic, it could be envisaged that localized negative charge trapped in surface states could have a very strong influence, weakening the local binding strength between the Sn ions centered on the trap sites and the negatively charged surface oxygen. Hence the increased concentration of localized electrons under illumination could alter to a certain extent the surface oxygen vacancy density. For the more studied oxide, TiO_2, when oxygen vacancies are generated, partially reduced Ti^{4+} states are thought to induce sub bandgap states around $\sim$1 eV below the conduction band [240, 241]. A similar effect is expected in SnO_2.

6.3.4 Capacitance measurements

To verify the influence of light-soaking upon the distribution of sub bandgap states in SnO_2, transient photovoltage/photocurrent measurements have been performed on a SnO_2-MgO/D102 SDSC illuminated with red LEDs[6]. This was done by measuring the change in capacitance as a function of illumination time at different light bias conditions (and, therefore, at different V_{OC} values). The experimental set-up is described in Section 3.3. Figure 6.4 a) shows that the capacitance increases for a given energy level with increased exposure to light. This suggests a broadening of the density of sub bandgap states (DoS) (proportional to measured capacitance) over time with illumination. Figure 6.4 b) shows the same data but presented in a semi-log graph with the axes swapped. It shows a clear shift of

---

[6] Capacitance measurements and analysis done by Pablo Docampo [233]

the capacitance (which is proportional to the DoS) towards lower potentials without any significant change to the slope of the curve, consistent with a shift in the surface potential of the SnO_2 [233].

Figure 6.4 c) shows an illustrative Gaussian conduction band with an exponential tail (sub bandgap states). Based on our interpretation of the measurement shown in Figure 6.4 a), light-soaking leads to an increase in the available energy states, as shown in red. The inset of this diagram zooms into the tail of the DoS in the range which can be normally measured via photocurrent and photovoltage decay measurements, and depicts the trend seen in Figure 6.4 a). This technique measures sub bandgap states which were "full" under illumination at open-circuit and hence the photoinduced electron transfer is unlikely to take place directly into these measured states. Instead, the electron transfer is likely to take place directly into the conduction band. This diagram illustrates that the change in the tail of the DoS can be small, whereas at a given energy in the conduction band, the DoS can be increased by over 100%. This arises from the different gradients of the DoS moving from the tail to conduction band states. This sketch is only illustrative, but justifies why a small measured change in capacitance could be highly significant for charge generation. As the density of available states for charge transfer is increased, the electron injection yield from the dye in the DSC devices appears to increase significantly. This correlates well with the increase in photocurrent, accompanied by a decrease in V_{OC}, as seen in Figure 6.1. This is also in agreement with previous reports on different preparation methods for mesoporous TiO_2, where a change in the sub bandgap DoS correlates well with increased device photocurrent [64, 239].

6.3.5 MgO coating on SnO_2

As mentioned in the introduction, both liquid electrolyte and solid-state DSCs exhibit very poor performances when fabricated with 'bare' SnO_2 nanoparticles [38, 148, 229–232]. This is usually due to severe recombination losses. A successful alternative is to apply an optimized surface coating of an insulating oxide such as MgO, Al_2O_3, ZrO_2, TiO_2, etc. between the

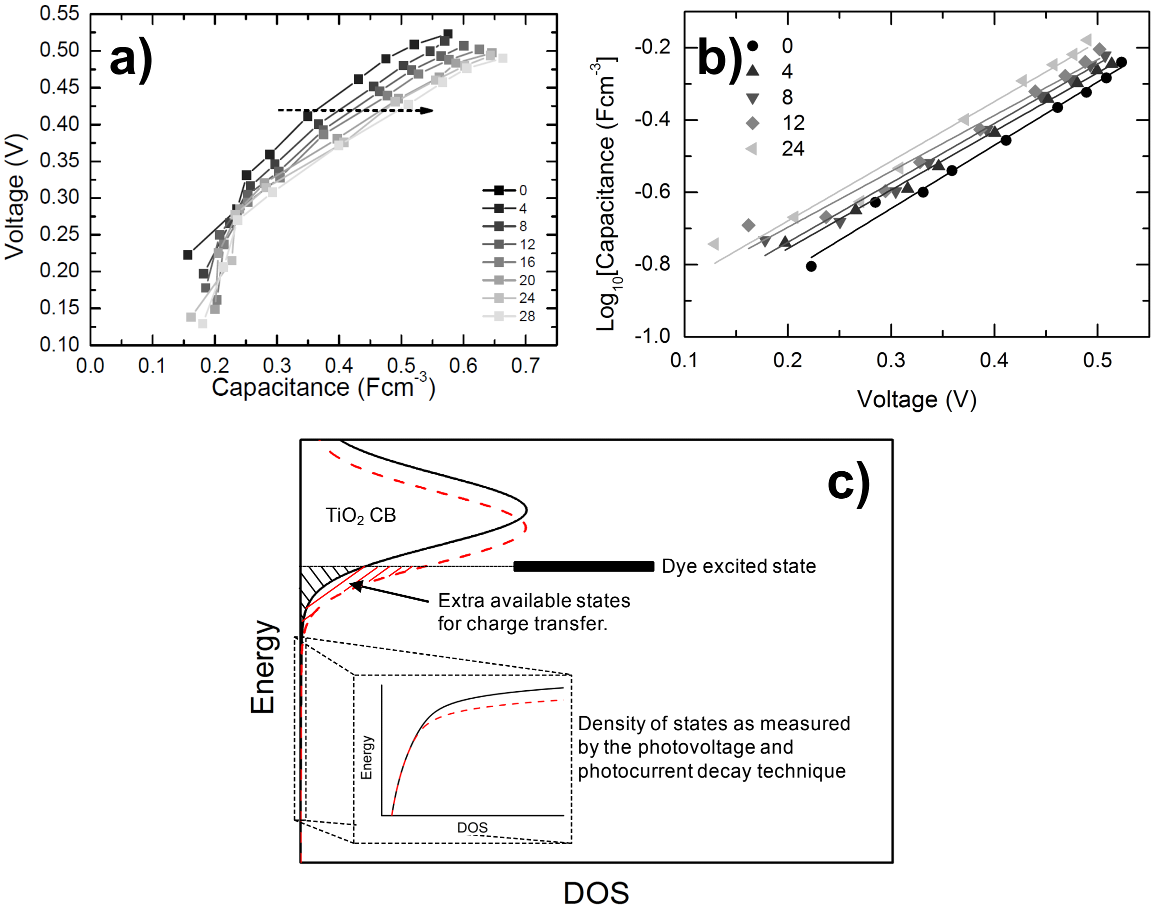

Figure 6.4: a) Change in capacitance *versus* voltage measurement in SnO_2-MgO/D102 SDSC devices as a function of light-soaking time. Red LEDS (∼600 nm) were used for both background and perturbation illumination. Measurements were taken every 4 minutes as shown in legend, with the initial measurement shown as black squares and every consecutive curve shown in a lighter shade of gray than the previous one. Solid lines represent exponential fits to the experimental data for each light-soaking time. b) Semi-log plot of the data shown in a). As before, solid lines represent exponential fits. c) Cartoon of the expected conduction band shift and its effect on the available states for charge transfer at the level of the dye excited state. The “zoom in” shows the density of states (capacitance) as measured in a). The available states for electron injection pre-light soaking are shaded in black and for post-light soaking, they are cross-shaded in red.

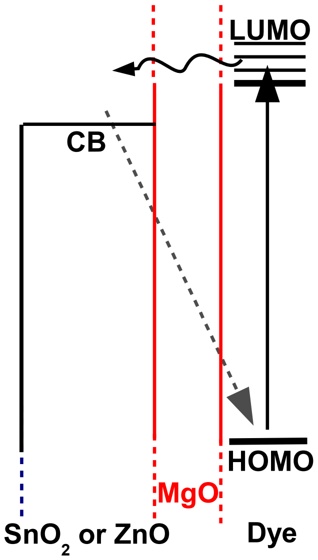

Figure 6.5: Cartoon of the expected electronic processes taking place in a dye-sensitized SnO_2 or ZnO mesoporous film with a subnanometer coating of MgO.

SnO_2 and the dye. This can potentially decrease the recombination rate, thus improving both the V_{OC} and J_{SC} [148, 231]. TEM images of SnO_2 nanoparticle films coated with MgO and TiO_2 can be found in Ref. 148. The same recipe has been employed in my work and has been described in Section 6.2. The current understanding is that the photoexcited electrons in the dye LUMO states are able to tunnel through the 1–2 nm thin film of the high bandgap material into the SnO_2 nanoparticles and can be successfully transported to the anode, as depicted in Figure 6.5. However, the recombination between the electrons in the SnO_2 matrix and the redox electrolyte or the hole-transport gets slowed down because of this layer, as shown by Green *et al.* using nanosecond transient absorption spectroscopy [231]. This can be explained by an upwards shift of the SnO_2 CB edge by almost 250 mV observed in the presence of MgO, measured by Docampo *et al.* [233].

As discussed earlier, terahertz pump probe scans were carried out on SnO_2 films sensitized with Z907 dye, both with and without an MgO shell surrounding the nanoparticles. The light-soaking effect has already been discussed in detail above. In addition, it is interesting

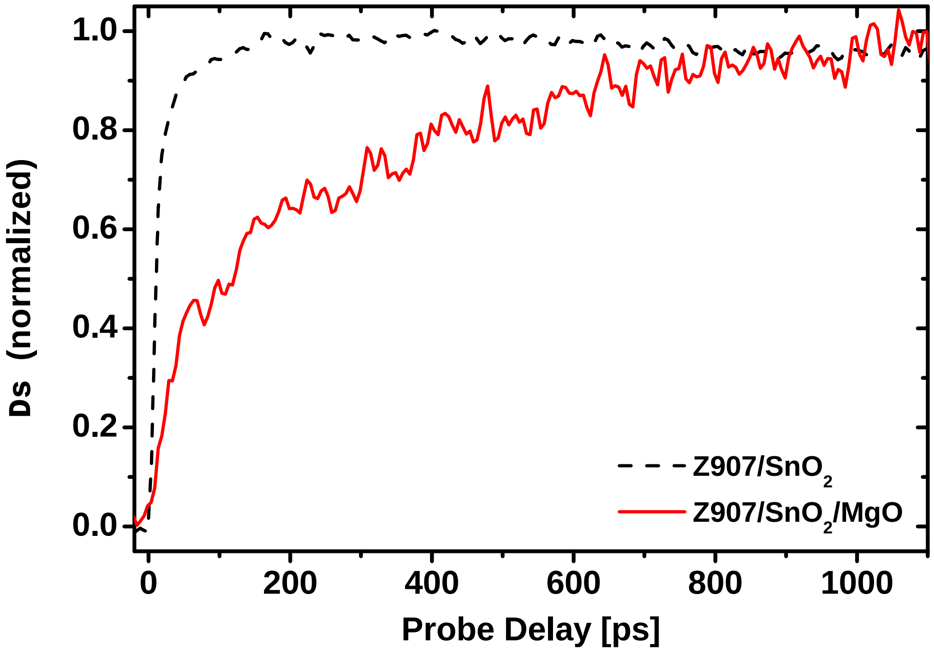

Figure 6.6: THz photoconductivity dynamics in SnO_2 mesoporous films sensitized with Z907 dye, both with (red solid line) and without (black dashed line) a conformal MgO coating. Photoexcitation was carried out with 550 nm wavelength 40 fs pulses with 7×10^{14} photons/cm^2 incident fluence on samples kept under vacuum.

to note that while the initial few scans in the SnO_2/Z907 films both with and without MgO treatment are very similar, the final 'steady-state' scans are quite different. The steady-state curves from Figures 6.3 b) and c) have been redrawn in Figure 6.6 for easy reference. While complete charge injection takes place within the first 200 ps in case of SnO_2, photoconductivity value is still rising at 1 ns in case of MgO treated SnO_2. Data shown here has been normalized at the respective maxima for each curve (∼200 ps for SnO_2/Z907, 1 ns for SnO_2-MgO/Z907). The absolute photoconductivity values have not been compared here because the slight difference in the measured values could be attributed to laser power fluctuation or sample-to-sample variation. The charge injection rate is, therefore, adversely affected due to the presence of the wide bandgap layer. This is to be expected, given that the insulating shell appears to cause a negative shift in the SnO_2 CB level [233]. The overall device performance depends on a subtle balance between the charge injection, transport and recombination times [80], hence further detailed studies measuring the effect of the insulating film on recombination rate will be useful in determining the efficacy of such treatments.

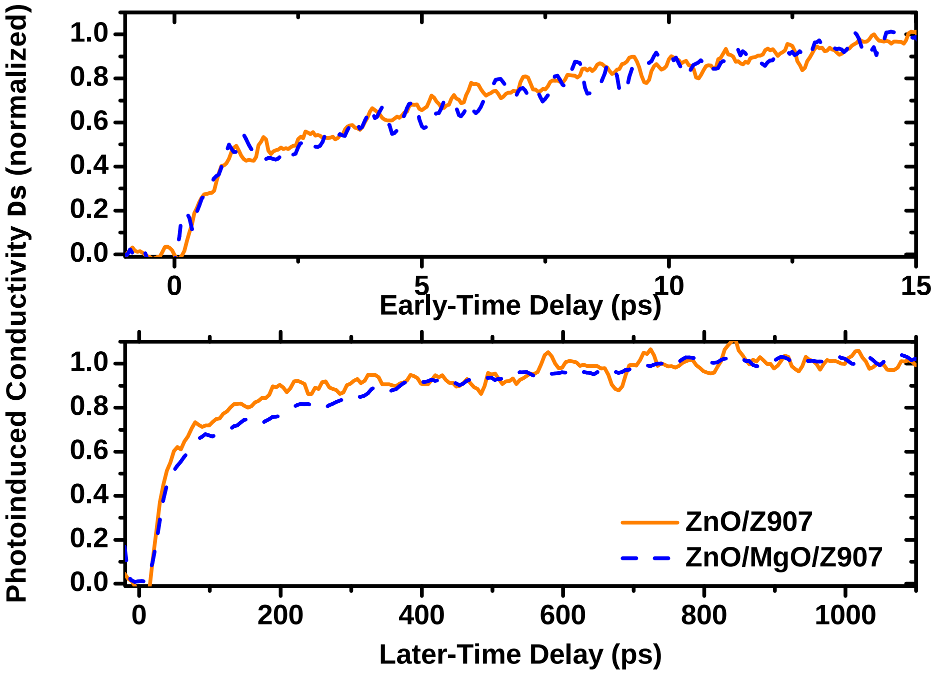

Figure 6.7: Early and later time photoconductivity dynamics in ZnO mesoporous films sensitized with Z907 dye, both with (blue dashed line) and without (orange solid line) an MgO coating. Photoexcitation was carried out with 550 nm wavelength 40 fs pulses with 7×10^{14} photons/cm^2 incident fluence on samples kept under vacuum.

6.3.6 MgO coating on ZnO

Similar comparative OPTP studies were also carried out on mesoporous ZnO films both with and without a conformal MgO coating. The same recipe was used as described earlier in Section 6.2 for MgO treatment of SnO_2. In stark contrast to dye-sensitized SnO_2, no light-soaking effect was observed in the ZnO films. Also, Figure 6.7 shows that the MgO treatment made no difference to the charge injection dynamics. This suggests that either there is no significant shift in the ZnO CB edge in the presence of the high bandgap shell, or the ϕ_{inj} is already too slow to be affected by this change in CB level (see discussion accompanying Figure 5.2). Additional photovoltaic measurements need to be conducted on MgO-treated devices and compared with observations made on the SnO_2 system, in order to better understand the difference between the two material systems.

6.4 Conclusions

A significant increase in the short-circuit photocurrent of SnO_2 based solid-state DSCs has been observed under illumination, where approximately 20 minutes of AM1.5G 1 Sun light soaking is required to reach maximum efficiency. Through a combined device-based and spectroscopic study, it has been demonstrated that a systematic enhancement in the electron transfer yield is responsible for the increased photocurrent under visible light illumination. This improved injection has been attributed to an increase in the relative density of acceptor states in the SnO_2 at a given energy, which is postulated to be caused by an increase in the oxygen vacancy density upon charging.

Terahertz spectroscopy has also been used to study the effect of applying a thin conformal coating of a high band-gap metal-oxide such as MgO over SnO_2 and ZnO mesoporous films. While in SnO_2, a significant retardation in electron injection rate is observed in the presence of MgO, MgO-coated ZnO shows negligible difference. The significance of this observation has then been discussed briefly.

Chapter 7

Conclusions and Outlook

The work presented in this dissertation is aimed at conducting an in-depth optical spectroscopic study of materials used in dye-sensitized solar cells (DSCs). To this end, subpicosecond resolution optical-pump terahertz-probe (OPTP) spectroscopy has been employed on dye-sensitized mesoporous metal-oxide films, in order to measure intra-particle electron mobility, and early-time charge transfer dynamics from the dye excited states into the semiconductor conduction band in a solar cell. These measurements have been complemented with photovoltaic-related measurements done on liquid electrolyte and solid-state DSCs fabricated from the same metal-oxide pastes. The overall intention is to build on the current understanding about how different dye molecules interact with different nanostructured metal-oxides such as TiO_2, ZnO and SnO_2, so that the DSC architecture and materials can be optimized to maximize photon-to-current generation efficiency. In this ‘conclusions and outlook’ chapter, the key results have been briefly reviewed, and suggestions for future work have been given.

TiO_2 is the most popular choice of materials for use as photoanode in both liquid electrolyte and solid-state DSCs. This is because of its high dielectric constant, respectable electron mobility, easy availability, and a vast knowledge-base about the material. Although a lot of photovoltaic and spectroscopic studies have been conducted on TiO_2-based cells over the past many years, there are still some unresolved questions about the true charge injection dynamics in dye-sensitized TiO_2. With this in mind, subpicosecond resolution OPTP spectroscopy has been used in Chapter 4 to measure electron injection efficiency in

Z907-sensitized TiO_2. Biphasic injection has been observed, with an ultrafast sub-500 fs component followed by a slower 70–200 ps component. Based on IPCE, charge collection efficiency, and UV-Vis absorbance measurements conducted on liquid electrolyte TiO_2/Z907 cells, charge injection efficiency has been calculated in Chapter 5 to be near-unity. This shows that the TiO_2/Z907 system is highly optimized, and, therefore, injection rate being slower than the femtosecond time-range is not an issue for these devices.

Based on the OPTP photoconductivity measurements, electron mobility in nanostructured TiO_2 has been calculated to be about $0.1\,\mathrm{cm^2/Vs}$, about an order of magnitude smaller than in bulk TiO_2. This can be partly explained by the restricted electron movement because of both geometrical constraints and increased surface trap sites in the nanostructured material. In addition, the mesoporous film behaves like a nanostructured composite material, with the TiO_2 nanoparticles embedded in a low dielectric medium (air or vacuum), leading to lower electron mobility. In addition, TiO_2 films treated with $TiCl_4$ have been studied using OPTP in order to understand the reason for the observed enhanced device performance in the case of $TiCl_4$-treated TiO_2 DSCs. $TiCl_4$ treatment does not seem to influence the early time charge dynamics, suggesting the need for looking at electron recombination dynamics taking place at longer time-scales using transient absorption spectroscopy experiments.

As a follow-up to this work, it will be interesting to explore the correlation between electron mobility and the morphology of the TiO_2 sintered network. Recently, a technique for fabricating a fully interconnected TiO_2 matrix through a diblock copolymer approach has been optimized in the Snaith lab [42, 160, 242]. The morphology and porosity can be controlled by varying the polymer:TiO_2 ratio. It is expected that films made with different amounts of TiO_2, and hence, with different porosities, would exhibit unique spectral signatures in the terahertz frequency range. Also, recent work by Guldin *et al.* demonstrated that the TiO_2 crystal size can be controlled by changing the sintering temperature [42]. This could potentially be a good experiment for studying the correlation between electron mobility and crystal size. Additionally, the OPTP set-up can be customized for studying charge injection dynamics in aligned TiO_2 nanotubes or nanowires, to check for enhanced electron collection in the presence of an electric field.

Over the past few decades, the majority of photovoltaic and spectroscopic studies have been conducted on the TiO_2 system, with the result that the TiO_2 device architecture has been highly optimized. Most of the dye sensitizer molecules available in the market work best with TiO_2. However, despite all this effort, there hasn't been a significant increase in the TiO_2 DSC efficiency since the first demonstration in 1991 [7]. This suggests the need for looking at other metal-oxides to replace TiO_2 as the electron-transporting layer. ZnO and SnO_2 are perfect candidates for this position, owing to their favourable band energetics. However, so far, devices fabricated with ZnO or SnO_2 have not been able to out-perform TiO_2 DSCs. To understand why, mesoporous films of ZnO and SnO_2 have been studied using OPTP in Chapter 5. The electron mobilities of these materials has been calculated and compared with that of TiO_2, and the reasons for the observed differences have been discussed in detail in the chapter.

One of the main conclusions of Chapter 5 is that while electron mobility in mesoporous TiO_2 is quite close to the TiO_2 bulk mobility, the difference between nanoparticle and bulk mobilities in SnO_2 is significant ($1\,\mathrm{cm}^2/\mathrm{Vs}$ and $250\,\mathrm{cm}^2/\mathrm{Vs}$, respectively). It would be difficult, therefore, to achieve any significant improvements in nanostructured TiO_2 charge carrier mobility, while there is a large scope for improvement in SnO_2. Hence, as a future study, it would be of great interest to do a comprehensive study of electron mobility dependence on the SnO_2 crystal size.

While conducting OPTP measurements on dye-sensitized SnO_2 films, a very interesting light-soaking effect was observed, whereby the electron injection rate and peak photoconductivity were observed to increase steadily with exposure to the photoexcitation source. The same trend was repeated when solid-state SnO_2 DSCs are exposed to simulated sunlight or an array of white LEDs - there was a monotonic increase in short-circuit photocurrent and device efficiency with light exposure, until steady state was achieved. Further experiments were conducted to understand the reason behind the phenomenon and a possible explanation has been presented in Chapter 6. It has been proposed that exposure to light results in a build up of space charge in SnO_2 and hole space-charge in the dye or hole-transporter, resulting in an electric field across the dye-sensitized heterojunction. This causes a rearrangement of charge species at the metal-oxide surface, ultimately leading to increased density of electron acceptor states in SnO_2 or a positive shift in the SnO_2 conduction band. The increase in acceptor density of states was confirmed by conducting transient photovoltage and photocurrent measurements on the devices.

Appendix A

Quasiparticles

In contrast to 'elementary particles' in condensed matter physics, quasiparticles and collective excitations arise when a crystal lattice or similar system behaves as if it contains weakly interacting particles in free space. For instance, a charged particle or photon travelling through a lattice interacts with all the electrons, nuclei, lattice defects, etc. in its vicinity in a complex fashion. This particle movement is approximately equivalent to that of a particle with a different effective mass travelling unpertubed through free space. The resulting quasiparticle can be thought of as a single particle accompanied by a distortion cloud in the lattice [162]. Some examples relevant to the work reported in the thesis are described below:

A.1 Phonons and polarons

In a crystal lattice, the energy of the lattice vibration is quantized and is called a phonon, in analogy with the quantized photon of the electromagnetic wave [144, 162]. The vibrations can arise from various forces including mechanical, thermal, electromagnetic etc. When a charge carrier (electron or hole) is travelling through a polar solid, it interacts with the ions in the lattice causing a local displacement of the lattice in the immediate vicinity of the particle. This particle with its local lattice distortion is equivalent to a quasi-particle with quantized energy, and is called a polaron. The charge carrier, therefore, has to drag the heavy ion cores in its vicinity as it travels, thus increasing its effective mass and lowering its mobility. The effect is large in ionic crystals because of the strong coulombic interaction between electrons/holes and ions. Equivalently, the effect is much weaker in covalent crystals because of the weaker interaction between the two entities.

The deformation in the crystal lattice leads to a polarization locally centred on the charge carrier. Depending on whether the polarization cloud is much larger or smaller than the atomic spacing in the material, there can be 'large' or 'small' polarons. For instance, in case of a sufficiently strong electron-phonon interaction, small polarons are formed. This corresponds to localized self-trapped electrons or holes, whereby charge transport typically occurs through thermally activated hopping from one site to the next [139, 144, 162]. At lower temperatures, the charged particle tunnels slowly through the crystal, as if in a band of large effective mass. On the other hand, large polarons are based on much weaker electron-lattice interactions and exhibit bandtype behaviour, although with effective mass larger as compared to the band mass associated with an electron in a rigid lattice.

Titania (TiO_2) is a transition metal oxide whose chemical bonding is regarded as intermediate between ionic and covalent [219]. The highly polarizable TiO_2 lattice deforms around an electron that passes through the lattice, such that the polaron mass in rutile TiO_2 varies between $8\,\mathrm{m}_e$ to $190\,\mathrm{m}_e$, where m_e is the free electron mass [219]. Based on THz measurements, Hendry *et al.* have showed that TiO_2 exhibits intermediate-sized polarons resulting in a low electron mobility of about $1\,\mathrm{cm}^2/(\mathrm{Vs})$ in bulk TiO_2 [139].

A.2 Excitons

Photoexcitation can sometimes result in an electron and hole pair which is bound to each other through an attractive Coulomb interaction. This electrically neutral quasiparticle is called an exciton. The exciton binding energy is in the 1–100 meV range depending on the dielectric constant of the medium and the temperature [141]. In insulators such as solid xenon (inert gas) or sodium chloride (ionic solid), the electronic shells within each atom are always full and the electrons are not much affected by the presence of neighbouring atoms. Excitons in such materials are localized and tightly bound with very high binding energy [162, 243, 244]. On the other hand, many semiconductors such as silicon, GaAs etc. are covalent in nature with higher interatomic interaction. In such cases the photoexcited electron is weakly bound to the hole, resulting in an exciton with an average electron-hole distance (exciton radius) much larger than the interatomic distance.

Movement of free charge carriers induces an electric field in the medium. In contrast, movement of bound electron-hole pairs results in transporting energy without transporting net electric charge. This is usually a loss mechanism in typical solar cells as described in the thesis because any photogenerated electron-hole pairs that are excitonic in nature can not contribute to the photocurrent. The identification of excitonic populations is therefore critical for redesigning and optimizing device performance.

Terahertz spectroscopy is an ideal technique for identifying free and bound charges because of its ability to simultaneously measure both the real and imaginary components of frequency-dependent THz photoconductivity at a sub-picosecond time-scale. This can be exploited for detecting excitons, both through resonant interactions with internal exciton transitions (at energies typically a fraction of the exciton binding energy), and through a non-resonant interaction, by measuring the polarizability associated with the electron and hole wave-functions of the exciton [141]. This has been demonstrated in a variety of materials such as ZnO [127, 244], poly2-methoxy-5-(2'-ethyl-hexyloxy)-*p*-phenylene-vinylene (MEH-PPV) polymer [138, 200], etc.

A.3 Exciplexes and excimers

An excimer is a short-lived charge transfer complex formed from two species, at least one of which is in an electronic excited state [245]. These constituting species usually do not bond if both are in the ground state. In excimers (short for excited dimer), both the interacting components are the same molecule or atom. Similarly, exciplexes are formed by the interaction of two distinct chromophores: D (donor) and A (acceptor), either of which is in the excited state, $\mathrm{D}^* + \mathrm{A}$ or $\mathrm{D} + \mathrm{A}^*$ [246]. The excited state complex is stable as a result of resonance contributions from both exciton and charge-transfer configurations:

$$\mathrm{D}^*\mathrm{A} \longleftrightarrow \mathrm{DA}^* \longleftrightarrow \mathrm{D}^{\cdot +}\mathrm{A}^{\cdot -}$$

The electronic states of the donor-acceptor pair (D^*A or DA^*) with a wave-function Φ_N and the corresponding ion pair (D^+A^-) with wave-function Φ_I mix together through charge-transfer interactions. While excimers and exciplexes have been frequently reported in several pi-conjugated polymers [246–248], DSC materials exhibit significantly fewer instances of such interactions. The excited dye molecules can interact with either the continuous, delocalized states in the semiconductor conduction band or the discrete, localized states at the surface, resulting in complicated electronic interactions during charge injection and separation. Recently, experiments using mid-IR transient absorption spectroscopy [222] and THz spectroscopy [100] have shown the presence of an intermediate charge transfer state during electron transfer from the dye excited state (D^*) to the acceptor states (A) in ZnO-based DSCs. The exciplexes can have a neutral or ionic character depending on whether the D^*A state is energetically more stable than the D^+A^- state or not, with an approximate wave-function $\Phi_\mathrm{N} + \delta\Phi_\mathrm{I}$ or $\delta\Phi_\mathrm{N} + \Phi_\mathrm{I}$, respectively [222].

Appendix B

Dye Molecular Structures

The molecular structures of dyes frequently mentioned in the thesis are given below for quick reference:

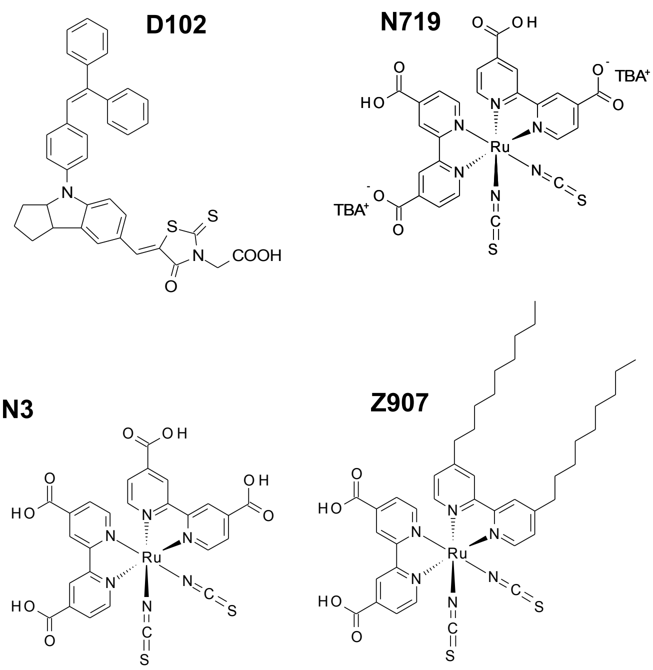

Figure B.1: Dye molecular structures.

Dye Names

D102	(5-4-[4-(2,2-diphenylvinyl)phenyl]-1,2,3,3a,4,8b-hexahydro-cyclopenta[b]indol-7-ylmethylene-4-oxo-2-thioxo-thiazolidin-3-yl)acetic acid
N3	$[Ru(dcbpyH_2)_2(NCS)_2]$
N719	$(Bu_4N)_2[Ru(dcbpyH)_2(NCS)_2]$
Z907	NaRu(4-carboxylic acid-4'-carboxylate)(4,4'-dinonyl-2,2'-bipyridine)$(NCS)_2$

Bibliography

[1] BP. "BP Statistical Review of World Energy" (June 2011) (www.bp.com/statisticalreview).

[2] National Academies. "Joint science academies statement: Global response to climate change" (2005) (http://nationalacademies.org/onpi/06072005.pdf).

[3] The World Bank. "WDR 2010: Development and Climate Change" (2010) (available online).

[4] O Morton. *Nature*, **443** (2006) 19–22.

[5] Vaclav Smil. "Energy at the cross-roads". MIT Press, first edition (2003).

[6] David MacKay. "Sustainable Energy - Without the Hot Air". UIT Cambridge Ltd., first edition (2009).

[7] B Oregan & M Grätzel. *Nature*, **353** (1991) 737.

[8] M Grätzel. *Prog. Photovoltaics*, **14** (2006) 429–442.

[9] M Grätzel. *Accounts Chem. Res.*, **42** (2009) 1788–1798.

[10] H J Snaith & L Schmidt-Mende. *Adv. Mater.*, **19** (2007) 3187–3200.

[11] M A Green, K Emery, Y Hishikawa, W Warta & E D Dunlop. *Prog. Photovoltaics*, **19** (2011) 565–572.

[12] A Hagfeldt, G Boschloo, L C Sun, L Kloo & H Pettersson. *Chem. Rev.*, **110** (2010) 6595–6663.

[13] M Grätzel. *Nature*, **414** (2001) 338.

[14] H Tsubomura, M Matsumura, Y Nomura & T Amamiya. *Nature*, **261** (1976) 402–403.

[15] N Robertson. *Angew. Chem.-Int. Edit.*, **45** (2006) 2338–2345.

[16] S Ardo & G J Meyer. *Chem. Soc. Rev.*, **38** (2009) 115–164.

[17] J C Wang, Y L Su, J C Shieh & J A Jiang. *Sol. Energy Mater. Sol. Cells*, **95** (2011) 843–851.

[18] A Usami, S Seki, Y Mita, H Kobayashi, H Miyashiro & N Terada. *Sol. Energy Mater. Sol. Cells*, **93** (2009) 840–842.

[19] A Yella, H W Lee, H N Tsao, C Y Yi, A K Chandiran, M K Nazeeruddin, E W G Diau, C Y Yeh, S M Zakeeruddin & M Grätzel. *Science*, **334** (2011) 629.

[20] N Cai, S J Moon, L Cevey-ha, T Moehl, R Humphry-baker, P Wang, S M Zakeeruddin & M Grätzel. *Nano Lett.*, **11** (2011) 1452–1456.

[21] Udo Bach. "Solid-state dye-sensitized mesoporous TiO2 Solar Cells". Ph.D. thesis, cole Polytechnique Fdrale de Lausanne (2000).

[22] D Shi, N Pootrakulchote, R Z Li, J Guo, Y Wang, S M Zakeeruddin, M Grätzel & P Wang. *J. Phys. Chem. C*, **112** (2008) 17046–17050.

[23] K Murakoshi, R Kogure, Y Wada & S Yanagida. *Sol. Energy Mater. Sol. Cells*, **55** (1998) 113–125.

[24] T W Hamann, R A Jensen, A B F Martinson & J T Hupp. *Energy Environ. Sci.*, **1** (2008) 66–78.

[25] H N Tian & L C Sun. *J. Mater. Chem.*, **21** (2011) 10592–10601.

[26] T Daeneke, T H Kwon, A B Holmes, N W Duffy, U Bach & L Spiccia. *Nat. Chem.*, **3** (2011) 211–215.

[27] P Wang, B Wenger, R Humphry-baker, J-E Moser, J Teuscher, W Kantlehner, J Mezger, E V Stoyanov, S M Zakeeruddin & M Grätzel. *J. Am. Chem. Soc.*, **127** (2005) 6850–6856.

[28] D B Kuang, S Ito, B Wenger, C Klein, J-E Moser, R Humphry-baker, S M Zakeeruddin & M Grätzel. *J. Am. Chem. Soc.*, **128** (2006) 4146–4154.

[29] J Y Kim, T H Kim, D Y Kim, N G Park & K D Ahn. *J. Power Sources*, **175** (2008) 692–697.

[30] B Oregan & D T Schwartz. *J. Appl. Phys.*, **80** (1996) 4749–4754.

[31] K Tennakone, G R R A Kumara, I R M Kottegoda & K G U Wijayantha. *Semicond. Sci. Technol.*, **12** (1997) 128–132.

[32] U Bach, D Lupo, P Comte, J-E Moser, F Weissortel, J Salbeck, H Spreitzer & M Grätzel. *Nature*, **395** (1998) 583.

[33] H J Snaith & M Grätzel. *Adv. Mater.*, **19** (2007) 3643.

[34] R Katoh, A Furube, T Yoshihara, K Hara, G Fujihashi, S Takano, S Murata, H Arakawa & M Tachiya. *J. Phys. Chem. B*, **108** (2004) 4818–4822.

[35] J B Asbury, E Hao, Y Q Wang, H N Ghosh & T Q Lian. *J. Phys. Chem. B*, **105** (2001) 4545–4557.

[36] R W Fessenden & P V Kamat. *J. Phys. Chem.*, **99** (1995) 12902–12906.

[37] Y Fukai, Y Kondo, S Mori & E Suzuki. *Electrochem. Commun.*, **9** (2007) 1439–1443.

[38] A Kay & M Grätzel. *Chem. Mat.*, **14** (2002) 2930–2935.

[39] Y Diamant, S Chappel, S G Chen, O Melamed & A Zaban. *Coord. Chem. Rev.*, **248** (2004) 1271–1276.

[40] Q F Zhang, C S Dandeneau, X Y Zhou & G Z Cao. *Adv. Mater.*, **21** (2009) 4087–4108.

[41] R Jose, V Thavasi & S Ramakrishna. *J. Am. Ceram. Soc.*, **92** (2009) 289–301.

[42] S Guldin, S Huttner, P Tiwana, M C Orilall, B Ulgut, M Stefik, P Docampo, M Kolle, G Divitini, C Ducati, S A T Redfern, H J Snaith, U Wiesner, D Eder & U Steiner. *Energy Environ. Sci.*, **4** (2011) 225–233.

[43] E J W Crossland, M Kamperman, M Nedelcu, C Ducati, U Wiesner, D M Smilgies, G E S Toombes, M A Hillmyer, S Ludwigs, U Steiner & H J Snaith. *Nano Lett.*, **9** (2009) 2807–2812.

[44] L Schmidt-mende, U Bach, R Humphry-baker, T Horiuchi, H Miura, S Ito, S Uchida & M Grätzel. *Adv. Mater.*, **17** (2005) 813.

[45] A Mishra, M K R Fischer & P Bauerle. *Angew. Chem.-Int. Edit.*, **48** (2009) 2474–2499.

[46] R Zhu, C Y Jiang, B Liu & S Ramakrishna. *Adv. Mater.*, **21** (2009) 994.

[47] D Poplavskyy & J Nelson. *J. Appl. Phys.*, **93** (2003) 341–346.

[48] H J Snaith & M Grätzel. *Appl. Phys. Lett.*, **89** (2006) 262114.

[49] I K Ding, N Tetreault, J Brillet, B E Hardin, E H Smith, S J Rosenthal, F Sauvage, M Grätzel & M D McGehee. *Adv. Funct. Mater.*, **19** (2009) 2431–2436.

[50] H J Snaith, R Humphry-baker, P Chen, I Cesar, S M Zakeeruddin & M Grätzel. *Nanotechnology*, **19** (2008) 424003.

[51] A Listorti, B O'Regan & J R Durrant. *Chem. Mat.*, **23** (2011) 3381–3399.

[52] A J Frank, N Kopidakis & J. van de Lagemaat. *Coord. Chem. Rev.*, **248** (2004) 1165–1179.

[53] N A Anderson & T Lian. *Coord. Chem. Rev.*, **248** (2004) 1231.

[54] G H Li, C P Richter, R L Milot, L Cai, C A Schmuttenmaer, R H Crabtree, G W Brudvig & V S Batista. *Dalton Trans.*, **45** (2009) 10078–10085.

[55] G Redmond & D Fitzmaurice. *J. Phys. Chem.*, **97** (1993) 1426–1430.

[56] J Bisquert, F Fabregat-santiago, I Mora-sero, G Garcia-belmonte, E M Barea & E Palomares. *Inorg. Chim. Acta*, **361** (2008) 684–698.

[57] H Tang, F Levy, H Berger & P E Schmid. *Phys. Rev. B*, **52** (1995) 7771–7774.

[58] K Westermark, A Henningsson, H Rensmo, S Sodergren, H Siegbahn & A Hagfeldt. *Chem. Phys.*, **285** (2002) 157–165.

[59] B C O'Regan & J R Durrant. *Accounts Chem. Res.*, **42** (2009) 1799–1808.

[60] L D L Garza, Z V Saponjic, N M Dimitrijevic, M C Thurnauer & T Rajh. *J. Phys. Chem. B*, **110** (2006) 680–686.

[61] J Nelson. *Phys. Rev. B*, **59** (1999) 15374.

[62] J Nelson, S A Haque, D R Klug & J R Durrant. *Phys. Rev. B*, **6320** (2001) 205321.

[63] B C O'Regan, J R Durrant, P M Sommeling & N J Bakker. *J. Phys. Chem. C*, **111** (2007) 14001.

[64] A Listorti, C Creager, P Sommeling, J Kroon, E Palomares, A Fornelli, B Breen, P R F Barnes, J R Durrant, C Law & B O'Regan. *Energy Environ. Sci.*, **4** (2011) 3494–3501.

[65] L Schmidt-mende, S M Zakeeruddin & M Grätzel. *Appl. Phys. Lett.*, **86** (2005) 013504.

[66] F Nour-mohhamadi, S D Nguyen, G Boschloo, A Hagfeldt & T Lund. *J. Phys. Chem. B*, **109** (2005) 22413–22419.

[67] R Berera & J T M Kennis. *Photosynth. Res.*, **101** (2009) 105–118.

[68] Y Tachibana, J-E Moser, M Grätzel, D R Klug & J R Durrant. *J. Phys. Chem.*, **100** (1996) 20056–20062.

[69] Y Tamaki, A Furube, R Katoh, M Murai, K Hara, H Arakawa & M Tachiya. *C. R. Chim.*, **9** (2006) 268–274.

[70] J Kallioinen, G Benko, V Sundström, J E I Korppi-tommola & A P Yartsev. *J. Phys. Chem. B*, **106** (2002) 4396–4404.

[71] G Benko, J Kallioinen, J E I Korppi-tommola, A P Yartsev & V Sundström. *J. Am. Chem. Soc.*, **124** (2002) 489–493.

[72] G Benko, P Myllyperkio, J Pan, A P Yartsev & V Sundström. *J. Am. Chem. Soc.*, **125** (2003) 1118–1119.

[73] T Yoshihara, R Katoh, A Furube, Y Tamaki, M Murai, K Hara, S Murata, H Arakawa & M Tachiya. *J. Phys. Chem. B*, **108** (2004) 3817.

[74] J B Asbury, Y Q Wang & T Q Lian. *J. Phys. Chem. B*, **103** (1999) 6643–6647.

[75] N A Anderson, X Ai & T Q Lian. *J. Phys. Chem. B*, **107** (2003) 14414–14421.

[76] G Benko, J Kallioinen, P Myllyperkio, F Trif, J E I Korppi-tommola, A P Yartsev & V Sundström. *J. Phys. Chem. B*, **108** (2004) 2862–2867.

[77] B Wenger, M Grätzel & J-E Moser. *J. Am. Chem. Soc.*, **127** (2005) 12150.

[78] M K Nazeeruddin, A Kay, I Rodicio, R Humphrybaker, E Muller, P Liska, N Vlachopoulos & M Grätzel. *J. Am. Chem. Soc.*, **115** (1993) 6382–6390.

[79] Y Tachibana, M K Nazeeruddin, M Grätzel, D R Klug & J R Durrant. *Chem. Phys.*, **285** (2002) 127–132.

[80] S A Haque, E Palomares, B M Cho, A N M Green, N Hirata, D R Klug & J R Durrant. *J. Am. Chem. Soc.*, **127** (2005) 3456.

[81] J R Durrant, S A Haque & E Palomares. *Coord. Chem. Rev.*, **248** (2004) 1247.

[82] C Bauer, G Boschloo, E Mukhtar & A Hagfeldt. *Int. J. Photoenergy*, **4** (2002) 17–20.

[83] A Furube, R Katoh, K Hara, S Murata, H Arakawa & M Tachiya. *J. Phys. Chem. B*, **107** (2003) 4162–4166.

[84] C Bauer, G Boschloo, E Mukhtar & A Hagfeldt. *Chem. Phys. Lett.*, **387** (2004) 176–181.

[85] X Ai, N A Anderson, J C Guo & T Q Lian. *J. Phys. Chem. B*, **109** (2005) 7088–7094.

[86] R Katoh, A Furube, M Murai, Y Tamaki, K Hara & M Tachiya. *C. R. Chim.*, **9** (2006) 639–644.

[87] S E Koops & J R Durrant. *Inorg. Chim. Acta*, **361** (2008) 663–670.

[88] P Tiwana, P Docampo, M B Johnston, H J Snaith & L M Herz. *ACS Nano*, **5** (2011) 5158.

[89] M M Lee, J Teuscher, T Miyasaka, T N Murakami & H J Snaith. *Science*, **338** (2012) 643–647.

[90] S J Mousavi, M R Abolhassani, S M Hosseini & S A Sebt. *Chinese J. Phys.*, **47** (2009) 862–873.

[91] J P Chang, Y S Lin & K Chu. *J Vacuum Sci and Tech*, **19** (2001) 1782–1787.

[92] S A Haque, Y Tachibana, R L Willis, J-E Moser, M Grätzel, D R Klug & J R Durrant. *J. Phys. Chem. B*, **104** (2000) 538.

[93] N G Park, S H Chang, K J Kim & A J Frank. *Bull. Korean Chem. Soc.*, **21** (2000) 985–988.

[94] D Kuang, C Klein, H J Snaith, J E Moser, R Humphry-baker, P Comte, S M Zakeeruddin & M Grätzel. *Nano Lett.*, **6** (2006) 769–773.

[95] Y Tachibana, S A Haque, I P Mercer, J-E Moser, D R Klug & J R Durrant. *J. Phys. Chem. B*, **105** (2001) 7424–7431.

[96] S E Koops, B C O'Regan, P R F Barnes & J R Durrant. *J. Am. Chem. Soc.*, **131** (2009) 4808–4818.

[97] H J Snaith, L Schmidt-Mende, M Grätzel & M Chiesa. *Phys. Rev. B*, **74** (2006) 045306.

[98] S A Haque, Y Tachibana, R L Willis, J-E Moser, M Grätzel, D R Klug & J R Durrant. *J. Phys. Chem. B*, **104** (2000) 538–547.

[99] N Kopidakis, K D Benkstein, J. van de Lagemaat & A J Frank. *J. Phys. Chem. B*, **107** (2003) 11307–11315.

[100] H Němec, J Rochford, O Taratula, E Galoppini, P Kužel, T Polìvka, A Yartsev & V Sundström. *Phys. Rev. Lett.*, **104** (2010) 197401.

[101] P Myllyperkio, G Benko, J Korppi-tommola, A P Yartsev & V Sundström. *Phys. Chem. Chem. Phys.*, **10** (2008) 996–1002.

[102] A Islam, K Hara, L P Singh, R Katoh, M Yanagida, S Murata, Y Takahashi, H Sugihara & H Arakawa. *Chem. Lett.*, **29** (2000) 490–491.

[103] J R Durrant, Y Tachibana, I Mercer, J-E Moser, M Grätzel & D R Klug. *Z. Phys. Chemie-Int. J. Res. Phys. Chem. Chem. Phys.*, **212** (1999) 93–98.

[104] G M Turner, M C Beard & C A Schmuttenmaer. *J. Phys. Chem. B*, **106** (2002) 11716.

[105] E Hendry, M Koeberg, B O'Regan & M Bonn. *Nano Lett.*, **6** (2006) 755.

[106] A Furube, Z S Wang, K Sunahara, K Hara, R Katoh & M Tachiya. *J. Am. Chem. Soc.*, **132** (2010) 6614.

[107] J J H Pijpers, R Ulbricht, S Derossi, J N H Reek & M Bonn. *J. Phys. Chem. C*, **115** (2011) 2578–2584.

[108] A Abrusci, R S S Kumar, M Al-hashimi, M Heeney, A Petrozza & H J Snaith. *Adv. Funct. Mater.*, **21** (2011) 2571–2579.

[109] M T Dang, L Hirsch & G Wantz. *Adv. Mater.*, **23** (2011) 3597–3602.

[110] A F Nogueira, I Montanari, R Monkhouse, J Nelson & J R Durrant. *J. Phys. Chem. B*, **105** (2001) 7517–7524.

[111] C Bauer, G Boschloo, E Mukhtar & A Hagfeldt. *J. Phys. Chem. B*, **106** (2002) 12693–12704.

[112] H J Snaith. *Adv. Funct. Mater.*, **20** (2010) 13–19.

[113] J N Clifford, E Palomares, M K Nazeeruddin, M Grätzel & J R Durrant. *J. Phys. Chem. C*, **111** (2007) 6561–6567.

[114] S N Mori, W Kubo, T Kanzaki, N Masaki, Y Wada & S Yanagida. *J. Phys. Chem. C*, **111** (2007) 3522–3527.

[115] S Pelet, J-E Moser & M Grätzel. *J. Phys. Chem. B*, **104** (2000) 1791–1795.

[116] J E Kroeze, N Hirata, S Koops, M K Nazeeruddin, L Schmidt-mende, M Grätzel & J R Durrant. *J. Am. Chem. Soc.*, **128** (2006) 16376–16383.

[117] U Bach, Y Tachibana, J-E Moser, S A Haque, J R Durrant, M Grätzel & D R Klug. *J. Am. Chem. Soc.*, **121** (1999) 7445–7446.

[118] H J Snaith, A Petrozza, S Ito, H Miura & M Grätzel. *Adv. Funct. Mater.*, **19** (2009) 1810–1818.

[119] F Fabregat-santiago, J Bisquert, L Cevey, P Chen, M K Wang, S M Zakeeruddin & M Grätzel. *J. Am. Chem. Soc.*, **131** (2009) 558–562.

[120] S Sodergren, A Hagfeldt, J Olsson & S E Lindquist. *J. Phys. Chem.*, **98** (1994) 5552–5556.

[121] A Solbrand, H Lindstrom, H Rensmo, A Hagfeldt, S E Lindquist & S Sodergren. *J. Phys. Chem. B*, **101** (1997) 2514.

[122] G Boschloo & A Hagfeldt. *J. Phys. Chem. B*, **109** (2005) 12093–12098.

[123] K D Benkstein, N Kopidakis & A J Frank. *J. Phys. Chem. B*, **107** (2003) 7759–7767.

[124] A Ghicov, S P Albu, R Hahn, D Kim, T Stergiopoulos, J Kunze, C A Schiller, P Falaras & P Schmuki. *Chem.-Asian J.*, **4** (2009) 520–525.

[125] A B F Martinson, M S Goes, F Fabregat-santiago, J Bisquert, M J Pellin & J T Hupp. *J. Phys. Chem. A*, **113** (2009) 4015–4021.

[126] J Wang & Z Q Lin. *Chem. Mat.*, **22** (2010) 579–584.

[127] J B Baxter & C A Schmuttenmaer. *J. Phys. Chem. B*, **110** (2006) 25229–25239.

[128] J R Jennings, A Ghicov, L M Peter, P Schmuki & A B Walker. *J. Am. Chem. Soc.*, **130** (2008) 13364–13372.

[129] C Richter & C A Schmuttenmaer. *Nat. Nanotechnol.*, **5** (2010) 769–772.

[130] P Wang, S M Zakeeruddin, J-E Moser, M K Nazeeruddin, T Sekiguchi & M Grätzel. *Nat. Mater.*, **2** (2003) 402–407.

[131] V K Thorsmølle, B Wenger, J Teuscher, C Bauer & J-E Moser. *Chimia*, **61** (2007) 631–634.

[132] B C O'Regan, K Walley, M Juozapavicius, A Anderson, F Matar, T Ghaddar, S M Zakeeruddin, C Klein & J R Durrant. *J. Am. Chem. Soc.*, **131** (2009) 3541–3548.

[133] N Papageorgiou, W F Maier & M Grätzel. *J. Electrochem. Soc.*, **144** (1997) 876–884.

[134] M C Beard, G M Turner & C A Schmuttenmaer. *J. Phys. Chem. B*, **106** (2002) 7146.

[135] C A Schmuttenmaer. *Chem. Rev.*, **104** (2004) 1759–1779.

[136] P U Jepsen, D G Cooke & M Koch. *Laser Photon. Rev.*, **5** (2011) 124–166.

[137] J B Baxter & G W Guglietta. *Anal. Chem.*, **83** (2011) 4342–4368.

[138] E Hendry, M Koeberg, J M Schins, H-K Nienhuys, V Sundström, L D A Siebbeles & M Bonn. *Phys. Rev. B*, **71** (2005) 125201.

[139] E Hendry, F Wang, J Shan, T F Heinz & M Bonn. *Phys. Rev. B*, **69** (2004) 081101.

[140] P Parkinson, J Lloyd-Hughes, Q Gao, H H Tan, C Jagadish, M B Johnston & L M Herz. *Nano Lett.*, **7** (2007) 2162–2165.

[141] R Ulbricht, E Hendry, J Shan, T F Heinz & M Bonn. *Rev. Mod. Phys.*, **83** (2011) 543–586.

[142] M Tonouchi. *Nat. Photon.*, **1** (2007) 97–105.

[143] Yun-Shik Lee. "Principles of Terahertz Science and Technology". Springer, first edition (2009).

[144] Mark Fox. "Optical Properties of Solids". Oxford Master Series in Condensed Matter Physics. Oxford University Press, first edition (2001).

[145] J E Kroeze, T J Savenije & J M Warman. *J. Am. Chem. Soc.*, **126** (2004) 7608–7618.

[146] C J Barbe, F Arendse, P Comte, M Jirousek, F Lenzmann, V Shklover & M Grätzel. *J. Am. Ceram. Soc.*, **80** (1997) 3157–3171.

[147] S Ito, P Chen, P Comte, M K Nazeeruddin, P Liska, P Pechy & M Grätzel. *Prog. Photovoltaics*, **15** (2007) 603–612.

[148] H J Snaith & C Ducati. *Nano Lett.*, **10** (2010) 1259–1265.

[149] H J Snaith, S M Zakeeruddin, L Schmidt-mende, C Klein & M Grätzel. *Angew. Chem.-Int. Edit.*, **44** (2005) 6413.

[150] P Wang, S M Zakeeruddin, R Humphry-baker, J-E Moser & M Grätzel. *Adv. Mater.*, **15** (2003) 2101.

[151] T Horiuchi, H Miura, K Sumioka & S Uchida. *J. Am. Chem. Soc.*, **126** (2004) 12218–12219.

[152] J Salbeck, N Yu, J Bauer, F Weissortel & H Bestgen. *Synth. Met.*, **91** (1997) 209–215.

[153] J Kruger, R Plass, L Cevey, M Piccirelli, M Grätzel & U Bach. *Appl. Phys. Lett.*, **79** (2001) 2085–2087.

[154] P M Sommeling, B C O'Regan, R R Haswell, H J P Smit, N J Bakker, J J T Smits & J M Kroon. *J. Phys. Chem. B*, **110** (2006) 19191.

[155] S Kambe, S Nakade, Y Wada, T Kitamura & S Yanagida. *J. Mater. Chem.*, **12** (2002) 723.

[156] Jenny Nelson. "The Physics of Solar Cells". Imperial College Press, first edition (2003).

[157] H J Snaith. *Energy Environ. Sci.*, **5** (2012) 6513–6520.

[158] P M Sommeling, H C Rieffe, A Schonecker, J M Kroon, J A Wienke & A Hinsch. *Sol. Energy Mater. Sol. Cells*, **62** (2000) 399–410.

[159] B C O'Regan & F Lenzmann. *J. Phys. Chem. B*, **108** (2004) 4342–4350.

[160] P Docampo, S Guldin, M Stefik, P Tiwana, M C Orilall, S Huttner, H Sai, U Wiesner, U Steiner & H J Snaith. *Adv. Funct. Mater.*, **20** (2010) 1787–1796.

[161] J Bisquert. *Phys Chem Chem Phys*, **5** (2003) 5360–5364.

[162] Charles Kittel. "Introduction to Solid State Physics". Wiley, seventh edition (1995).

[163] A J Moule, H J Snaith, M Kaiser, H Klesper, D M Huang, M Grätzel & K Meerholz. *J. Appl. Phys.*, **106** (2009) 073111.

[164] Spectra-Physics. "Spitfire PRO manual" (2005).

[165] Light Conversion/Spectra-Physics. "TOPAS-C User manual" (2006).

[166] Kiyomi Sakai, editor. "Terahertz Optoelectronics". Topics in Applied Physics. Springer, first edition (2005).

[167] M Bass, P A Franken, J F Ward & G Weinreich. *Phys. Rev. Lett.*, **9** (1962) 446–448.

[168] M Bass, P A Franken & J F Ward. *Phys. Rev.*, **138** (1965) A534–A542.

[169] L Xu, X-C Zhang & D H Auston. *Appl. Phys. Lett.*, **61** (1992) 1784.

[170] A Rice, Y Jin, X F Ma, X-C Zhang, D Bliss, J Larkin & M Alexander. *Appl. Phys. Lett.*, **64** (1994) 1324.

[171] J Shan, A Nahata & T F Heinz. *J. Nonlinear Opt. Phys. Mater.*, **11** (2002) 31–48.

[172] A Nahata, A S Weling & T F Heinz. *Appl. Phys. Lett.*, **69** (1996) 2321.

[173] M Schall, M Walther & P U Jepsen. *Phys. Rev. B*, **64** (2001) 094301.

[174] N Kuroda, O Ueno & Y Nishina. *Phys. Rev. B*, **35** (1987) 3860–3870.

[175] A Leitenstorfer, S Hunsche, J Shah, M C Nuss & W H Knox. *Appl. Phys. Lett.*, **74** (1999) 1516–1518.

[176] A Debernardi. *Phys. Rev. B*, **57** (1998) 12847.

[177] Robert W. Boyd. "Nonlinear Optics". Academic Press, Inc., San Diego, second edition (2003).

[178] J A Valdmanis, G A Mourou & C W Gabel. *IEEE J. Quantum Electron.*, **19** (1983) 664–667.

[179] C Winnewisser, P U Jepsen, M Schall, V Schyja & H Helm. *Appl. Phys. Lett.*, **70** (1997) 3069.

[180] Q Wu, M Litz & X-C Zhang. *Appl. Phys. Lett.*, **68** (1996) 2924–2926.

[181] Q Wu & X-C Zhang. *Appl. Phys. Lett.*, **68** (1996) 1604–1606.

[182] Y Cai, I Brener, J Lopata, J Wynn, L Pfeiffer, J B Stark, Q Wu, X-C Zhang & J F Federici. *Appl. Phys. Lett.*, **73** (1998) 444.

[183] G Gallot, J Q Zhang, R W McGowan, T-I Jeon & D Grischkowsky. *Appl. Phys. Lett.*, **74** (1999) 3450–3452.

[184] H-K Nienhuys & V Sundström. *Phys. Rev. B*, **71** (2005) 235110.

[185] Enrique Castro Camus. "Polarisation resolved terahertz time domain spectroscopy". Ph.D. thesis, University of Oxford (2006).

[186] G L Dakovski, B Kubera, S Lan & J Shan. *J. Opt. Soc. Am. B-Opt. Phys.*, **23** (2006) 139–141.

[187] G Szabo & Z Bor. *Appl. Phys. B-Lasers Opt.*, **58** (1994) 237–241.

[188] D N Nikogosyan. *Appl. Phys. A-Mater. Sci. Process.*, **52** (1991) 359.

[189] Eugene Hecht. "Optics". Addison Wesley, fourth edition (2001).

[190] James Lloyd-Hughes. "Terahertz time-domain spectroscopy of carrier trapping in semiconductors". Ph.D. thesis, University of Oxford (2006).

[191] L Duvillaret, F Garet & J-L Coutaz. *IEEE J. Sel. Top. Quantum Electron.*, **2** (1996) 739–746.

[192] L Duvillaret, F Garet & J-L Coutaz. *Appl. Optics*, **38** (1999) 409–415.

[193] T D Dorney, R G Baraniuk & D M Mittleman. *J. Opt. Soc. Am. A-Opt. Image Sci. Vis.*, **18** (2001) 1562–1571.

[194] H Němec, F Kadlec, P Kužel, L Duvillaret & J-L Coutaz. *Opt. Commun.*, **260** (2006) 175–183.

[195] J M Schins, E Hendry, M Bonn & H G Muller. *J. Chem. Phys.*, **127** (2007) 094308.

[196] H Němec, F Kadlec & P Kužel. *J. Chem. Phys.*, **117** (2002) 8454–8466.

[197] P Kužel, F Kadlec & H Němec. *J. Chem. Phys.*, **127** (2007) 024506.

[198] K P H Lui & F A Hegmann. *Appl. Phys. Lett.*, **78** (2001) 3478–3480.

[199] H Němec, P Kužel, F Kadlec, D Fattakhova-rohlfing, J Szeifert, T Bein, V Kalousek & J Rathousky. *Appl. Phys. Lett.*, **96** (2010) 062103.

[200] E Hendry, J M Schins, L P Candeias, L D A Siebbeles & M Bonn. *Phys. Rev. Lett.*, **92** (2004) 196601.

[201] M van Exter, C Fattinger & D Grischkowsky. *Opt. Lett.*, **14** (1989) 1128–1130.

[202] E Hendry, M Koeberg, J Pijpers & M Bonn. *Phys. Rev. B*, **75** (2007) 233202.

[203] J. van de Lagemaat & A J Frank. *J. Phys. Chem. B*, **105** (2001) 11194–11205.

[204] Y Tachibana, I V Rubtsov, I Montanari, K Yoshihara, D R Klug & J R Durrant. *J. Photochem. Photobiol. A-Chem.*, **142** (2001) 215–220.

[205] J E Kroeze, T J Savenije & J M Warman. *J. Photochem. Photobiol. A-Chem.*, **148** (2002) 49–55.

[206] Y Tamaki, A Furube, M Murai, K Hara, R Katoh & M Tachiya. *Phys. Chem. Chem. Phys.*, **9** (2007) 1453.

[207] A Petrozza, C Groves & H J Snaith. *J. Am. Chem. Soc.*, **130** (2008) 12912–12920.

[208] N Kopidakis, E A Schiff, N G Park & A J Frank. *J. Phys. Chem. B*, **104** (2000) 3930–3936.

[209] T Dittrich. *Phys. Status Solidi A-Appl. Res.*, **182** (2000) 447.

[210] H Němec, P Kužel & V Sundström. *Phys. Rev. B*, **79** (2009) 115309.

[211] M C Beard & C A Schmuttenmaer. *J. Chem. Phys.*, **114** (2001) 2903–2909.

[212] N V Smith. *Phys. Rev. B*, **64** (2001) 155106.

[213] H Němec, P Kužel & V Sundström. *J. Photochem. Photobiol. A-Chem.*, **215** (2010) 123–139.

[214] A Marchioro, A Dualeh, A Punzi, M Grtzel & J E Moser. *J Phys Chem C*, **116** (2012) 26721–26727.

[215] D C Look, D C Reynolds, J R Sizelove, R L Jones, C W Litton, G Cantwell & W C Harsch. *Solid State Commun.*, **105** (1998) 399–401.

[216] Z M Jarzebski & J P Marton. *J. Electrochem. Soc.*, **123** (1976) 299C–310C.

[217] D Jousse, C Constantino & I Chambouleyron. *J. Appl. Phys.*, **54** (1983) 431–434.

[218] E Shanthi, V Dutta, A Banerjee & K L Chopra. *J. Appl. Phys.*, **51** (1980) 6243–6251.

[219] E Yagi, R R Hasiguti & M Aono. *Phys. Rev. B*, **54** (1996) 7945–7956.

[220] Ü Özgür, Y I Alivov, C Liu, A Teke, M A Reshchikov, S Doğan, V Avrutin, S J Cho & H Morkoç. *J. Appl. Phys.*, **98** (2005) 041301.

[221] Z M Zarzebski & J P Marton. *J. Electrochem. Soc.*, **123** (1976) C333–C346.

[222] A Furube, R Katoh, T Yoshihara, K Hara, S Murata, H Arakawa & M Tachiya. *J. Phys. Chem. B*, **108** (2004) 12583–12592.

[223] P Tiwana, P Parkinson, M B Johnston, H J Snaith & L M Herz. *J. Phys. Chem. C*, **114** (2010) 1365–1371.

[224] C Bauer, G Boschloo, E Mukhtar & A Hagfeldt. *J. Phys. Chem. B*, **105** (2001) 5585–5588.

[225] B Enright & D Fitzmaurice. *J. Phys. Chem.*, **100** (1996) 1027–1035.

[226] J Robertson. *J. Phys. C: Solid State Phys.*, **12** (1979) 4767–4776.

[227] A Petersson, M Ratner & H O Karlsson. *J. Phys. Chem. B*, **104** (2000) 8498–8502.

[228] N Tsuda, K Nasu, A Yanase & K Siratori. "Electronic Conduction in Oxides". Springer-Verlag, Berlin (1990).

[229] K Tennakone, J Bandara, P K M Bandaranayake, G R A Kumara & A Konno. *Jpn. J. Appl. Phys. Part 2 - Lett.*, **40** (2001) L732–L734.

[230] M K I Senevirathna, P K D D P Pitigala, E V A Premalal, K Tennakone, G R A Kumara & A Konno. *Sol. Energy Mater. Sol. Cells*, **91** (2007) 544–547.

[231] A N M Green, E Palomares, S A Haque, J M Kroon & J R Durrant. *J. Phys. Chem. B*, **109** (2005) 12525.

[232] K Tennakone, P V V Jayaweera & P K M Bandaranayake. *J. Photochem. Photobiol. A-Chem.*, **158** (2003) 125–130.

[233] P Docampo, P Tiwana, N Sakai, H Miura, L Herz, T Murakami & H J Snaith. *J Phys Chem C*, **116** (2012) 22840–22846.

[234] P Docampo & H J Snaith. *Nanotechnology*, **22** (2011) 225403.

[235] B A Gregg, S G Chen & S Ferrere. *J. Phys. Chem. B*, **107** (2003) 3019–3029.

[236] S Ferrere & B A Gregg. *J. Phys. Chem. B*, **105** (2001) 7602–7605.

[237] A Hagfeldt, U Bjorksten & M Grätzel. *J. Phys. Chem.*, **100** (1996) 8045–8048.

[238] B O'Regan & D T Schwartz. *Chem. Mat.*, **10** (1998) 1501–1509.

[239] Q Wang, Z Zhang, S M Zakeeruddin & M Grätzel. *J. Phys. Chem. C*, **112** (2008) 7084–7092.

[240] P M Kumar, S Badrinarayanan & M Sastry. *Thin Solid Films*, **358** (2000) 122–130.

[241] B J Morgan & G W Watson. *Surf. Sci.*, **601** (2007) 5034–5041.

[242] E J W Crossland, M Nedelcu, C Ducati, S Ludwigs, M A Hillmyer, U Steiner & H J Snaith. *Nano Lett.*, **9** (2009) 2813–2819.

[243] W . Y . Liang. *Phys. Educ. (UK)*, **5** (0) 226–228228.

[244] E Hendry, M Koeberg & M Bonn. *Phys. Rev. B*, **76** (2007) 045214.

[245] J B Birks. *Rep. Prog. Phys.*, **38** (1975) 903–974.

[246] S A Jenekhe & J A Osaheni. *Science*, **265** (1994) 765.

[247] A C Morteani, P Sreearunothai, L M Herz, R H Friend & C Silva. *Phys. Rev. Lett.*, **92** (2004) 247402.

[248] Laura Maria Herz. “Aggregation effects in conjugated polymer films studied by time-resolved photoluminescence spectroscopy”. Ph.D. thesis, Cambridge (2001).